UNIVERSITY OF TRENTO

PHYSICS DEPARTMENT

Ph.D. Thesis

Cycle XXXIII

Modeling of sequences of Silicon micro-Resonators for On-Chip Optical Routing and Switching

Supervisor:

Prof. Lorenzo Pavesi

Candidate:

Dr. Marco Masi

February 2011

To Stella, who will follow me.

To my mother, who will be happy.

To Vittorio and Marina, who are an example for me.

Contents

1 Silicon Photonics for Routing and Switching Applications

1.1 The need for optical interconnects

If the increase of the number of processing cores which should enhance the computational power of future multiprocessor platforms follows the same pace of Moore's law (single chip computing power doubling about every two years), an increasingly high-bandwidth and low-power communication infrastructure becomes an unavoidable option. Multicore chips became the new paradigm where the overall processing performance has been achieved by increasing the number of processing units instead of clock frequency. However, it is foreseeable that the conventional multicore approach, once it will become massively parallel, will lead also to an exponential increase in system concurrency. New inter-node communication infrastructures with optimized performance per unit power are needed. In high performance computers, multi-core processors will require data transfer rates in excess of 100 Terabit/s in the next decades. The development of processor technology of the last two decades has shown that while Moore's law continues to be confirmed, the traditional sources of performance improvements, e. g. the increase in clock frequency, experienced a flattening especially due to heat density and power constraints[1].

To face these bottlenecks the only viable technology is optical interconnects. Optical interconnects allow for additional flexibility through the use of Wavelength Division Multiplexing (WDM) while optical networks on chip (ONoC) envisage core to core photonic interconnects with large bandwidth, ultra-fast switching, ultra-low power consumption and support of WDM [2, 3]. ONoC systems must also be reconfigurable so that routing protocols can be changed on request.

In particular, in recent years silicon photonics has shown to be a promising interconnect

technology [4, 5, 6]. Silicon-on-insulator (SOI) photonic structures offer compatible fabrication processes with complementary metal-oxide-semiconductor (CMOS) technology. Microdisk lasers, photodetectors, ring filters, and flip-flop memory cells were demonstrated with promising performances and a potential for ONoCs and all-optical signal processing [7, 8, 9]. The advance of nano-silicon photonics [10] is complemented by the next generation optical lithography technologies [11] enabling the integration of complex photonic integrated circuits with CMOS technologies [12]. The recent increase of efforts aiming at building optical interconnects [13], photonic networks on chip [14], and the fabrication of active devices (e.g. high speed optical modulators and detectors [15] or compact light sources like micro-disk lasers [16]), have led to a general progress in nanophotonics. In this context, while the theory and implementation of single micro-ring resonators were extensively investigated (e.g. [17, 18, 19, 20], and references therein), cascaded resonators, as side coupled integrated spaced sequences of resonators (SCISSOR), and coupled resonator optical waveguide (CROW) systems ([21, 22, 23, 24, 25, 26]) were studied to a smaller extent [27, 28, 29, 30]. These structures are interesting because they promise to become wavelength optical routing systems, for so called λ-routing, and phase switching applications. In this work we will report about the design, fabrication and characterization of λ-router devices based on the coupling of SCISSOR systems and resorting to the interplay between the phase of the optical signals. In order to validate the modelling, I have designed Graphic Database System 2.0 (GDS II) layouts which were used to actually fabricate the proposed devices. These were then measured by other people in the laboratory (I'm particularly grateful to Mattia Mancinelli, a Ph.D. student who made most of the measurements presented). Here I use their data to compare it with my simulation results. This photonic devices are fabricated on SOI wafer. Its potential use could span from coarse WDM (CWDM) to pipeline forwarding techniques (optical node to node packet forwarding during predefined time frames [31]).

1.2 Examples of current micro-optical resonator realizations

One of the fundamental building blocks of optical interconnects is expected to be micro-optical resonators. The physics of microring resonators, and to some less extent micro racetrack- or stadium- resonators, has been studied by several authors (e.g. [17, 32, 33, 34]). These are at the basis of a large number of devices for WDM, sensing, filtering, switching, routing, or optical interconnects. Microrings are a popular choice for such applications because they can act as filters or modulators of small size, high quality factor, with good transparency to off-resonance light, and no or small intrinsic reflection. Worth mentioning is the experimental demonstration of compact and high-speed electro-optic modulators based on silicon microring resonators.[35, 36]
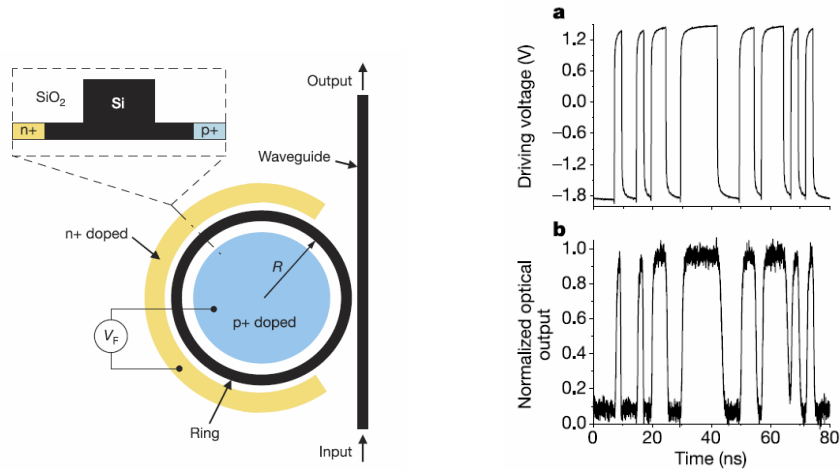
Figure 1: *Left: Schematic layout of the ring resonator-based modulator. The inset shows the cross-section of the ring. R, radius of ring. V_F, voltage applied on the modulator.* **Right:** *(a) Waveform of the electrical driving signal at 0.4 Gbit/s applied on the modulator. (b) Waveform of the output optical power of the modulator.*

These first efficient micrometer-scale silicon modulator active device operations were obtained by inducing small changes in the refractive index of the silicon by injecting electrons and holes using a p-i-n junction embedded in the ring resonator. The high speed slight effective index change leads to on-off resonant states of the structure modulating the transmitted signal. The working principle is sketched in fig. 1 left which

shows the cross-section of the rib waveguide, while fig. 1 right (a) and (b) depict the modulation of the transmitted light.

Current efforts are under way to lower the losses and bend radius of the resonators (about $1.5 \mu m$ radius ring resonators have been shown to work [37]). Cascading of active silicon micro-ring modulators for WDM optical interconnection were presented in single sided SCISSOR configuration [38]. We will present purely passive systems capable of WDM functions, i.e. devices which are fully functional without integrated electro-optical modulation.

The concepts of SCISSOR and CROW were first introduced to study their large dispersion and slow light properties [21, 22, 24]. SCISSOR exhibit two types of stop bands (band gaps): the resonator bandgaps, when the optical path of the resonators is an integer multiple of the wavelength; the Bragg bandgaps, which arise when the Bragg condition is satisfied, i.e. when the optical path of the back-reflected light is an integer multiple of the wavelength. This lends SCISSOR to various types of bandgap engineering [23, 25]. A particularly interesting SCISSOR configuration arises when the two bandgaps overlap since in this case a high order flat band pass filter is obtained whose properties depend on the number of parallel side coupled resonators. SCISSOR are also interesting for their property of conveying almost all the optical power in the Drop port, due to cascading of resonators even when the single resonator is not critically coupled to the bus waveguide. This band engineering and power optimization makes the cascading of several resonators, like in SCISSOR structures, interesting for filtering applications. The first comprehensive theoretical investigations of the optical properties of SCISSOR in their different symmetrically coupled geometrical configurations explored their slow light, dispersion and nonlinear properties [23, 39]. Later it became clear that also asymmetric coupling, called 'apodizing', offers potential advantages for filtering and switching (e.g. obtaining higher order roll off spectral side lobes and better extinctions), where also some switching and routing functions with active nxm WDM filters were considered [25, 26].

4

CROW resonant structures were studied also for their potential to engineer optical dispersion, the possibility to realize ultra-slow group velocities for various applications such as delay lines and all-optical switching [21, 40, 41]. Ultracompact optical buffers on a silicon chip were experimentally shown by IBM, where large group delay exceeding 10 bits was achieved for bit rates as high as 20 Gbps, as shown in fig. 2 [42]. Preliminary characterization of a reconfigurable CROW delay line realized on SOI with thermooptic control of the delay was also shown [43].
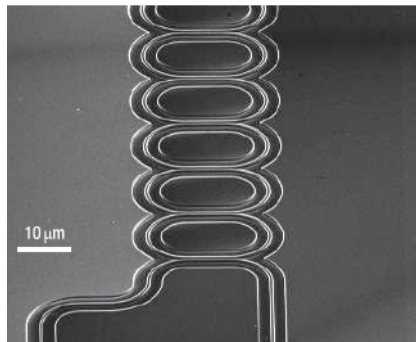
Figure 2: *Scanning electron micrographs of resonantly enhanced optical delay lines based on photonic-wire waveguides. Delay line composed of several resonators cascaded in a CROW configuration. (Source: IBM Thomas J. Watson Research Centre)*

1.3 Modern phase switching technologies and an outlook on possible enhancements

The transition from electronic to electro-optical or full optical devices can have also another potential application. In fact, the tremendous growth of communication services and information technologies demands new and enhanced networking capabilities where switching is expected to be one of the main functions in communication systems and networks. Novel optical switching technologies have the potential to play a decisive role in future telecommunication and information processing systems over traditional electronic devices, especially because of the extensive deployment of WDM technologies where the demand for high speed, scalable and rapidly reconfigurable network switching is a central issue. Several optical switching

technologies exist, like electro-optic, acousto-optic, thermo-optic, opto-mechanical and optical-amplifier based switching. Refractive index modulation inducing phase differences for switching functionalities resort especially to electro-optic or thermo-optic effects, and are widely used in directional couplers, Mach-Zhender interferometers (MZI), and multi mode interference (MMI) switches (for a good review see e.g. [44]). The present thesis will focus on some possible extensions from waveguide- to resonator-based phase switching interferometric techniques by means of micro-optical resonator systems, like SCISSOR and CROW and a particular combination of both where three waveguides serve for amplitude and phase modulation. The advantage a system of resonators has over conventional MZ coupling is its larger spectral band, its robustness against fabrication errors and signal imbalances, the possibility to operate through phase switching on several channels and its higher degrees of freedom which allow for a much larger set of behaviors compared to usual directional coupling switching, and of course its switching speed compared to electronic devices.

Some theoretical investigations of microring-resonant 2 x 2 optical switches and practical realizations of ultrafast and low power broadband electro-optic silicon switches were already done [45, 46]. Also more compact devices could be realized by fabricating spiral shaped MZ arms with p-i-n junction (like in fig. 3) which could reduce the typical 2x2 switch based MZI with two straight arms of 4mm length to a $150\mu m \times 150\mu m$ footprint.
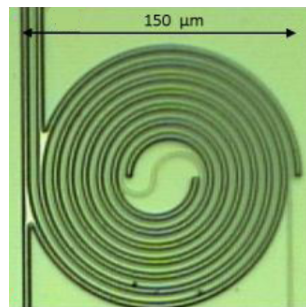

Figure 3: *A 2x2 MZI switch with spiral shaped arms (heavy gray: p-i-n- junction, light gray: waveguide).*

The theoretical analysis and practical realization of such kind of phase switching devices is however still rare. One of the main limitations is presented by current photonic

6

fabrication tolerances. Phase shifting of light requires the same interferometric precision as the device operation itself. For example the phase difference between two interfering light signals need to be tightly controlled at the sub-wavelength level to provide efficient switching. Even more sensitive to small deviations from the nominal parameters are devices where coherent addition of signals is achieved by arranging complex systems of resonator chains. These require nanometer level accuracy in the fabrication of the single resonators and their mutual spacings. For instance Coupled Resonator Induced Transparency (CRIT) effects emerge easily only for few nanometer deviations ([29, 47, 48, 49, 50, 51]).

However, while present optical lithography still suffers of few nanometers imprecision needing further improvements, the next generation optical lithography is likely to achieve in the coming years an order of magnitude leap in accuracy paving the way to novel phase modulation devices [11]. Also the fabrication of electro-optic silicon-photonic modulators which are capable of providing smooth and uniform phase shifts over a broad spectrum are a topic of intense research and promise to find a wide area of applications[52].

From our side we will demonstrate the practical realization of a novel silicon photonic phase switching device showing that resonator phase switching is indeed feasible. Therefore, it could be interesting to explore, at least from the theoretical point of view, some extensions of conventional directional coupling methods which could have potential applications in upcoming phase switching devices.

1.4   Optical networks on chip

One of the main reasons to look for ONoC technologies is energy efficiency. The problem becomes clear when one considers that for a typical electrical signalling of present technologies of 10 pJ/bit, 1000 W is required to support the interconnection bandwidth of 100 Tbit/s. Whereas optical interconnects promise to reduce energy
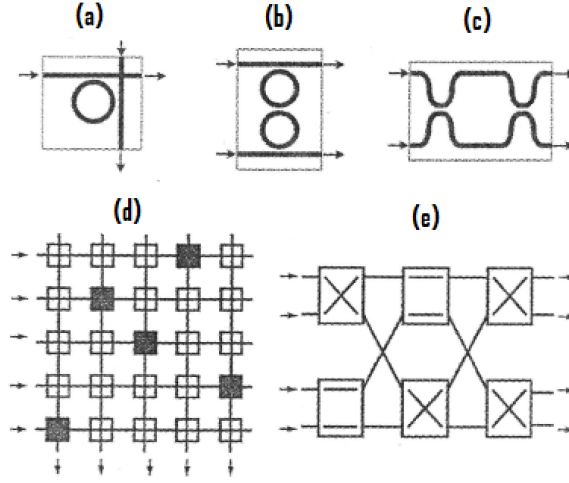
Figure 4: *The fundamental building blocks of an ONoC: the optical single, (a), and coupled, (b), micro-resonator system, (c) Waveguide-based MZI. Typical routers: (d) Cross-grid array, (e) Banyan network in cascaded 2x2 switch array configuration.*

consumption at least by an order of magnitude. The advantage over traditional technologies is also its small footprint and large bandwidth.

But the way to fully operational ONoC systems is still long. Present attempts to build efficient micro-optical routing systems are based on optical micro-resonators (fig. 4 (a), (b)), and waveguide based MZI as switching elements (fig. 4 (c)). These are used to build network structures which can be classified in two major topologies. The cross-grid optical router (fig. 4 (d) as a 5x5 nonblocking router) where at each intersection of the horizontal (input) and vertical (output) waveguide there is a 2x2 switch. In cross-state (black box) the optical signal is routed from the input to the output waveguides, whereas the switch in bar-state (white box) keeps the signal propagating straight through the bus waveguide. Fig. 4 (e) illustrates the Banyan network acting as a 4x4 nonblocking router comprising six 2x2 switches. The link path passes through only three cascaded switches. Typical optical switches structures are coupled microring resonator-based and MZI switches as shown in fig. 4 (b) and (c). Fig. 5 provides a partial list of micro-resonator array structures in different materials.

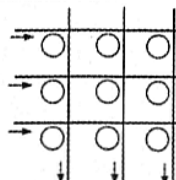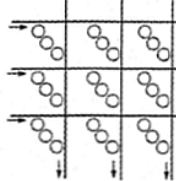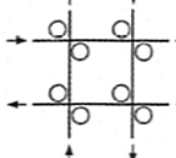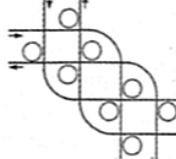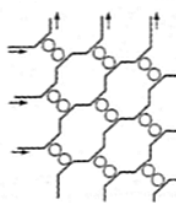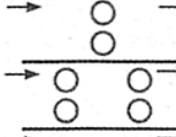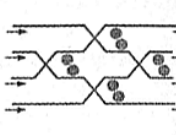|	Device configuration		Material	Comments
Cross grid	Microring resonator cross-grid array		Glass	• First experimental demonstration of 8 × 8 cross-grid array • Vertical coupling between the waveguides and the microring • Non-blocking
	Third-order coupled-microring resonators coupled cross-grid matrix switch		SiON	• First demonstration of 8 × 8 optical matrix switch • Third-order coupled-microring resonators for each cross-grid • Non-blocking
	Two microring resonators coupled cross-grid array		SOI	• 4 × 4 switch • Each crossing routes two links simultaneously • Blocking • Analysis only
	4 × 4 optical hitless router		SOI	• 4 × 4 switch • Non-blocking • Thermal-optical dynamical tuning
Banyan network	M × M second-order coupled-microring resonators-based cross-connect switch		III-V material (GaAs -AlGaAs)	• Scalable cross-connects • Non-blocking • Analysis only
	Second-order coupled-microring resonator-based switch		17mol%Ta$_2$O$_5$ doped SiO$_2$	• Wavelength-selective switch • Thermo-optic tuning • Non-blocking
	Second-order coupled-microdisk resonator-based add-drop filters array		SOI	• 4 × 4 switch • Multiple wavelength channels for optical routing • Non-blocking

Figure 5: *Microresonator array for multiple-input multiple-output optical inteconnects (Source: Poon et al. [53])*

Worth of mention are however the SOI ONoC designs. The requirements and the design of ONoC passive components were first described and validated by experimental results in [54]. Coupled two-disk add-drop filters as small as $1\mu m$ were fabricated (last SOI device from top in fig. 5). Perhaps the most relevant work was done by Bergman's
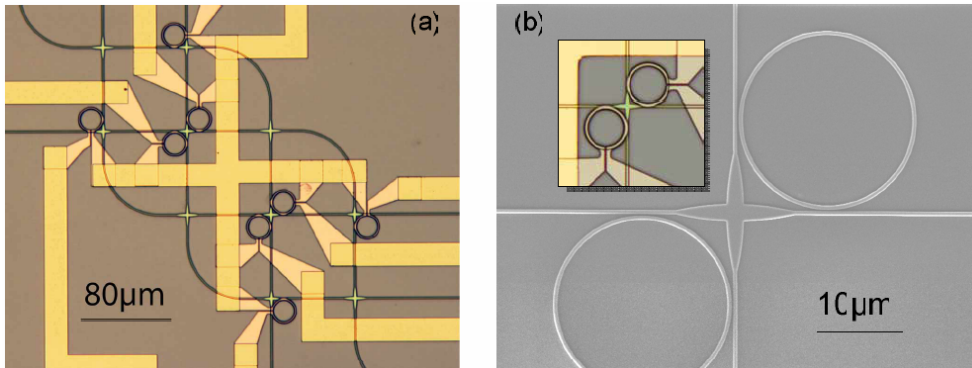
Figure 6: *Images of the 4x4 hitless router: (a) microscope image of full device shows gold contacts to nickel-chrome heaters above the microrings; (b) Scanning Electron Microscope (SEM) image shows the details of the fabricated waveguide crossing and coupled rings (insert shows close-up of Ω heaters). (Source: Sherwood et al. [55])*

group. They proposed and numerically analyzed a 4x4 blocking photonic switch [3] on SOI comprising eight silicon microring resonators laterally coupled to a waveguide cross-grid (first SOI device from top in fig. 5). Each of the photonic switching element, i.e. each two equal resonators laterally coupled to a crossing, are active: they can be in off-state (signal going through) or in on-state by the injection of electrical current into p-n contacts surrounding the rings, coupling the light into the rings. This configuration however is blocking (for example, a message routed from south to east will block message requests from west to south and from east to north). Later a non-blocking 4x4 optical hitless router was presented (second SOI device from top in fig. 5). The device was dynamically switched using thermo-optically tuned silicon microring resonators (with $10\mu m$ radius and ten waveguide crossings, see microscope images in fig. 6).[55] It has a wavelength shift to power ratio of 0.25nm/mW, is capable of routing four optical inputs to four outputs with individual bandwidths of up to 38.5 GHz, providing a maximum extinction ratio larger than 20 dB.

Future developments envisage hybrid interconnection networks overlayed to the chip multi processors in a three-dimensionally stacked monolithically integrated structure, i.e. in a multi-core processor-, a memory-, and ONoC-layer, like shown in fig. 7. This important research area attempts to extend the scaling of Moore's law into the third

10
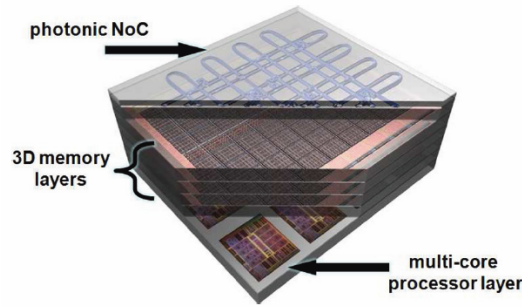
Figure 7: *Illustration of a 3D integration stack with dedicated computation, storage, and communication planes (not to scale).*

dimension by physically stacking traditionally planar chip layers, maximizing the area allotted to CMOS devices over the limited chip footprint, as well as decreasing the critical wiring distance between communicators. We will not study other geometries further, since it would go beyond the scope of this thesis (for a more in depth analysis of the geometries presented in fig. 5 see [53], for the 3D-stacking [56, 57, 58], and references therein).

1.5   Thesis plan and collaboration

The purpose of this thesis is to focus on the aspect of passive devices allowing for WDM, routing, switching and filtering of optical signals, investigating novel routing concepts based on side coupled resonators to achieve large bandwidth by multiple cascading and/or multiple coupling (low group velocity) periodicity effects. We will describe some technical aspects necessary for the design and fabrication of some passive circuitry, and usually neglected in purely theoretical approaches, including optical routers based on racetrack resonators and novel SCISSOR and CROW devices.

Most of the modelings in literature rely on approximations and simplified assumptions which depart from the real physical properties of the resonator. Within certain limits this idealization is justified since it leads to the qualitative understanding of the device behavior. But with increasing integration densities, resonators have smaller bend

radiuses and small coupling gaps. This implies that one cannot neglect in the modelling effects such as coupling losses, effective index differences and modal mismatches between the straight and bend waveguides. For a radius of curvature smaller than $R < 5\mu m$ in a SOI system, the traditional algorithms furnish very rough estimates of the optical response of microresonators, especially for some high-order filtering applications. Moreover, the situation gets worse for devices based on sequences of microresonator like in SCISSOR or CROW devices. We will describe accurately small microresonator or multiple cascaded microresonators in order to enhance design methods of complex optical systems which can tackle, at least partially, fabrication tolerances, narrowing the gap between models and real devices.

In the first part we will shortly recall the basics of coupled mode theory (CMT). A full description of the single racetrack needs an improved understanding of the behavior of its constituent parts. After an introduction to racetrack resonator theory we will briefly justify the use of racetracks instead of the more traditional ring resonators and outline its main physical properties which are necessary to understand when the fabrication of complex structures is necessary, where they appear in chains of mutually interacting fundamental components in a larger system. After a brief theoretical introduction on the behavior of add-drop filters, we will discuss the dispersion law of the straight waveguide, the characterization of curved waveguides and the influence of the bending on the effective index. Experimental results will be shown on losses and its characterization on some devices and the determination through CMT of the odd and even modes arising from the mutual interaction of waveguides. Also the determination of bending losses, the calculation of the coupling coefficients and length, and a comparison between the obtained parameters with experimental results will follow. We will use these data for a model of the single racetrack resonator. A final comparison among the proposed model, an idealized one, and experimental measurements will close the first part. We will then introduce a detailed transfer matrix formalism in order to model SCISSOR and CROW structures. Later on, novel SCISSOR based geometries are

12

presented which have the capability of routing spectral bands, i.e. CWDM in contrast to DWDM channel routing, and of a switching behavior based on phase modulation. This latter aspect will be explored in more detail at a theoretical level and will be applied also in some devices fabricated on SOI wafers applying it to few SCISSOR configurations to explore and measure their use in routing devices.

As far as it was possible in the given time frame, first attempts were made to build some device prototypes and test them experimentally. For this reason also some emphasis has been laid on the design, fabrication and experimental validation of different SCISSOR structures. However, the aim of this thesis is mainly theoretical. It wants to investigate the conceptual and analytical aspects and the physics of the structures proposed in order to lay a theoretical foundation also for those who will design and fabricate other real devices in the future.

This work was carried out in the framework of the project Wavelength Division Multiplexed Photonic Layer on CMOS (WADIMOS) which is a EU funded research project aiming at demonstrating a photonic interconnect layer on CMOS. WADIMOS objective is to build a complex photonic interconnect layer incorporating multi-channel microsources, microdetectors and different advanced wavelength routing functions. Another aim is to directly integrate with electronic driver circuits and demonstrate the application of such electro-photonic integrated circuits (ICs) in two representative applications, an on-chip optical network and a terabit optical datalink. Besides the University of Trento (UNITN), the project includes partners from industry (STM, MAPPER) as well as major research institutes and universities (IMEC, CEA-LETI, INL). ST Microelectronics is one of the world leading suppliers of electronic ICs while IMEC and CEA-LETI are the largest European research institutes on microelectronics. Mapper Lithography, a Delft University spin-off, is developing a massively parallel ebeam writing system for future electronic circuit fabrication. MAPPER was responsible for the system studies related to the terabit optical link. On its part, UNITN focused on the design of innovative optical WDM circuits based on coupled micro-optical resonators in SCISSOR configuration. The projects ends in June 2011.

2 Overview of Coupled Mode Theory

CMT has grown to a vast subject in the last three decades and is the most fundamental theoretical approach to the design and construction of practical micro-photonic devices. The most common starting point for it is the mutual lightwave interaction between (co-propagating or contra-propagating) light signals in two adjacent waveguides. In this section the coupled mode equations based on perturbation theory is first investigated, and the calculation through cross-section integrals leading to the coupling coefficients and coupling lengths is presented. As will be seen later, this approach can also be applied to a system of three waveguides which will enable us to extend Mach-Zhender interferometry techniques to more complex designs of sequences of micro-optical resonators. The optical response of a system of cascaded ring or racetrack resonators is determined by its geometry and its coupling regions, and can be modeled through a Bloch-matrix formalism (e.g. [23]) or, as will be explained in more detail in section 4, with a transfer matrix approach (see also [59, 40, 60, 61, 45, 24], and other references therein). The former deals with infinite periodic structures and is therefore only an approximation for realistic devices, while the second can be used to model finite systems. In both cases, co- and contra-propagating signals should be taken into account. We will consider only the case of co-propagating signals. The parameters calculated by means of CMT will then be employed in the following section to systemize the (somewhat scattered throughout the literature) transfer matrix approach with its generalization to racetracks.

2.1 Coupled mode equations derived from perturbation theory

There has been a great effort to describe the electromagnetic (EM) fields in coupled waveguides (for instance see the seminal work of Marcuse [62], or more recent texts [63, 64, 65, 66]). Most of its results rest on the fundamental fact that there is an orthogonal relation between the modes supported by a waveguide structure, which implies that each mode propagates independently along the waveguide without power

14

exchange among the modes itself. The modes become mutually "coupled" when energy transfer between them takes place if the original waveguide structure is altered. CMT is the theory that describes the interaction between modes and the new modes arising from the modified structure. The most important result for our purposes are the cross-sectional integrals which lead to the coupling coefficients. We will present only a sketch of the lengthy calculation following the perturbative approach adopted by K. Okamoto [63].

As well known, Maxwell's equations for source-free, time dependent fields are

$$\nabla \times \mathbf{E} = -\frac{\partial \mathbf{B}}{\partial t}\,, \tag{2.1}$$

$$\nabla \times \mathbf{H} = \frac{\partial \mathbf{D}}{\partial t}\,, \tag{2.2}$$

where t is time, $\nabla = (\partial/\partial x, \partial/\partial y, \partial/\partial z)$ is the del operator, $\mathbf{E}(t)$, $\mathbf{H}(t)$, $\mathbf{D}(t)$, $\mathbf{B}(t)$ are the time dependent vectors of the dielectric and magnetic field, the electric displacement and the magnetic induction respectively. Since we consider only waveguide structures that do not depend on the z coordinate, Maxwell's equations admit solutions whose z dependence can be expressed by the simple function $e^{i\beta z}$, with β the propagation constant, with forward and backwards fields of periodic time dependence and which can be written as

$$\mathbf{E} = \mathbf{E}_0\, e^{i\omega t} + \mathbf{E}_0^*\, e^{-i\omega t}\,, \tag{2.3}$$

where $\mathbf{E}_0$ is a complex amplitude, ω the angular frequency, and the asterisk indicates a complex conjugate. These solutions are referred as '*normal modes*'. All modes of a dielectric waveguide are orthogonal to each other [64], that is, given two uncoupled modes ϕ_a and ϕ_b we have

$$\int_{-\infty}^{+\infty} \phi_a \phi_a^*\, dx = \int_{-\infty}^{+\infty} \phi_b \phi_b^*\, dx = 1\,, \tag{2.4}$$

$$\int_{-\infty}^{+\infty} \phi_a \phi_b^*\, dx = \int_{-\infty}^{+\infty} \phi_b \phi_a^*\, dx = 0\,, \tag{2.5}$$

where , for simplicity, we assumed a two-dimensional (x, z) geometry so that x is the coordinate transverse to the waveguide. This important property is the base for much of the waveguide theory.

If the medium is lossless with a scalar dielectric constant $\epsilon(\omega)$ and scalar magnetic permeability μ, it holds

$$\mathbf{D} = \epsilon\,\mathbf{E}\,, \tag{2.6}$$

$$\mathbf{B} = \mu\,\mathbf{H}\,, \tag{2.7}$$

and Maxwell's equations for the complex amplitudes become

$$\nabla \times \mathbf{E} = -i\omega\mu\mathbf{H}\,, \tag{2.8}$$

$$\nabla \times \mathbf{H} = i\omega\epsilon\mathbf{E}\,. \tag{2.9}$$

Now, consider two waveguides of refractive index n_I and n_{II} immersed in a non-magnetic medium (i.e. $\mu \approx \mu_0$, and $n^2 \approx \epsilon/\epsilon_0 = \epsilon_r$, the dielectric constant) of refractive index n_0 and brought together as in fig. 8.
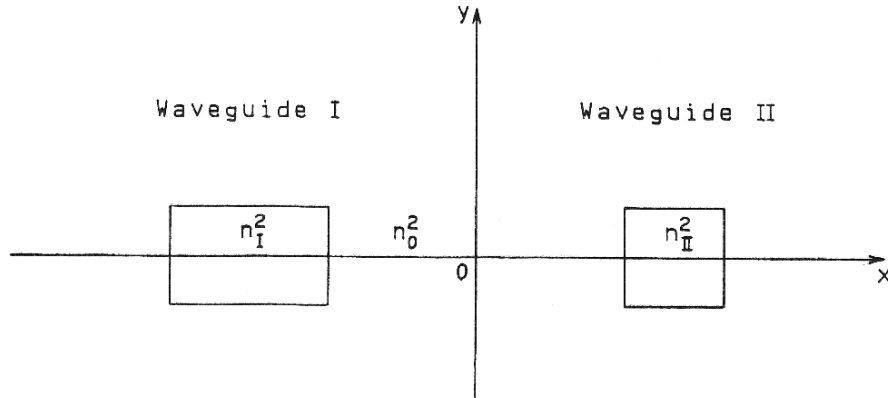
Figure 8: *Graphical z-section of directionally coupled optical waveguides.*

If the EM field distribution of the coupled waveguides does not differ too much from the uncoupled ones (further clarification will follow later on this point), then the system can be analyzed in terms of perturbation theory [63]. Let us denote the uncoupled electric and magnetic fields eigen modes as $\widetilde{\mathbf{E}}_p$, $\widetilde{\mathbf{H}}_p$ (p=1,2), satisfying complex amplitudes Maxwell's equations:

$$\nabla \times \widetilde{\mathbf{E}}_p = -i\omega\mu_0\widetilde{\mathbf{H}}_p\,, \tag{2.10}$$

$$\nabla \times \widetilde{\mathbf{H}}_p = i\omega\epsilon_0 N_p^2\widetilde{\mathbf{E}}_p\,, \tag{2.11}$$

with $N_p^2(x, y)$ the refractive index distribution of each waveguide (in capital letters, to distinguish from the uniform distribution of fig. 8). Assume the EM fields of the coupled waveguide can be expressed as the sum of the uncoupled eigen modes in each waveguide:

$$\widetilde{\mathbf{E}} = A_1(z)\widetilde{\mathbf{E}}_1 + A_2(z)\widetilde{\mathbf{E}}_2 \,, \tag{2.12}$$

$$\widetilde{\mathbf{H}} = A_1(z)\widetilde{\mathbf{H}}_1 + A_2(z)\widetilde{\mathbf{H}}_2 \,. \tag{2.13}$$

These should satisfy Maxwell's equations also, i.e.:

$$\nabla \times \widetilde{\mathbf{E}} = -i\omega\mu_0\widetilde{\mathbf{H}} \,, \tag{2.14}$$

$$\nabla \times \widetilde{\mathbf{H}} = i\omega\epsilon_0 N^2\widetilde{\mathbf{E}} \,, \tag{2.15}$$

with $N^2(x, y)$ the refractive index distribution in the entire coupled system. Using 2.14 and 2.15 and separating the transverse and axial dependency of the EM field

$$\widetilde{\mathbf{E}}_p = \mathbf{E}_p\, e^{-i\beta_p z} \,, \qquad \widetilde{\mathbf{H}}_p = \mathbf{H}_p\, e^{-i\beta_p z} \,,$$

with

$$\beta_p = \frac{2\pi}{\lambda} n_{eff_p} \,, \qquad (p = 1, 2) \tag{2.16}$$

the propagation constant given by the effective index n_{eff_p} at wavelength λ, then it can be shown ([63]) that

$$\frac{dA_1(z)}{dz} + bc_{12}\frac{dA_2(z)}{dz}\, e^{-i(\beta_2-\beta_1)z} + i\chi_1 A_1(z) + ik_{12}A_2(z)\, e^{-i(\beta_2-\beta_1)z} = 0 \,, \tag{2.17}$$

$$\frac{dA_2(z)}{dz} + bc_{21}\frac{dA_1(z)}{dz}\, e^{i(\beta_2-\beta_1)z} + i\chi_2 A_2(z) + ik_{21}A_1(z)\, e^{+i(\beta_2-\beta_1)z} = 0 \,, \tag{2.18}$$

where

$$k_{pq} = \frac{\omega\epsilon_0 \int_{-\infty}^{+\infty}\int_{-\infty}^{+\infty}(N^2 - N_q^2)\mathbf{E}_p^*\mathbf{E}_q\, dxdy}{\int_{-\infty}^{+\infty}\int_{-\infty}^{+\infty}\mathbf{u}_z(\mathbf{E}_p^* \times \mathbf{H}_p + \mathbf{E}_p \times \mathbf{H}_p^*)\, dxdy} \,, \tag{2.19}$$

$$bc_{pq} = \frac{\int_{-\infty}^{+\infty}\int_{-\infty}^{+\infty}\mathbf{u}_z(\mathbf{E}_p^* \times \mathbf{H}_q + \mathbf{E}_q \times \mathbf{H}_p^*)\, dxdy}{\int_{-\infty}^{+\infty}\int_{-\infty}^{+\infty}\mathbf{u}_z(\mathbf{E}_p^* \times \mathbf{H}_p + \mathbf{E}_p \times \mathbf{H}_p^*)\, dxdy} \,, \tag{2.20}$$

$$\chi_p = \frac{\omega\epsilon_0 \int_{-\infty}^{+\infty}\int_{-\infty}^{+\infty}(N^2 - N_p^2)\mathbf{E}_p^*\mathbf{E}_p\, dxdy}{\int_{-\infty}^{+\infty}\int_{-\infty}^{+\infty}\mathbf{u}_z(\mathbf{E}_p^* \times \mathbf{H}_p + \mathbf{E}_p \times \mathbf{H}_p^*)\, dxdy} \,, \tag{2.21}$$

17

with p and q either $(p, q) = (1, 2)$ or $(p, q) = (2, 1)$. Eqs. 2.17 and 2.18 represent the coupling modal equations that determine the spatial variation along z of the modal amplitude coefficients $A_1(z)$ and $A_2(z)$, and eqs. 2.19, 2.20 and 2.21 are the waveguide sectional integrals for multi-mode waveguides with arbitrary dimensions, refractive index and separated by an arbitrary small distance. These integrals furnish the mode coupling coefficient k_{pq} of the directional coupler, the 'butt coupling' coefficients bc_{pq} between the two waveguides, and quantity χ_p which is η times smaller than k_{pq} since the electric field $\mathbf{E}_2$ inside waveguide II is $|\mathbf{E}_2| = \eta|\mathbf{E}_1|$.

To analyze strictly the mode coupling effects all the coefficients must be calculated, but in most of the conventional analysis for directional couplers χ_p and bc_{pq} can be neglected when two waveguides are sufficiently separated, (typically, for $0.5\mu m$ wide waveguides, separations larger than 100-120 nm [67, 34]), and this approximation will be used throughout the present thesis. In lossless directional couplers k_{pq} is real (later it will have to be multiplied by a complex quantity which takes into account phase shifts). Therefore, the reciprocity relation expresses as $k_{12} = k_{21} = k$, and if we assume the waveguides differing only in their propagation constant, then equations 2.17 and 2.18 simplify to

$$\frac{dA_1(z)}{dz} = -ik\, A_2(z)\, e^{-i(\beta_2 - \beta_1)z} \,, \tag{2.22}$$

$$\frac{dA_2(z)}{dz} = -ik\, A_1(z)\, e^{+i(\beta_2 - \beta_1)z} \,, \tag{2.23}$$

which are coupled differential equations of the co-directional coupler $(\beta_1 > 0, \beta_2 > 0)$, and the solutions can be assumed in the form:

$$A_1(z) = \left[a_1 e^{iqz} + a_2 e^{-iqz}\right] e^{-i\delta z} \,, \tag{2.24}$$

$$A_2(z) = \left[b_1 e^{iqz} + b_2 e^{-iqz}\right] e^{i\delta z} \,, \tag{2.25}$$

where

$$\delta = \frac{(\beta_2 - \beta_1)}{2} \,, \tag{2.26}$$

18

is the difference of the propagation constants between the two waveguides, called *'mismatching'* and expressed in m^{-1}. It expresses the degree of synchronism between the modes, and q is a parameter to be determined. Imposing the initial conditions:

$$a_1 + a_2 = A_1(0), \qquad b_1 + b_2 = A_2(0), \tag{2.27}$$

and substituting eqs. 2.24 and 2.25 in 2.22 and 2.23 respectively, we obtain

$$A_1(z) = \left\{ \left[\cos(qz) + i\frac{\delta}{q}\sin(qz) \right] A_1(0) - i\frac{k}{q}\sin(qz)A_2(0) \right\} e^{-i\delta z}, \tag{2.28}$$

$$A_2(z) = \left\{ -i\frac{k}{q}\sin(qz)A_1(0) + \left[\cos(qz) - i\frac{\delta}{q}\sin(qz) \right] A_2(0) \right\} e^{i\delta z}, \tag{2.29}$$

with

$$q = \sqrt{k^2 + \delta^2}. \tag{2.30}$$

Considering the special case of coupling light into only one waveguide at $z = 0$ ($A_1(0) = A_0$ and $A_2(0) = 0$), the normalized optical power flowing along the z-direction in the two waveguides is given by:

$$P_a(z) = \frac{|A_1(z)|^2}{|A_0|^2} = 1 - F\,\sin^2(qz), \tag{2.31}$$

$$P_b(z) = \frac{|A_2(z)|^2}{|A_0|^2} = F\,\sin^2(qz), \tag{2.32}$$

with

$$F = \left(\frac{k}{q}\right)^2 = \frac{1}{1+X}, \tag{2.33}$$

denoting the maximum power-coupling efficiency, and

$$X = \left(\frac{\delta}{k}\right)^2, \tag{2.34}$$

the coupled-waveguide parameter. The maximum power coupled between the two waveguides is reached at $z = \frac{\pi}{2q}(2m+1)$, $(m = 0, 1, 2...)$ and the length z at $m = 0$

$$L_c = \frac{\pi}{2q} = \frac{\pi}{2\sqrt{k^2 + \delta^2}}. \tag{2.35}$$

is called *coupling length*.

When the propagation constants of the two waveguides are equal ($\beta_1 = \beta_1$ and $\delta = 0$)), the situation is said to be in perfect *'phase-matching condition'*, and 100% of power transfer occurs at the coupling length:

$$L_c = \frac{\pi}{2k} \ . \tag{2.36}$$

2.2 Even and odd modes in two coupled waveguides

It should be kept in mind that the approach to CMT followed here was perturbative and therefore it is an approximation which basically rests on two assumption. Consider that for the exponentially decaying coupling constant k it must hold $|k| = \alpha_d \, e^{-\beta_t d}$, with α_d some constant and β_t the transverse component of the propagation constant and d the distance. In CMT first it is implicitly assumed that k is small or that $\beta_t d > 1$, i.e. it decays quickly. Secondly, the initial assumption that the EM field distribution of the coupled waveguides does not differ too much from the uncoupled ones, means that the waveguides should not be too dissimilar, i.e. that $\Delta\beta$ not too large. This approximation fails in particular in those cases where waveguide transitions should be taken into account (for instance when tapers, splitters, or branching systems have to be designed). But for most applications this is a sufficient first order approximation which can be safely applied.

Therefore CMT works in a weak coupling regime where it makes first order predictions. For strong couplings other higher order theories or direct calculations of Maxwell's equations are necessary. This happens when the coupling waveguides separation becomes very small (say about 200nm for SOI waveguides) and/or the coupling section is close to the coupling length. CMT can nevertheless be used to provide an approximate representation of the light propagation in two strongly coupled photonic waveguides if one considers the splitting into the first symmetric and second anti-symmetric order modes respectively, and describing the two interacting waveguides as a five layer system like that shown in fig. 9.
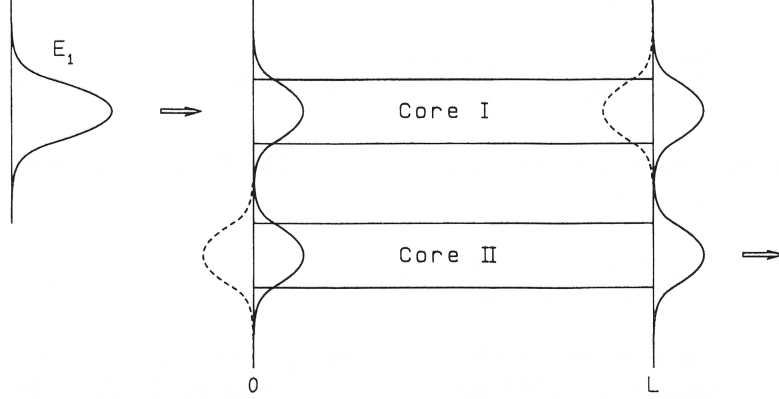
Figure 9: *Wave E_1 propagating in the five-layer slab waveguide: even (solid line) and odd (dotted line) modes.*

The even and odd normal modes can be expressed as a linear combination of the uncoupled modes (as in 2.12 and 2.13, but here for the whole structure)

$$\Psi_e = d\,\phi_a + e\,\phi_b\,, \qquad \Psi_o = -e\,\phi_a + d\,\phi_b\,. \tag{2.37}$$

Normalization imposes $d^2 + e^2 = 1$, and since the normal modes must be orthogonal it must be $\int \Phi_e \Phi_o^* \, dx$, and this requires that orthogonality conditions 2.4 and 2.5 must be satisfied. The constants e and f are related to the coupled-waveguide parameter 2.34 by

$$f = \frac{e}{d} = -X + \sqrt{(X^2 + 1)}\,, \tag{2.38}$$

which, when combined with the normalization condition above gives

$$d = \left[\frac{1}{2}\left(1 + \frac{X}{\sqrt{X^2 + 1}}\right)\right]^{1/2}, \qquad e = \left[\frac{1}{2}\left(1 - \frac{X}{\sqrt{X^2 + 1}}\right)\right]^{1/2}. \tag{2.39}$$

The normal propagation constants are given by

$$\beta_e = \overline{\beta} + \gamma\,, \qquad \beta_o = \overline{\beta} - \gamma \tag{2.40}$$

with $\gamma = |k|\sqrt{X^2 + 1}$, and $\overline{\beta} = (\beta_a + \beta_b)/2$ the average propagation constant. The important conclusion of all this analytics is that the propagation constants change as the result of the waveguide coupling.

The first immediate simplification is that of the perfect phase-matching condition (from eqs. 2.26, 2.34, and 2.39 it follows: $\Delta\beta = 0 \rightarrow \delta = 0 \rightarrow X = 0 \rightarrow e = d$). Then the normal modes are a linear combination of uncoupled modes with equal amplitude and power for all waveguide separations (for $\beta \neq 0$ the power eventually accumulates in one or the other waveguide when the distance between them increases).

An analysis to obtain the coupling coefficient k can be done considering the interference phenomena between the even and odd modes in a directional coupler in perfect phase-matching condition. Approximating the electric field by the sum of the even and odd modes as:

$$E(x, z) = E_e(x)e^{-i\beta_e z} + E_o(x)e^{-i\beta_o z}, \tag{2.41}$$

with (E_e, E_o) the even and odd mode electric fields respectively, the electric field amplitude at $z = 0$ is:

$$E(x, z) = |E_e(x) + E_o(x)| = E_1(x), \tag{2.42}$$

with E_1 the eigen mode of waveguide I. While that at z:

$$|E(x, z)| = |E_e(x) + E_o(x)e^{i(\beta_e - \beta_o)z}|, \tag{2.43}$$

which at $z = \frac{\pi}{(\beta_e - \beta_o)}$ becomes:

$$E(x, z) = |E_e(x) - E_o(x)| = E_2(x), \tag{2.44}$$

where $E_2(x)$ denotes the eigen mode of waveguide II.

So, the total power transfer from the first to the second waveguide occurs at the distance

$$L_c = \frac{\pi}{\beta_e - \beta_o}, \tag{2.45}$$

with L_c the coupling length. Therefore, from eq. 2.36 we can finally write the identity

$$k = \frac{\pi}{2L_c} = \frac{\beta_e - \beta_o}{2}, \tag{2.46}$$

which highlights the relationship between the coupling coefficient, the coupling length and the even and odd modes propagation constants. Despite phase-matching conditions,

the difference in the propagation constants of the even and odd modes implies different propagation speeds and after some distance their relative phase becomes 180^0 giving rise to the beat phenomenon: the resultant fields in the two waveguides reverse. More in general, when light has traveled a distance z the amount of (normalized and dimensionless) fraction of power coupled to the second waveguide can be obtained from the first rhs term of 2.29 (here, through 2.30, $q = k$), and is given by

$$P_{coupled} = |\kappa|^2 = \sin^2(kz)\,. \tag{2.47}$$

Therefore, it is customary to distinguish between the cross-coupling coefficient obtained from perturbation theory and the amplitudes cross-sectional integral over the section of the two waveguides of the co-directional coupler, and having the dimensions of an inverse length as in eq. 2.19, from that describing the amount of power coupled along a distance z as in eq. 2.47. From now on we will distinguish the former from the latter with a roman and Greek letter, i.e. k and κ, respectively.

2.3   CMT and phase switching basics

Let us quickly recall and derive some standard equations which describe in particular the coupling between a single waveguide with another waveguide as an isolated system, as shown in fig. 10.

Figure 10: *Single sided co-directional coupling*
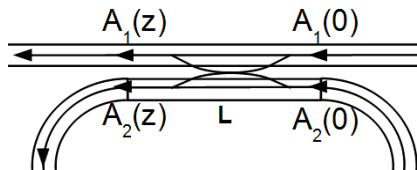
This will be necessary to understand phase switching devices, and will be used throughout the rest of this thesis. In order to clarify its application to racetrack resonators, it has been represented as a coupling between a straight waveguide and the traight section of a racetrack resonator neglecting the small curved part (this point will be justified later in section 5.2).

Sections 2.1 and 2.2 furnished the basis to understand how to solve the problem to obtain a description of the fields in two mutually interacting waveguides. We begin with the assumption that these are not too close to each others ($bc_{12} = bc_{21} = \chi_1 = \chi_2 = 0$, and mutual mode coupling coefficient $k_{12} = k_{21} = k$, see comment on pg. 18), and that they have the same geometry (width, core height, cladding, etc.), i.e. are in phase-matching condition (from eq. 2.26, $\triangle\beta = \delta = 0$). This reduces to the solution of the coupled differential equations 2.17 and 2.18.

That is:

$$\frac{\partial A_1(z)}{\partial z} = ikA_2(z),$$ (2.48)

$$\frac{\partial A_2(z)}{\partial z} = ikA_1(z),$$

where, for the sake of brevity, the change of sign on the rhs has been set by taking as convention the forward propagating initial conditions due to initial phase change with positive complex argument in the Euler exponent as

$$A_1(0) = A_1 e^{i\phi_1}, \quad A_2(0) = A_2 e^{i\phi_2}.$$ (2.49)

Then the solutions which describe the complex fields in the two waveguides at z are

$$A_1(z) = tA_1 e^{i\phi_1} + i\kappa A_2 e^{i\phi_2}$$ (2.50)

$$A_2(z) = i\kappa A_1 e^{i\phi_1} + tA_2 e^{i\phi_2},$$ (2.51)

with

$$\kappa = \sin(kz)e^{i\beta z}, \quad t = \cos(kz)e^{i\beta z},$$ (2.52)

the cross-coupling coefficient of eq. 2.47 and the through-coupling coefficient (obtained from the first term of the rhs of eq. 2.28) respectively, and $e^{i\beta z}$ accounting for the phase shift along the structure. Recalling eq. 2.36 or eq. 2.46, $k = \frac{\pi}{2L_c}$, and these can be written as

$$\kappa = \sin\left(\frac{\pi L}{2L_c}\right)e^{i\beta L}, \quad t = \cos\left(\frac{\pi L}{2L_c}\right)e^{i\beta L},$$ (2.53)

where, because of 2.45, the coupling length is

$$L_c = \frac{\lambda}{2\left(n_{effe}(\lambda) - n_{effo}(\lambda)\right)}, \tag{2.54}$$

with λ the wavelength, L the length of the coupling section (not to be confused with the coupling length), while n_{effe} and n_{effo} are the even and odd mode wavelength dependent effective indexes respectively.

From eqs. 2.50 and 2.51 it follows

$$|A_1(z)|^2 = |t|^2|A_1|^2 + |\kappa|^2|A_2|^2 + 2|\kappa||t||A_1||A_2|\sin\Delta\phi, \tag{2.55}$$

$$|A_2(z)|^2 = |\kappa|^2|A_1|^2 + |t|^2|A_2|^2 - 2|\kappa||t||A_1||A_2|\sin\Delta\phi, \tag{2.56}$$

with $\Delta\phi = \phi_1 - \phi_2$ and where, from now on, we omit the coupling coefficients dependence in z. Power conservation condition for the lossless system follows straightforwardly from 2.53, or 2.55 and 2.56, as $t^2 + \kappa^2 = 1$.

If we set $A_2 = 0$ we obtain the well known power exchange expressions for the single sided co-directional coupler made of two equal and synchronous waveguides

$$|A_1(z)|^2 = \cos^2(kz)|A_1|^2 = |t|^2|A_1|^2, \tag{2.57}$$

$$|A_2(z)|^2 = \sin^2(kz)|A_1|^2 = |\kappa|^2|A_1|^2. \tag{2.58}$$

The typical Mach-Zhender phase switching method is obtained when we couple two signals with same amplitude ($A_1 = A_2 = A$), then one could use phase modulation for switching the power into one or the other waveguide.

In fact, for this special case, 2.55 and 2.56 become

$$|A_1(z)|^2 = |A|^2\left(1 + 2|\kappa||t|\sin\Delta\phi\right), \tag{2.59}$$

$$|A_2(z)|^2 = |A|^2\left(1 - 2|\kappa||t|\sin\Delta\phi\right), \tag{2.60}$$

which tell us that, while there would be no net power exchange between the two waveguides for no de-phasing ($\Delta\phi = 0$), for a de-phasing of an integer multiple of
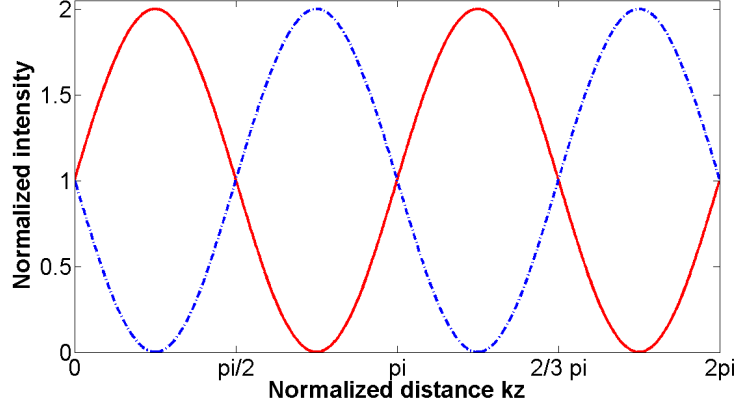
Figure 11: *Single sided co-directional coupling for two signals with same amplitude and $\Delta\phi = \frac{\pi}{2}$ phase difference (red solid line: $A_1(z)$, blue dotted-dashed line: $A_2(z)$), normalized intensity: input powers set to unity, normalized distance kz (where $k = \frac{\pi}{2L_c}$ is the cross-coupling).*

$\Delta\phi = \frac{\pi}{2}$ all the power couples forth and back among the two waveguides, as shown in fig. 11.

From now on, for 'normalized intensity' it is meant that per convention the powers of the input signals are set to unity and the ordinate axis of the graphs will be rescaled to the sum of the input intensities (e.g. here $|A_j(z)|^2/(|A_1(0)|^2 + |A_2(0)|^2)$, with (j=1,2) and $|A_1(0)|^2 = |A_2(0)|^2 = 1$). For 'normalized distance' we set kz, with $k = \frac{\pi}{2L_c}$, which makes the graphs independent from the coupling strengths.

This is a different situation than the classical case of eqs. 2.57 and 2.58 where the power transfer occurs always, independently from any phase condition. If we chose the length of the coupling section L such that $kL = \frac{\pi}{4}$ (i.e., according to 2.46, half the coupling length), then we have built a very simple phase switching device: a de-phasing of $\pm\frac{\pi}{2}$ will transfer all the power into one or the other waveguide, as shown in fig. 12.
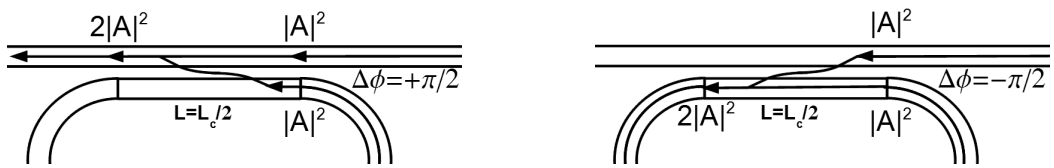
Figure 12: *Special case of fig. 10 for $kz = \frac{\pi}{4}$ and $\Delta\phi = \pm\frac{\pi}{2}$ de-phasing. Light is coupled into one or another waveguide.*

2.4 CMT and phase switching for the double sided symmetric co-directional coupler

However, eqs. 2.48 don't describe the situation we have in fig. 13, where three waveguides have to be considered. We can not naively add twice the field of eq. 2.50 or 2.51 into the middle waveguide, the Drop port, and take the modulus square to obtain the intensity.
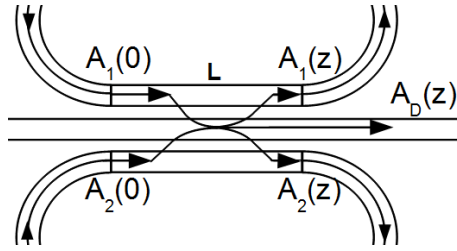
Figure 13: *Double sided (ds-) symmetric co-directional coupling*

To write the set of differential equations that are more adequate for the couplings of the system of fig. 13 consider the case of a Drop signal A_D excited by the fields in the upper and lower waveguides with amplitudes A_1 and A_2. Then, if we assume that the direct coupling between the two outer waveguides can be neglected, the set of three coupled differential equations which describe the system of fig. 13 is given by

$$\frac{\partial A_1(z)}{\partial z} = ik A_D(z) , \tag{2.61}$$

$$\frac{\partial A_D(z)}{\partial z} = ik A_1(z) + ik A_2(z) ,$$

$$\frac{\partial A_2(z)}{\partial z} = ik A_D(z) .$$

We impose the initial conditions

$$A_1(0) = A_1 e^{i\phi_1} , \tag{2.62}$$

$$A_D(0) = A_D e^{i\phi_D} , \tag{2.63}$$

$$A_2(0) = A_2 e^{i\phi_2} , \tag{2.64}$$

where ϕ_1, ϕ_1 and ϕ_D express the phase of A_1, A_2 and A_D respectively.

27

The solutions of the system 2.61 then are

$$A_1(z) = t' A_1 e^{i\phi_1} + i\kappa_D A_D e^{i\phi_D} - \kappa' A_2 e^{i\phi_2} , \tag{2.65}$$

$$A_D(z) = i\kappa_D A_1 e^{i\phi_1} + t_D A_D e^{i\phi_D} + i\kappa_D A_2 e^{i\phi_2} , \tag{2.66}$$

$$A_2(z) = -\kappa' A_1 e^{i\phi_1} + i\kappa_D A_D e^{i\phi_D} + t' A_2 e^{i\phi_2} , \tag{2.67}$$

with

$$t' = \cos^2\left(\frac{kz}{\sqrt{2}}\right) e^{i\beta z}, \quad t_D = \cos(\sqrt{2}kz)\, e^{i\beta z} , \tag{2.68}$$

$$\kappa' = \sin^2\left(\frac{kz}{\sqrt{2}}\right) e^{i\beta z}, \quad \kappa_D = \frac{1}{\sqrt{2}}\sin(\sqrt{2}kz)\, e^{i\beta z} . \tag{2.69}$$

To keep things simple lets consider the special case where $A_D = 0$. Then the intensities are given by:

$$|A_1(z)|^2 = |t'|^2|A_1|^2 + |\kappa'|^2|A_2|^2 - 2|\kappa'||t'||A_1||A_2|\cos\Delta\phi , \tag{2.70}$$

$$|A_D(z)|^2 = |\kappa_D|^2\left(|A_1|^2 + |A_2|^2 + 2|A_1||A_2|\cos\Delta\phi\right) , \tag{2.71}$$

$$|A_2(z)|^2 = |\kappa'|^2|A_1|^2 + |t'|^2|A_2|^2 - 2|\kappa'||t'||A_1||A_2|\cos\Delta\phi . \tag{2.72}$$

The sum of 2.70, 2.71, and 2.72 results in the total input power $|A_1(z)|^2 + |A_2(z)|^2$, always. If the system is lossless power conservation implies $|k'|^2 + |k_D|^2 + |t'|^2 = 1$. The term $\frac{1}{\sqrt{2}}$ in front of the second eq. of 2.69 indicates equal (per unit power) contribution from the two external waveguides to the middle one and is a consequence of the symmetry of the system (symmetric coupling and geometry). We can consider the separate contribution amplitudes to the Drop port as:

$$A_{D1}(z) = \kappa_D|A_1(z)|e^{i\phi_1} , \tag{2.73}$$

$$A_{D2}(z) = \kappa_D|A_2(z)|e^{i\phi_2} , \tag{2.74}$$

such that

$$|A_D(z)|^2 = |\,|A_{D1}(z)|e^{i\phi_1} + |A_{D2}(z)|e^{i\phi_2}\,|^2 . \tag{2.75}$$

Despite not being directly coupled to each others, from 2.70 and 2.72, we see that the field in the first (second) waveguide depends also from the initial signal in the second (first) one. This expresses the effects of crosstalk between the outer waveguides through the intermediate Drop port (crossing of arrows through the Drop port shown in fig.13). This can be seen by injecting a signal only in one of the ports, say in A_1 and not in A_2, which reduces 2.70, 2.71, and 2.72, by using eqs. 2.68 and 2.69, to

$$|A_1(z)|^2 = |A_1|^2 \cos^4(\frac{kz}{\sqrt{2}}),\tag{2.76}$$

$$|A_D(z)|^2 = \frac{|A_1|^2}{2} \sin^2(\sqrt{2}kz),\tag{2.77}$$

$$|A_2(z)|^2 = |A_1|^2 \sin^4(\frac{kz}{\sqrt{2}}).\tag{2.78}$$

Figure 14: *Power transfer in the waveguides of the ds-coupler for one input signal only (eqs. 2.70, 2.71 and 2.72, with initial conditions $A_1 = 1$, $A_2 = 0$). Red dashed line: amplitude $A_1(kz)$; blue dotted-dashed line: amplitude $A_2(kz)$; black solid line: amplitude $A_D(kz)$.*

Eqs. 2.76, 2.77 and 2.78 are traced in fig. 14 in normalized intensity. These show that the signal from the upper (lower) waveguide is never completely recovered in the Drop port because part of it re-couples towards the lower (upper) waveguide. The Drop behaves like a 'power transiting' port and the amount of light that crosses the structure can be considered as a measure of crosstalk. However, we will see that this interpretation must be taken with caution. In fact, things change in this respect if we consider the case where we have the same input signals in amplitude and phase ($A_1 = A_2 = A$).
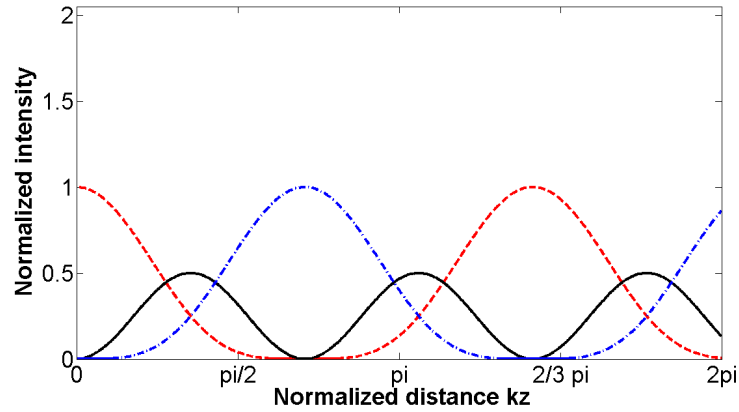
29
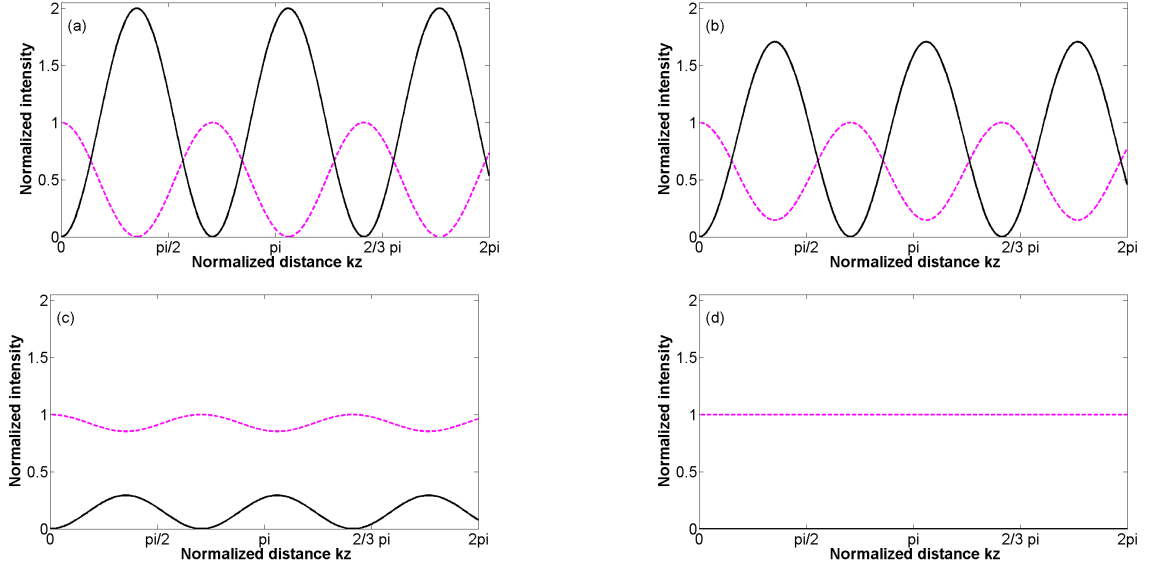
Figure 15: *Power transfer in the waveguides of the ds-coupler for two equal input signals (eqs. 2.70, 2.71 and 2.72, with initial conditions $A_1 = 1$, $A_2 = 1$, $\Delta\phi = (0, \frac{\pi}{4}, \frac{3}{4}\pi, \pi)$ in (a), (b), (c), (d) respectively). Magenta dotted-dashed line: amplitude $A_1(kz)$ and $A_2(kz)$; black solid line: amplitude $A_D(kz)$.*

Eqs.2.70, 2.71 and 2.72 then simplify to:

$$|A_1(z)|^2 = |A_2(z)|^2 = |A|^2 \left(1 - \frac{1}{2}\sin^2(\sqrt{2}kz)(1 + \cos\Delta\phi) \right),$$

$$|A_D(z)|^2 = |A|^2(1 + \cos\Delta\phi)\sin^2(\sqrt{2}kz). \tag{2.79}$$

The case for in phase signals ($\Delta\phi = 0$) is shown in normalized intensity in fig. 15(a). In this case, the energy transfer between the Drop and external ports occurs harmonically and there can be 100% power transfer. When two in phase signals with equal amplitude are injected into the double sided co-directional coupler system (ds-coupler) of fig. 13, and if one chooses the length L of the coupling section such that

$$L = \frac{\pi}{2\sqrt{2}\,k} = \frac{L_c}{\sqrt{2}}, \tag{2.80}$$

with the last passage because of 2.46, then the power is completely transferred into the Drop port and none remains in the outer waveguides. This is contrary to the previous case of the single input signal where always some power was coupled towards the Drop and the opposite waveguide, independently from the length of the coupling section

30

chosen. Fig. 15(b) and 15(c) shows the case for a phase difference of $\Delta\phi = \frac{\pi}{4}$ and $\Delta\phi = \frac{3}{4}\pi$: the power in the outer waveguides 1 and 2 (magenta dotted-dashed line) oscillates around the initial input value but is never turned off, while the Drop (black solid line) turns on or off according the propagation length like in the previous case, but reaches less intensity. If instead a phase difference of $\Delta\phi = \pi$ is applied (fig. 15(d)) the power in the Drop port will be switched off always (and *not* necessarily maintaining the same coupling section length 2.80) and $|A_1|^2 = |A_2|^2 = |A|^2$, i.e. the light in the two coupling waveguides doesn't couple at all and no power goes into the Drop port.

Therefore, a particularly interesting situation occurs when we build a ds-coupler with coupling section length 2.80 ($kz = \frac{1}{\sqrt{2}}\frac{\pi}{2}$ in the graphs) and have two balanced input signals. Because in this case we can use it as a phase switching device: for a $\Delta\phi = 0$ all the power goes into the drop and none into waveguides 1 and 2 (fig. 16), while for $\Delta\phi = \pi$ all the power will go through waveguides 1 and 2 and nothing will couple into the Drop port (fig. 17).
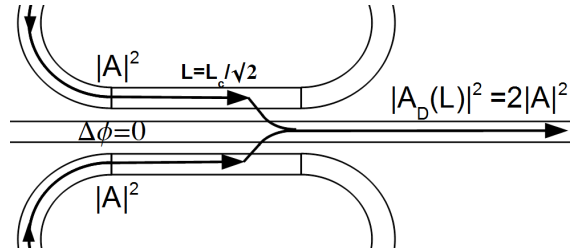

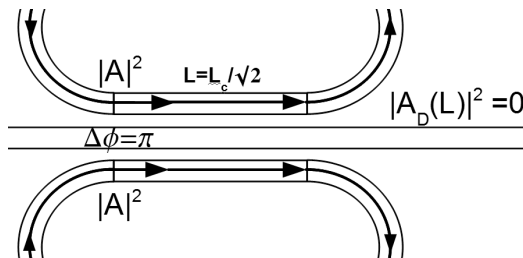**Figure 16:** *The ds-coupler switch in phase: all the power goes into the Drop port.*

Figure 17: *The ds-coupler switch out of phase: no power couples into the Drop port.*

Under these circumstance the system behaves as if the crosstalk between waveguide 1 and 2 has been suppressed since, independently from the coupling strength, it is

31

possible to direct from waveguide 1 (waveguide 2) all the light into the Drop port but without observing any part of it re-coupling to waveguide 2 (waveguide 1). At first this seems to be at odds with the previous situation of the single input case of fig. 14 where it is impossible to observe any power in the Drop port without having some fraction of it already coupled towards the opposite waveguide. This apparent contradiction is explained by the fact that the signal in waveguide 1 (waveguide 2) undergoes twice a phase change of $\frac{\pi}{2}$ (again, because of the $\frac{\pi}{2}$ phase difference of the evanescent wave) and the net π de-phased cross coupled wave interferes destructively in waveguide 2 (waveguide 1). This interference effect leads to a mutual subtraction of the cross coupled powers (graphically: the transformation of the dashed lines of fig. 14 into those of fig. 15). Therefore, such very simple device as a ds-coupler could possibly serve as zero-crosstalk and ultra-fast photonic switch.

For completeness we mention also the case where the light is injected only in the Drop waveguide, i.e. where in the initial conditions we set

$$A_1(0) = 0, \ A_D(0) = A_D, \ A_2(0) = 0 \,, \tag{2.81}$$

that, from eqs. 2.65, 2.66 and 2.67, lead to

$$A_1(z) = A_2(z) = \frac{iA_D \sin(\sqrt{2}kz)}{\sqrt{2}} \, e^{i\beta z} \,, \tag{2.82}$$

$$A_D(z) = A_D \cos(\sqrt{2}kz) \, e^{i\beta z} \,, \tag{2.83}$$

whereby of course

$$|A_1(z)|^2 = |A_2(z)|^2 = \frac{|A_D|^2}{2} \sin^2(\sqrt{2}kz) = |A_D|^2 \frac{|\kappa_D|^2}{2} \,, \tag{2.84}$$

$$|A_D(z)|^2 = |A_D|^2 \cos^2(\sqrt{2}kz) = |A_D|^2 \, |t_D|^2 \,, \tag{2.85}$$

shows that the power is equally distributed along the outer waveguides. Note that imposing coupling section 2.80 leads to complete power transfer into waveguide 1 and 2, i.e. the ds-coupler can be used as a splitter.

Its advantage over other splitting devices, as Y-branches or MMI splitters, is that it would be less sensitive to imbalances (and losses at the wavelength where condition 2.80 holds), its disadvantage is obviously that the equally distributed amount of power is wavelength dependent through 2.54.

3 Micro-Optical Racetrack Resonator Theory

3.1 Some theoretical aspects on the add-drop optical modelling

Racetracks resonators (see fig. 18) have several advantages with respect to ring resonators. For instance, it is easier to determine the coupling strength since it is
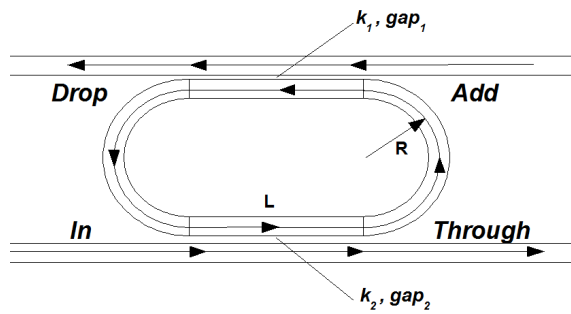
Figure 18: *The racetrack resonator structure.*

controlled by two parameters: the length L of the two straight coupling guides and their separation gap. The CMT between two straight waveguides is more straightforward than between a straight and a bent waveguide. Spacing tolerances are less critical for the coupling gaps in racetracks compared to rings, because if stronger couplings are needed only the coupling length has to be increased without decreasing the spacing between the input guide and the resonator, which is instead more difficult to calibrate precisely. In addition, the TE-polarization is frequently taken as a default for many theoretical investigations and practical applications. But ring resonators work better in TM-polarization since the coupling efficiency is higher for TM than TE-polarization due to its lower field confinement. Therefore, racetracks are more suitable to obtain the desired couplings in TE. The disadvantage of racetracks versus ring geometries is about losses, since the effective length of racetracks is longer than that of rings and due to the phase mismatch between the straight and bend component. For this reason we will also address the issue of loss optimization. However, if very high quality factors are not needed, this is usually not a real stumbling block.

Let us discuss firstly what happens when the bus waveguide starts to interact with the racetrack resonator. We will consider the waveguides in perfect phase-matching condition ($\Delta\beta = 0 \rightarrow X = 0, \ e = d$) and apply the results discussed in section 2.2. However, according to 2.40 the propagation constant of the anti-symmetric mode of the same order is lower than the symmetric one. Intuitively this can be explained by the fact that the anti-symmetric wave is pushed towards the interface between the waveguide core and the surrounding lower index cladding region. The deviation from the mean $\overline{\beta} = \frac{\beta_e + \beta_o}{2}$ is negligible for large separations, but in resonator systems where also a slight variation of the effective index can induce resonance shifts, this effect can become relevant especially for small gaps and induces spectral shifts of the racetrack resonances. These are called *coupling-induced resonance frequency shifts* (CIFS) and can have deleterious effects on high-order resonant filters [67].

Once the effective indexes of the even and odd modes are known they can be used to obtain the coupling coefficients and lengths. According to 2.47, the cross- and transmission- coupling coefficients, κ and t (those derived considering mode interference, dimensionless and such that their modulus square represents the fraction of the coupled power), are given by 2.53 and 2.54. In absence of losses, $\kappa^2 + t^2 = c^2$ with $c = 1$ and c the coupling loss parameter. But in general $c \leq 1$ since there can be coupling losses due to roughness at the bend-straight interfaces, due to the small power transfer asymmetry between the odd and even modes and also due to the mode conversion losses which however become relevant only for very small gaps (smaller than 120nm).[34]

Given the two coupling coefficients κ_1, κ_2, the upper and lower coupling losses c_1 and c_2, the bend and straight propagation constants β_b and β_s, the roughness and radiation losses α, and the racetrack's perimeter $p = 2L + 2\pi R$ (see fig. 18), then one can analytically model the spectral response of the racetrack using the well known relations which connect the In, Through, Add and Drop ports, or resort to the more general

transfer matrix analysis (see chapter 4), obtaining:

$$T = \frac{|Through|^2}{|In|^2} = c_1^2 \frac{t_1^2 + c_1^2 c_2^2 t_2^2 e^{-\alpha 4\pi R} - 2c_1 c_2 t_1 t_2\, e^{-\alpha 2\pi R}\cos(\beta_b 2\pi R + \beta_s 2L)}{1 + c_1^2 c_2^2 t_1^2 t_2^2 e^{-\alpha 4\pi R} - 2c_1 c_2 t_1 t_2\, e^{-\alpha 2\pi R}\cos(\beta_b 2\pi R + \beta_s 2L)}, \quad (3.1)$$

$$D = \frac{|Drop|^2}{|In|^2} = \frac{c_1^2 c_2^2\, \kappa_1^2 \kappa_2^2 e^{-\alpha 2\pi R}}{1 + c_1^2 c_2^2 t_1^2 t_2^2 e^{-\alpha 4\pi R} - 2c_1 c_2 t_1 t_2\, e^{-\alpha 2\pi R}\cos(\beta_b 2\pi R + \beta_s 2L)}, \quad (3.2)$$

where T and D are the optical mode intensity at the Through and Drop ports respectively.

Notice the fourth power of c in eq. 3.2, which means that especially in the Drop a small change in the coupling losses can lead to large deviations from the idealized model.

3.2 Modelling of the straight waveguide

The dispersions of the refractive indexes of silicon and silica have been obtained at room temperature (20°C) by fitting the data from [68]:

$$n_{Si}(\lambda) = 3.4277 + \frac{0.1104}{\lambda^2} + \frac{0.041}{\lambda^4}, \quad (3.3)$$

$$n_{SiO_2}(\lambda) = 1.4213 + \frac{0.0856}{\lambda^2} - \frac{0.0735}{\lambda^4}, \quad (3.4)$$

which at $\lambda = 1.55\mu m$ give $n_{Si} = 3.4758$ and $n_{SiO_2} = 1.4442$.

The stripe waveguides have been modelled with a full vectorial finite difference (FVFD) mode solver which was developed at the Institut des Nanotechnologies de Lyon (INL) [69]. For straight waveguides transparent boundaries conditions (TBC) were used. TBC implement a realistic boundary that allows the wave to leave the computational region without numerical appreciable reflections. These properties make a FVFD with TBC most appropriate for high refractive index contrast and a small core SOI rib-waveguides. For bend waveguides uniaxial perfectly matched layers (UPML) were used as absorbing boundary conditions. The mode solver developed at INL uses either cartesian or cylindrical coordinates.

Fig. 19 reports the effective indexes for waveguide widths (wgw) of 400, 450 and 500nm and for two core thicknesses of 200nm (top) and 220nm (bottom) in TE polarization. Larger widths would lead to multimode guides. For wgw= $0.5\mu m$ and 220nm core, already the second mode appears, but it is fortunately very lossy. The effective mode dispersions can be fitted by a polynomial regression of the second order.
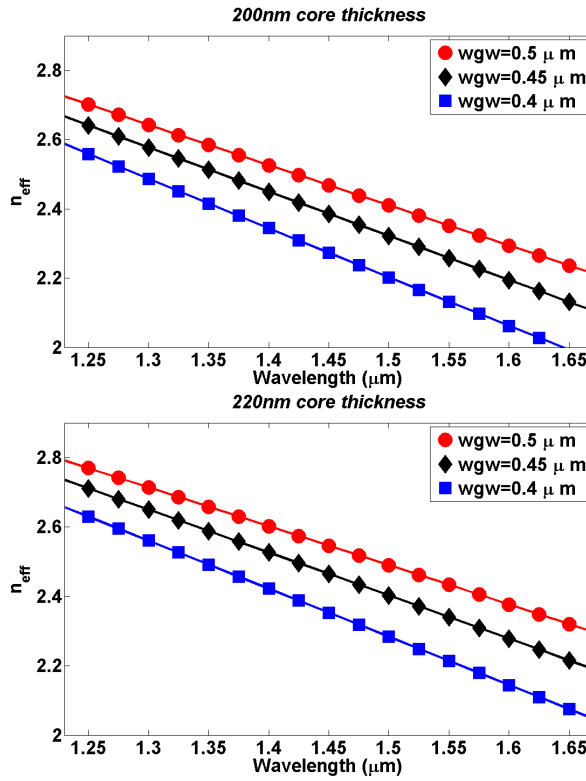
Figure 19: *Effective index variation versus wavelength in TE polarization for strip straight waveguides of different width and core dimensions.*

The polynomial coefficients, the width and the height of the core of a stripe straight waveguide for a wavelength range between 1250-1650nm are reported in Table 1.

3.3 Modelling of the bend waveguide

We used FVFD in cylindrical coordinates with UPML boundary conditions to model curved waveguides. The electric and magnetic components are governed by wave equations that are a linear system of two differential equations where the r and z

37

Table 1: $n_{effs}(\lambda) = a + b\lambda + c\lambda^2$

Core thickness (nm)	wgw (nm)	a	b $[\mu m^{-1}]$	c $[\mu m^{-2}]$
	500	4.1739	-1.1905	0.009671
200	450	4.2603	-1.3096	0.011578
	400	4.4929	-1.6478	0.080459
	500	4.1169	-1.0447	-0.026851
220	450	4.1725	-1.1171	-0.041857
	400	4.3359	-1.3494	-0.012511

components of the electric and magnetic fields are coupled [70]:

$$r^2 \frac{\partial}{\partial r}\left(\frac{1}{\varepsilon_r}\frac{\partial}{\partial r}(\varepsilon_r E_r)\right) + r\frac{\partial}{\partial r}E_r + \frac{2r}{\varepsilon_r}\frac{\partial}{\partial r}(\varepsilon_r E_r) + r^2 \frac{\partial^2}{\partial z^2}E_z + (r^2 k_0^2 \varepsilon_r + 1)E_r +$$

$$+ r^2 \frac{\partial}{\partial r}\left(\frac{1}{\varepsilon_r}\frac{\partial}{\partial z}(\varepsilon_r E_r)\right) - r^2 \frac{\partial^2}{\partial r\partial z}E_z + \frac{2r}{\varepsilon_r}\frac{\partial}{\partial z}(\varepsilon_r E_z) = \beta^2 E_r, \quad (3.5)$$

$$r^2 \varepsilon_r \frac{\partial}{\partial r}\left(\frac{1}{\varepsilon_r}\frac{\partial}{\partial r}H_z\right) + r\frac{\partial}{\partial r}H_z + r^2 \frac{\partial^2}{\partial z^2}H_z + r^2 k_0^2 \varepsilon_r H_r$$

$$- r^2 \varepsilon_r \frac{\partial}{\partial r}\left(\frac{1}{\varepsilon_r}\frac{\partial}{\partial z}H_r\right) - r^2 \frac{\partial^2}{\partial r\partial z}H_r = \beta^2 H_z, \quad (3.6)$$

where $\varepsilon_r = \varepsilon_r(r, z)$ is the permeability, $k_0 = \frac{2\pi}{\lambda}$ the vacuum wave number, $\beta = \beta_b + i\alpha$ the complex propagation constant with α the radiation loss parameter, and

$$\beta_b = r\, n_{effb}(\lambda)k_0 \quad (3.7)$$

the real part which gives the effective index for the bend, n_{effb}. Since losses due to bending are negligible in high refractive index contrast bending with respect to scattering losses due to roughnesses, we focus our attention on the real part of the propagation constant. Note that in cylindrical coordinates the propagation constant is dimensionless and proportional to r, and that it expresses also the azimutal mode number for a resonant mode of a ring resonator $m = \frac{n_{effb}(\lambda_m)\,2\pi R}{\lambda_m}$ at $r = R$ (see section 3.5).

While we will take as convention throughout this work the physical curvature of a bend the middle radius of the waveguide, an open question is the value of the optical
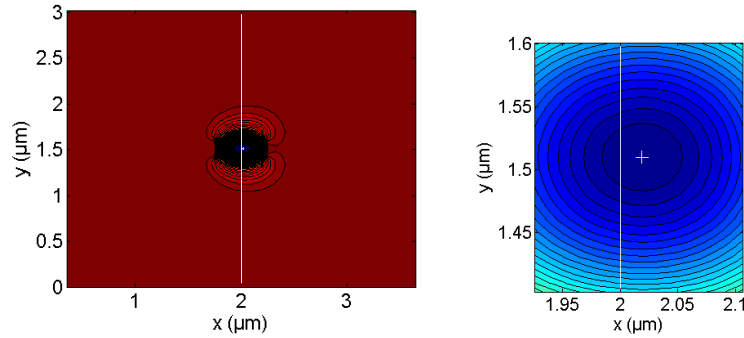
38

Figure 20: *Magnetic field and zoom onto its shifted field center (wgw=0.5 μm, R=2 μm, $\lambda = 1.55\mu m$). The white straight line indicates the geometrical center of the waveguide, the cross the position of maximal optical field intensity.*

curvature radius $r = R$ in the equation here, i.e. is it the outer, middle or inner radius of the waveguide, or the position of maximal field intensity which should be used? The specific choice leads to contradicting results because the radius determines not only different magnitudes for the propagation constant, but also a different signature in the change of the effective index between the same bend and the straight waveguide $\delta n_{eff} = n_{effb} - n_{effs}$, with n_{effs} the effective index of the straight waveguide. Does bending cause an increase or a decrease of the effective index? We choose the outer core radius as r as in [71]. The shift of the mode profile away from the center towards the edge of a bent waveguide can be seen readily by conformal transformation where the constant index profile of a curved waveguide is transformed to an exponentially decreasing profile with increasing bend curvature of a leaky straight waveguide. Another point of view of the same physical phenomenon at a more fundamental level is that to invoke Fermat's principle. Fermat's principle states that the path of a light ray between two points follows a stationary optical path (minimal in refractive media) with respect to variations of the path. The bending produces a slight offset, δR, of the light ray from the waveguide center towards the outer interface. A graphical example of this effect is shown in fig. 20.

Therefore, the light traveling on a $R + \delta R$ radius has a smaller optical path length despite the larger physical path, due to a smaller effective index for the bend than for

39
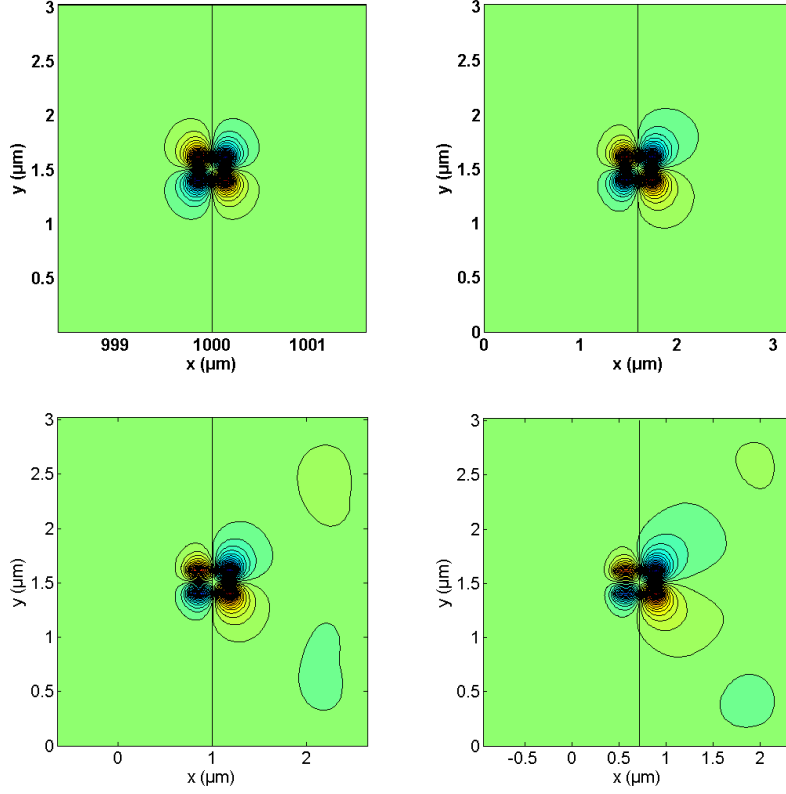
Figure 21: *Mode profiles of the first mode (E_x field, wgw= $0.5\mu m$, $\lambda = 1.55\mu m$, 220nm core) for bent waveguides of different curvature radii (from the top to the bottom: $R = 1000\mu m$, $R = 1.50\mu m$, $R = 1\mu m$, $R = 0.75\mu m$).*

the straight waveguide of similar cross-section. This implies

$$n_{effb}(R + \delta R) \leq n_{effb}(R)\frac{R}{R + \delta R} \, . \tag{3.8}$$

And eq. 3.8 equality must hold because we are considering the mode with the same azimutal number (i.e. $\beta_b(R) = \beta_b(R + \delta R)$). Once equations 3.5 and 3.6 are solved the shift of the maximum optical field intensity from the waveguide center can be found, δR. This is then used to scale the propagation constant accordingly to $R + \delta R$.

Fig. 21 shows some electric field maps for the E_x component of the fundamental mode for the almost straight ($R = 1000\mu m$) and bent waveguides with different curvature radii of $R = 1.5\mu m$, $R = 1\mu m$ and $R = 0.75\mu m$.
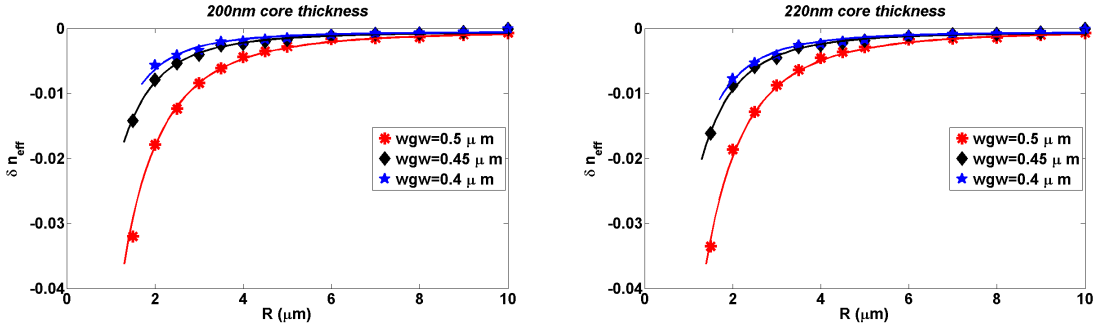
Figure 22: *Effective index variations due to bending compared to the straight waveguide.*

The so-obtained values for the variation of the effective index due to bending are shown in fig. 22 for different radii, waveguide widths and core thicknesses. For $R < 1.5 - 2\mu m$ the fit has been truncated because the mode becomes radiative. The waveguide with wgw$=0.4\mu m$ becomes radiative for a larger curvature radius than the wgw$=0.45~\mu m$ and wgw$=0.5~\mu m$ waveguides. In addition, the wgw$=0.5~\mu m$ waveguide is multimode. Therefore in the following we have chosen a wgw$=0.45~\mu m$ waveguide. For future reference Table 2 gives the parameters of a fit to δn_{eff}, with the errors on the parameters and the root mean square (RMS) on the value of δn_{eff}.

One can see that for bending radius larger than about $5\mu m$ the effect of the curvature is substantially negligible. For smaller radii $\delta n_{eff} = 2 - 3 \times 10^{-2}$, which corresponds to a resonance wavelength shift in a micro-ring of up to a dozen nm, i.e. an entire free spectral range (FSR).

Table 2: $\delta n_{eff} = \alpha - \frac{\beta}{1+(R+\gamma)^\delta} ; \quad (\lambda = 1.55\mu m)$

Core(nm)	wgw(nm)	α	β	γ	δ	$RMS(\delta n_{eff})$
	500	$-4.6 \times 10^{-4} \pm 7 \times 10^{-5}$	0.58 ± 0.27	1.20 ± 0.26	2.99 ± 0.21	7.4×10^{-5}
200	450	$-5 \times 10^{-4} \pm 6 \times 10^{-7}$	$0.106 \pm 1 \times 10^{-3}$	$0.536 \pm 7 \times 10^{-3}$	$2.726 \pm 5 \times 10^{-3}$	4.9×10^{-7}
	400	$-5 \times 10^{-4} \pm 4 \times 10^{-6}$	$0.220 \pm 28 \times 10^{-3}$	$1.017 \pm 65 \times 10^{-3}$	$3.268 \pm 57 \times 10^{-3}$	4.5×10^{-6}
	500	$-3.1 \times 10^{-4} \pm 3 \times 10^{-5}$	0.215 ± 0.043	0.48 ± 0.14	2.538 ± 0.21	2.1×10^{-5}
220	450	$-5.9 \times 10^{-4} \pm 2 \times 10^{-5}$	0.4864 ± 0.013	1.269 ± 0.13	3.363 ± 0.12	2.2×10^{-5}
	400	$-5.7 \times 10^{-4} \pm 1.4 \times 10^{-5}$	0.60 ± 0.24	1.387 ± 0.19	3.595 ± 0.17	1.7×10^{-5}

3.4 Evaluating bend losses, coupling coefficients and phase mismatching

Bends and resonators were fabricated on SOI wafers by DUV lithography, within the WADIMOS project. To measure the bending losses we used test structures which are composed by 100 90° bends (fig. 23). An offset configuration has been tested where the width of the straight waveguide varies between 0.38 to 0.5 μm and that of the curved one according to its radius as given in fig. 24, in order to evaluate the radiation and reflection effects on the losses of the bend. A selection of the bend losses measurements (TE-mode, $R = 2\mu m$) versus the wavelength is shown in fig. 25.
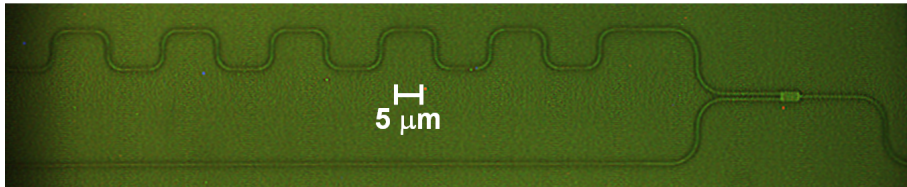
Figure 23: *Optical microscope image of the test device used for the losses measurements of the curved waveguides ($R = 2.35\mu m$).*
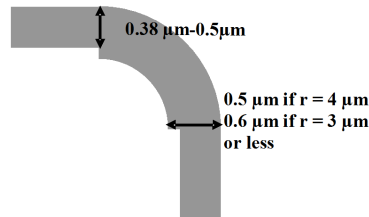
Figure 24: *Type of offsets used.*

The measurements, carried out at the INL laboratory, have an accuracy of about 0.01 dB/90°. The 500 nm wide waveguide has been used as reference with respect to the 450 nm wide waveguide where the bends have offset. The offset is aimed to make negligible the mode mismatch losses at the bends. Offset bends in the 450 nm wide waveguide yields the smaller losses despite the smaller waveguide width: about 0.024dB/90° throughout all the $1.5 - 1.6\,\mu m$ spectrum. Similar values have been found also for
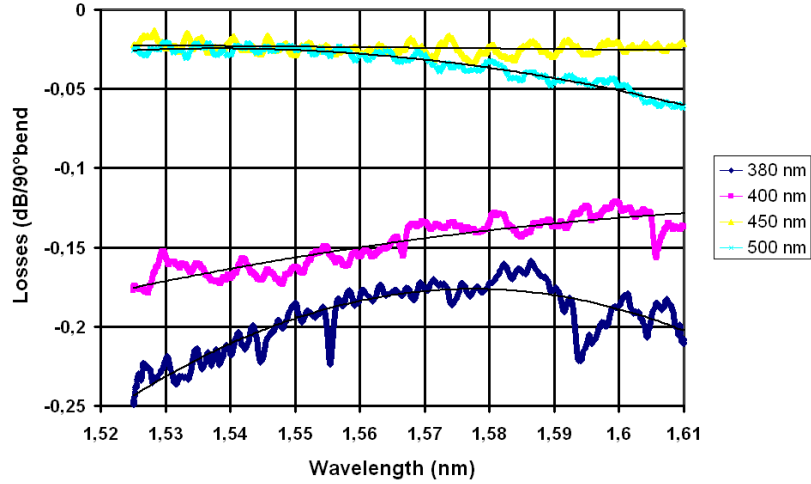
Figure 25: *Bend losses versus the wavelength for different widths of the straight waveguide (bend wgw=0.6μm, R = 2μm, TE-mode).*

0.5μm widths at $\lambda < 1.55\,\mu m$, but for larger wavelengths the loss increases up to 0.06dB/90° at 1.61μm. This shows the relevance of the modal matching at the bends via waveguide offset.

The mode solver is then used to calculate the even and odd modes of a system formed by two straight coupled waveguides (waveguide coupler) and its effective indexes. From this one obtains the difference between the effective index and the mean of the even and odd modes in a straight waveguide for various wavelengths and coupling spacings:

$$\triangle n(\lambda) = n_{eff}(\lambda) - \frac{n_{effo}(\lambda) + n_{effe}(\lambda)}{2}\,.$$

An illustration of such calculation is given in fig. 26 for TE polarization. The variation is very small but sufficient for allowing a shift of the resonant wavelength of several tenths of nm for a coupling length of 10μm. Table 3 furnishes the appropriate fitting parameters.

From the even and odd effective indexes, the coupling length and coefficients can be calculated with eq. 2.53. A comparison with experiments can be done by fitting the measured throughput signal out of a racetrack resonator. Knowing the propagation constant, the losses involved, setting the coupling loss =-0.1 dB (see the next section)

43
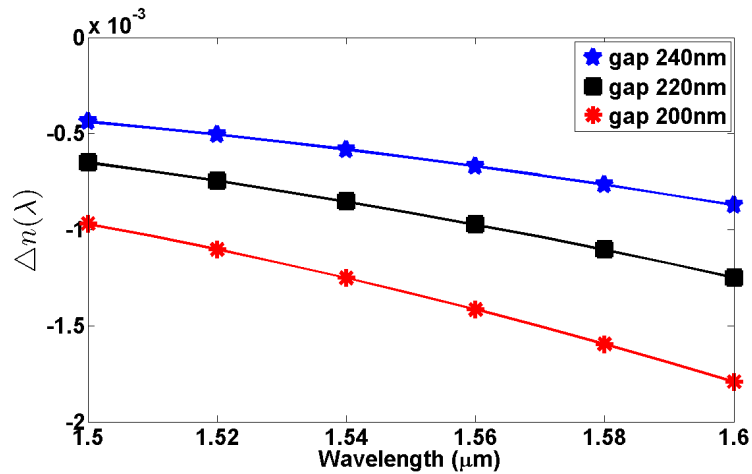
Figure 26: *Difference between the effective index and the mean of the even and odd modes in a straight waveguide for various coupling spacings (TE-polarization).*

Table 3: *Even-odd mode effective index mismatch.*

$\triangle n = a + b\lambda + c\lambda^2$	a	b $[\mu m^{-1}]$	c $[\mu m^{-2}]$
d=200nm	-0.03547	0.052282	-0.019521
d=220nm	-0.028363	0.04141	-0.01529
d=240nm	-0.022467	0.032535	-0.011899

and considering symmetric coupling ($\kappa_1 = \kappa_2 = \kappa$), from eq. 3.1 we have the coupling coefficient t and then, from eq. 2.54, the coupling length L_c is finally obtained. A comparison between the modelled and experimental measured coupling lengths of a waveguide coupler versus the wavelength for a spacing of 200 nm and 220 nm is given in fig. 27.

Despite a general agreement, we observe a tendency of the model to overestimate the coupling length. This can be due to a difference between the nominal and the actual values of the waveguide width. Indeed the model results are extremely sensitive to the waveguide width. The coupling length dependence on the wavelength can be approximated by a polynomial regression of the second order. The coefficients of the regression are summarized in Table 4.

.
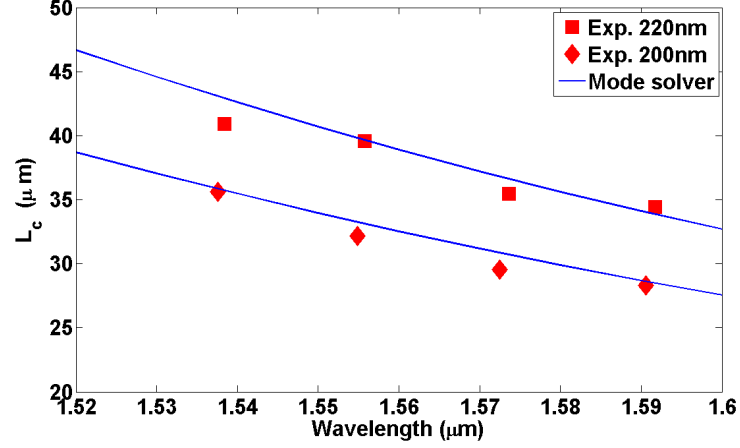
Figure 27: *The coupling length spectral variation of twin waveguide couplers (0.5μm width) for different spacing.*

Table 4: *Coupling length coefficients*

$L_c = a + b\lambda + c\lambda^2$	a	b $[\mu m^{-1}]$	c $[\mu m^{-2}]$
d=200nm	1116.8	-1308.3	374.62
d=220nm	1505.5	-1705.6	490.69

.

3.5   Spectral response modelling of the racetrack resonator

By using all the parameterizations reported in the previous sections and tables, we can model the optical path in a racetrack resonator as:

$$p_{opt}(\lambda) = 2\, n_{neffs}\, L + 2\, n_{effb}\, \pi R + (\triangle n_1 + \triangle n_2)\, L \tag{3.9}$$

where n_{neffs} and n_{neffb} are the effective indexes of the straight and bent waveguide, and $\triangle n_1$ and $\triangle n_2$ are the variation between the effective index of the straight waveguide from the mean value of the odd and even modes in the two coupling regions of the racetracks (fig. 18). There is no loss of generality if the optical path is expressed as a

weighted mean of the effective indexes as

$$p_{opt} = \overline{n}_{eff} * p$$

with

$$\overline{n}_{eff} = \frac{2\,n_{neffs}\,L + 2\,n_{effb}\,\pi R + (\triangle n_1 + \triangle n_2)\,L}{2L + 2\pi R}$$

and $p = 2L + 2\pi R$ the resonators's physical perimeter. The mean propagation constant is $\overline{\beta} = k_0\,\overline{n}_{eff}$, and the still exact phase delay induced by the racetrack as a whole $\triangle\Phi = \overline{\beta}\,p$.

In the following we will work with these averaged quantities and represent them with the parametrization of the previous sections. With the results of Table 1, the group index becomes

$$\overline{n}_g(\lambda) = \overline{n}_{eff}(\lambda) - \lambda\,\frac{\partial \overline{n}_{eff}(\lambda)}{\partial \lambda} = a - c\lambda^2\,, \tag{3.10}$$

which does not depend from parameter b, while the group velocity dispersion (GVD) parameter D is

$$D(\lambda) = -\frac{\lambda}{\mathbf{c}}\,\frac{\partial^2 \overline{n}_{eff}(\lambda)}{\partial \lambda^2} = -\frac{2\lambda c}{\mathbf{c}}\,, \tag{3.11}$$

with $\mathbf{c}$ the speed of light.

Given the propagation constant at resonance

$$\overline{\beta}_m = \overline{n}_{eff}(\lambda_m)\,k_0 = \frac{2m\pi}{p}\,,$$

we can write

$$\overline{\beta}_{m-1} = \frac{2(m-1)\pi}{p} = \overline{\beta}_m - \frac{2\pi}{p} \approx \beta_m + \left|\frac{\partial \overline{\beta}}{\partial \lambda}\right|_m \Delta\lambda\,,$$

where the right hand side is obtained as a first order Taylor series expansion of β at the m-th resonance wavelength and $\Delta\lambda$ is the difference between the wavelengths of two resonances, i.e. the FSR. Since

$$\left|\frac{\partial \overline{\beta}}{\partial \lambda}\right|_m = -\frac{k_0}{\lambda_m}\left(\overline{n}_{eff}(\lambda_m) - \lambda_m\,\frac{\partial \overline{n}_{eff}(\lambda_m)}{\partial \lambda}\right) = -\frac{k_0}{\lambda_m}\,\overline{n}_g(\lambda_m)\,, \tag{3.12}$$

where 3.10 has been applied, then the FSR is

$$FSR(\lambda_m) = \frac{\lambda_m^2}{\overline{n}_g(\lambda_m)\,p} \;. \tag{3.13}$$

and

$$\lambda_m = \frac{p_{opt}(\lambda_m)}{m} \;. \tag{3.14}$$

Therefore, 3.13 is an implicit function in λ_m through 3.9.

Table 1 and Eq. 3.11 show that the dispersion changes sign for the 200 nm versus 220 nm wide strip waveguide. Fine engineering of the core thickness might be a mean to obtain a nearly zero GVD waveguide, but this is usually not an easy task from the practical point of view and SOI waveguides with small cores and high refractive index contrast may suffer of highly dispersive effects. Errors on the FSR depend both on the effective index and the dispersion law as

$$\triangle FSR = -\frac{\lambda^2}{p}\frac{\triangle n_g}{n_g^2} = -FSR\frac{\triangle n_g}{n_g} = -FSR\frac{\left(\triangle n_{eff} - \lambda\triangle\left(\frac{dn_{eff}}{d\lambda}\right)\right)}{n_g} \;. \tag{3.15}$$

In other words, in order to obtain reasonable evaluations of the FSR and resonant mode frequencies, one must match both the effective index and the effective index dispersion, especially when dispersive effects become consistent.

In order to assess the mode solver's accuracy we obtained the necessary parameters experimentally measuring the response of a set of racetrack resonators. In particular, to establish from the measurement data the dispersion law of Table 1 we proceeded as follows. First we took two resonant modes λ_m and λ_n and measured the FSR between $[\lambda_m - \lambda_{m+1}]$ and $[\lambda_n - \lambda_{n+1}]$. Trough eq. 3.10 and eq. 3.13 a system of two equations and two unknowns follows

$$a - c\lambda_m^2 = \frac{\lambda_m^2}{FSR(\lambda_m)\,p} \qquad a - c\lambda_n^2 = \frac{\lambda_n^2}{FSR(\lambda_n)\,p} \tag{3.16}$$

which yields the experimental values of parameters a and c to be compared with those of Table 1. Then, in order to obtain the third parameter, one measures a resonant mode

at some other wavelength λ_l, inserts a and c into the optical path of equation 3.14 through eq. 3.9 and solves for b

$$b = \frac{m - \delta n_{eff} \, 2\pi R/\lambda_l - (\triangle n_1 + \triangle n_2) \, L/\lambda_l}{p} - c\lambda_l - \frac{a}{\lambda_l} . \qquad (3.17)$$

Here δn_{eff}, $\triangle n_1$ and $\triangle n_2$ are still obtained by the parameters of Table 2 and 4, but the relative error on these can be considered negligible compared to that on the effective index of the straight waveguide. The last free parameter left is the resonant mode number m, which can be only an integer number and is found by matching the effective index dispersions obtained by the experimental a, b, c values and by the a, b and c values reported in Table 1. It is assumed that it is the integer which best matches the theoretical curve of Table 1 through 3.17. An assumption that can be verified by comparing the spectral response associated to the so obtained dispersion law. And from this the accuracy of the mode solver effective index functions versus the experimental curve can be assessed.

Fig. 28 left shows an example of a measured through and drop port signals of a racetrack resonator with $L = 10\mu m$, wgw= $0.5\mu m$, $R = 2\mu m$, gap= $0.2\mu m$, and core=$220nm$. Fig. 28 right shows the analytical spectrum calculated from the experimentally obtained dispersion law (we obtain: $a = 3.7123$, $b = -0.8604\,\mu m^{-1}$, $c = -0.0155\,\mu m^{-2}$). We note that the experimental effective index function applied to the analytical model reproduces the racetrack spectrum.

It must be noted that, while the precise knowledge of dispersion law determines the FSR and the mode resonance frequencies, it still does not determine the extinction rates of the Through and Drop ports, which depend also on the coupling loss. The latter is a quite difficult parameter to be directly measured. In principle it could be inferred from eqs. 3.1 and 3.2 by measuring the slight shift it produces in the maximal transmission of the Drop signal. In practice this implies a precise normalization of the drop signal intensity which is usually affected by unbalance in the Y-splitter or MMI-component used (fig. 23). Interestingly however, once the dispersion law is obtained with the above
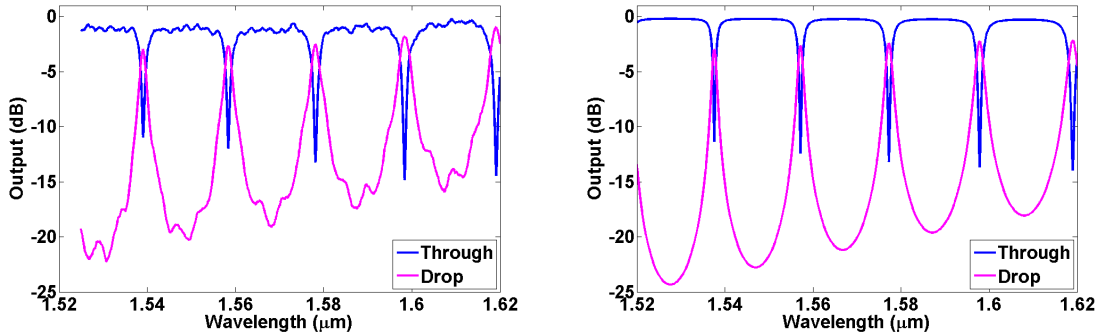
Figure 28: *The racetrack's measured spectrum (left) and its spectrum obtained from the experimentally deduced dispersion law (right).*
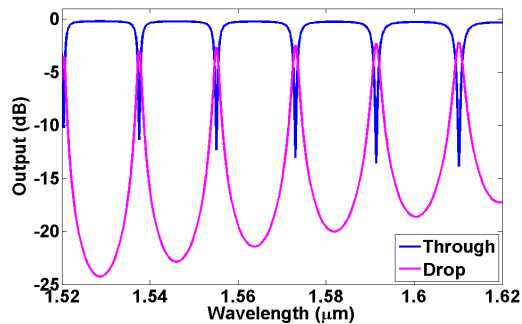
Figure 29: *The racetrack's spectrum obtained from the mode solver parameters.*

procedure, the fine tuning of the coupling loss parameter in the analytical model to reproduce also the experimentally measured extinctions, can nevertheless furnish a first estimate. For the specific case here reported we obtain a coupling loss of -0.1 dB.

Fig. 29 shows the spectrum obtained from the parameters furnished by the mode solver ($a = 4.1169$, $b = -1.0447\,\mu m^{-1}$, $c = -0.026851\,\mu m^{-2}$). The difference is not negligible, a certain discrepancy is visible, especially in the FSR which results 3nm smaller than the observed one. On one side this shows how the exact determination of the mode resonances and its FSR is very sensitive to the evaluation of the precise dispersion law. The dispersion law should be determined with a precision better than 1% which is out of reach of the presently available mode solver softwares.

On the other side, fig. 30 shows that the difference between the experimentally deduced effective index law and that predicted by computational means alone are quite similar and differ in the $1.5 - 1.6\,\mu m$ in the worst case only by 2%. We consider this a fairly
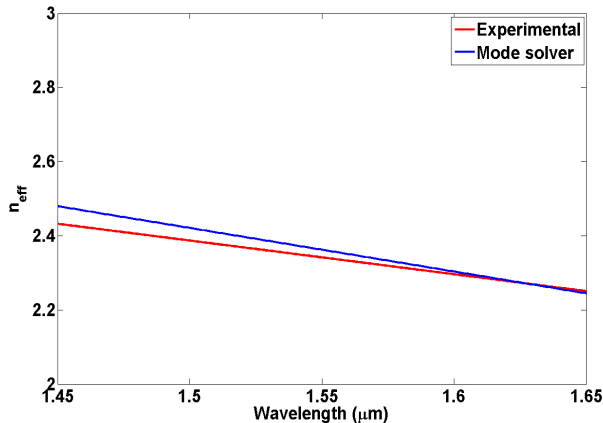
Figure 30: *Effective index difference between the experimental and mode solver model.*

good accuracy. We compared our FVFD mode solver with others (see [72]) and obtained the same results when averaging the refractive index at the boundaries of the waveguide in order to overcome the strong discontinuity of the first derivative of the permittivity at the boundaries. The only difference with the other methods is that it is possible to perform the modelling without averaging of the refractive index (the finite difference scheme is applied to the first derivative of the permittivity times the field, as described in eq. 3.5 and 3.6), while the dispersion law of the materials is included in the calculation. It is much more complicate with the 3D finite difference time domain (FDTD) algorithms (besides requiring much more computing power). Also with finite element method mode solvers it is not possible to perform the modelling without averaging. The difference must also be searched in the fabrication tolerances. Especially geometrical properties like small deviations from the nominal waveguide widths, unperfect sidewall surface verticality of the waveguides can induce unpredictable effective index variations which make the precise FSR and resonant mode wavelength control still a difficult task.

Finally, we would like to illustrate how it is possible to obtain experimentally the coupling factors and the total loss of the racetrack only by measuring the contrasts of the Through and Drop signals. From eq. 3.1 and 3.2 the maximum and minimum of the

Through and Drop functions are

$$T_{max} = c_1^2 \frac{\left(t_1 + c_1 c_2 t_2\, e^{-\alpha 2\pi R}\right)^2}{\left(1 + c_1 c_2 t_1 t_2\, e^{-\alpha 2\pi R}\right)^2} \; ;$$

$$T_{min} = c_1^2 \frac{\left(t_1 - c_1 c_2 t_2\, e^{-\alpha 2\pi R}\right)^2}{\left(1 - c_1 c_2 t_1 t_2\, e^{-\alpha 2\pi R}\right)^2} \; , \tag{3.18}$$

$$D_{max} = \frac{c_1^2 c_2^2\, \kappa_1^2 \kappa_2^2 e^{-\alpha 2\pi R}}{\left(1 - c_1 c_2 t_1 t_2\, e^{-\alpha 2\pi R}\right)^2} \; ;$$

$$D_{min} = \frac{c_1^2 c_2^2\, \kappa_1^2 \kappa_2^2 e^{-\alpha 2\pi R}}{\left(1 + c_1 c_2 t_1 t_2\, e^{-\alpha 2\pi R}\right)^2} \; . \tag{3.19}$$

If we assume symmetric coupling, the coupling factor and losses are equal, i.e.
$c_1 = c_2 = c$ and $\kappa_1 = \kappa_2 = \kappa$. Then we can define the contrast on the Drop signal as

$$C_D = \frac{D_{max}}{D_{min}} = \frac{\left(1 + c^2 t^2 e^{-\alpha 2\pi R}\right)^2}{\left(1 - c^2 t^2\, e^{-\alpha 2\pi R}\right)^2} \; . \tag{3.20}$$

Inversion of eq. 3.20 gives

$$A = \frac{\sqrt{C_D} - 1}{\sqrt{C_D} + 1} = c^2 t^2\, e^{-\alpha 2\pi R} \; . \tag{3.21}$$

Proceeding in the same manner with the contrast on the Through signal and using 3.20, one obtains

$$C_T = \frac{T_{max}}{T_{min}} = \frac{\left(1 + c^2 e^{-\alpha 2\pi R}\right)^2}{\left(1 - c^2\, e^{-\alpha 2\pi R}\right)^2} \frac{1}{C_D} , \tag{3.22}$$

which implies that

$$B = \frac{\sqrt{C_D C_T} - 1}{\sqrt{C_D C_T} + 1} = c^2\, e^{-\alpha 2\pi R} \; , \tag{3.23}$$

with B a parameter which expresses in pure terms of signal contrasts the total loss given by the sum of the coupling and bent losses. And from eq. 3.21 and 3.23 the contrasts furnish also the information on the coupling coefficients as

$$t^2 = \frac{A}{B} \; . \tag{3.24}$$

To compare the effectiveness of this method to the mode solving approach we measured the contrasts of the Through and Drop in the spectral response of fig. 28 left and obtained the values reported in Table 5.

Table 5: *Through coupling coefficients obtained from mode contrasts.*

t from contrasts (±3%)	t from mode solver
0.927	0.907
0.908	0.890
0.892	0.869
0.872	0.849
0.862	0.824

Within an error of few percent (the fluctuation associated with the measurement error on the contrasts caused by Fabry-Perot noise and other uncertainties) there is a substantial agreement between the two methods. This approach which determines quantitatively the coupling coefficients from the extremal values of the resonant modes by applying eqs. 3.21, 3.23 and 3.24 is simple and has better physical foundations than mere parameter adjustments which fit the simulated versus real spectrum, and can be useful as an experimental validation of mode solving and 3D-FDTD simulations.

We can summarize the conclusions to this section as follows. We analyzed a set of crucial optical and physical properties of racetrack resonators and their constituent waveguides. Assisted by a FVFD mode solver with TBC or UPML boundaries we modelled the straight and curved waveguides, the bend losses, the coupling coefficients and, considering also small effects like phase mismatch, suggested that bends with $2 - 3\mu m$ radius with single-mode waveguides of $0.45\mu m$ widths are a good compromise between the reduction of the radiation losses in the bend and small footprint of the racetrack resonator. Moreover, through experimental characterization of actual devices we could compare the quality of our model and establish accuracies of about 1-2 % in the effective index modelling. And yet this is still not enough to determine optical properties like the FSR and the precise determination of resonant mode wavelengths with a nm precision. We concluded that, at the present, discrepancies should be ascribed to fabrication tolerances than to inadequacies of the theoretical models. Finally we showed that it is possible to determine the coupling coefficients by measuring

the spectral contrasts of a resonator. Other optimizations can of course be pursued (e.g. the modelling of the coupling loss, of the roughness losses or of the asymmetric coupling [73]). However, we believe that the present work summarizes and outlines the main aspects necessary to pave the way to further understanding, control and realization of ultra-compact photonic devices based on small resonators.

4 The Transfer Matrix Method

Nowadays several analytic approaches exist to model the propagation of EM wavefronts and/or the parameters characterizing a photonic structure, like FDTD, beam propagation methods, finite element and finite difference methods, etc. Each of these has pros and cons. For instance FDTD is the best option in order to achieve the most realistic and reliable simulation results and is used as a numeric validation tool before the modeled device is finally sent to fabrication. However, the big disadvantage of FDTD techniques is its slow numerical speed, especially when it computes three dimensional structures. A single simulation can take days, sometimes weeks. On the other side, the transfer matrix approach has been shown to be a reliable matrix analytic tool for modeling optical micro-resonators [59, 40, 60, 61, 45, 24] very quickly (usually less than a minute computing time). Its weak point is that one must already know a priori the parameters characterizing the device (typically the dispersion laws and the coupling constants), and that it furnishes only the final output values of the add-drop resonator structure but doesn't tell nothing about the internal propagation of the EM field inside the device. Nevertheless, thanks to CMT and the details we studied in the preceding section these parameters can be calculated. The next subsections will show how the TMM works, first beginning with a simple introductory example, and then by exposing the detailed calculations.

4.1 A simple introductory approach

Let us outline a simple analytic technique to obtain the elementary transfer matrix between a coupling waveguide and a ring resonator. Here we proceed by reasoning only in terms of power conservation and apply some simple algebraic rules. Standard CMT texts derive it usually through much more elaborate and complicate calculations, resorting to the concepts sketched in section 2. For completeness we will do this too in section 7. However, the following simplified approach wants to be an example to show

that sometimes applying power conservation principles is the most direct route to obtain some coupling relations, and which we will use in particular when more complex optical designs, like in the case of three waveguide systems, will come into the play.
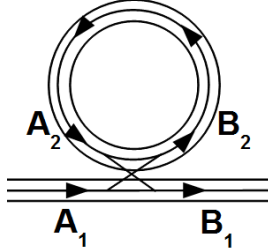

Figure 31: *The ring resonator.*

Let us consider the coupling between a single mode waveguide and a ring resonator (fig. 31), where A_1, A_2, B_1 and B_2 are complex mode amplitudes. We first consider a coupling section $L = 0$, which is the typical approximation for ring resonators. The coupling between the bus waveguide and the ring can be seen as a four port network where the input fields (A_1, A_2) are related to the output fields (B_1, B_2) by a 2x2 complex coupling matrix $\mathbf{M}$, such as

$$\begin{pmatrix} B_1 \\ B_2 \end{pmatrix} = \mathbf{M} \begin{pmatrix} A_1 \\ A_2 \end{pmatrix} = \begin{pmatrix} \kappa_{11} & \kappa_{12} \\ \kappa_{21} & \kappa_{22} \end{pmatrix} \begin{pmatrix} A_1 \\ A_2 \end{pmatrix} , \tag{4.1}$$

where κ_{12} and κ_{21} are the *cross coupling coefficients* and κ_{11} and κ_{22} are the *transmission (or 'straight-through') coupling coefficients.*

If the total input and output modal powers ($\sim$ the squared normalized magnitude of the complex amplitudes) must be the same, then the inner product of every field vector, $<\mathbf{X}, \mathbf{X}> = \mathbf{X}^T \cdot \mathbf{X}^*$, must be invariant under $\mathbf{M}$ as

$$<\mathbf{A}, \mathbf{A}> = <\mathbf{B}, \mathbf{B}> = <\mathbf{MA}, \mathbf{MA}> . \tag{4.2}$$

Eq. 4.2 shows that $\mathbf{M}$ is a unitary matrix, i.e. $\mathbf{M}^\dagger \cdot \mathbf{M} = \mathbf{I}$ and $|\det \mathbf{M}| = 1$.

On the other side, the transmitted and cross-coupling power coefficients are given

respectively by

$$P_T = \left(\frac{|B_1|^2}{|A_1|^2}\right)_{A_2=0} = \left(\frac{|B_2|^2}{|A_2|^2}\right)_{A_1=0} = |\kappa_{11}|^2 = |\kappa_{22}|^2 \equiv |t|^2 \,, \qquad (4.3)$$

and

$$P_C = \left(\frac{|B_1|^2}{|A_2|^2}\right)_{A_1=0} = \left(\frac{|B_2|^2}{|A_1|^2}\right)_{A_2=0} = |\kappa_{12}|^2 = |\kappa_{21}|^2 \equiv |\kappa|^2 \,, \qquad (4.4)$$

and, if there are no losses in the coupling region, it follows immediately

$$|t|^2 + |\kappa|^2 = 1 \,. \qquad (4.5)$$

Eqs. 4.2 and 4.5 represent the energy conservation (or equivalently, the time reversal) for passive devices. In mathematical terms they represent the well known diffeomorphism between the special unitary group SU_2 (the 2×2 unitary and unimodular matrixes with det $\mathbf{M} = 1$) and the points of the 3-dimensional unit sphere S^3 in $\mathbb{R}^4$. A general matrix in $SU_2(\mathbb{C})$ takes the form

$$\mathbf{M} = \begin{pmatrix} t & -\kappa^* \\ \kappa & t^* \end{pmatrix} . \qquad (4.6)$$

For self-coupling there is no phase change. For cross-coupling a π phase change occurs (evanescent waves have always a $\frac{\pi}{2}$ phase difference with respect to the waveguide core field phase), then $t = t^*$ and $\kappa = ik$ with k real, and 4.6 becomes

$$\mathbf{M} = \begin{pmatrix} t & ik \\ ik & t \end{pmatrix} , \qquad (4.7)$$

which fulfills the requirement that in a reciprocal network (losses independent from direction of propagation) the coupling matrix is symmetric. Matrix 4.7 is the basic analytic building block, together with the propagation matrixes which will be discussed in the next section, from which the light propagation in systems of resonators can be calculated.

4.2 TMM for racetracks

In the following we will assume that eq. 4.5 holds because it represents the ideal reference case. But a notice of care is necessary nevertheless. Coupling losses arise at each resonator and are difficult to estimate since they depend strongly from the type and quality of technology employed. They are usually neglected in a theoretical discussion because they are relatively small for a single resonator, but might become relevant for several ones as in a SCISSOR. In addition, it has been also shown that a particular case where eq. 4.5 is not valid occurs when the air-gap between the bus waveguide and the ring becomes very narrow, less than 120 nm for a 220x530 nm SOI waveguide, due to mode conversion losses [34]. Therefore, care must be taken when working with many resonators and small gaps. For this purpose we introduce coupling losses analytically by reformulating eq. 4.5 through eq. 4.7 as

$$\det \mathbf{M} = t^2 + k^2 = c^2 \leq 1 \,, \tag{4.8}$$

where c represents the coupling loss parameter. Note that for a system of n cascaded equal resonators the power lost due to coupling losses, for instance along the Through port waveguide, scales as $1 - c^{2n}$.
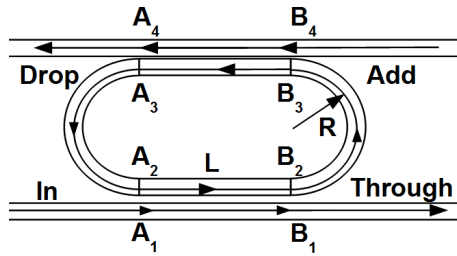

Figure 32: *The racetrack resonator.*

Now, for racetrack resonators (fig. 32), the coupling length L is finite. Then, according to 4.1 and 4.7, we write

$$\begin{pmatrix} B_1 \\ B_2 \end{pmatrix} = \begin{pmatrix} t & ik \\ ik & t \end{pmatrix} \begin{pmatrix} A_1 \\ A_2 \end{pmatrix} e^{i\beta L} \,, \tag{4.9}$$

where $\beta = \frac{2\pi}{\lambda} n_{eff}$ is the real part of the propagation constant in the straight section, and n_{eff} the effective index of the guided mode. In eq. 4.9, the phase delay due to propagation in the straight section is taken into account by the exponential function.

For a generic matrix $\mathbf{A} = \begin{pmatrix} a & b \\ c & d \end{pmatrix}$ the following relation holds

$$\begin{pmatrix} X' \\ Y' \end{pmatrix} = \mathbf{A} \begin{pmatrix} X \\ Y \end{pmatrix} \Rightarrow \begin{pmatrix} Y \\ Y' \end{pmatrix} = \frac{1}{b} \begin{pmatrix} -a & 1 \\ -\det \mathbf{A} & d \end{pmatrix} \begin{pmatrix} X \\ X' \end{pmatrix}. \quad (4.10)$$

Then, by using eq. 4.8, 4.9 and 4.10, the coupling matrix $\mathbf{K}^1$ which relates (A_1, B_1) to (A_2, B_2) (fig. 32) is

$$\begin{pmatrix} A_2 \\ B_2 \end{pmatrix} = \mathbf{K}^1 \begin{pmatrix} A_1 \\ B_1 \end{pmatrix} = \frac{1}{ik} \begin{pmatrix} -t & e^{-i\beta L} \\ -c^2 e^{i\beta L} & t \end{pmatrix} \begin{pmatrix} A_1 \\ B_1 \end{pmatrix}. \quad (4.11)$$

Considering losses and phase shifts, the (forward and backwards) internal propagation matrix $\mathbf{P}$ for the racetrack is

$$\begin{pmatrix} B_3 \\ A_3 \end{pmatrix} = \mathbf{P} \begin{pmatrix} A_2 \\ B_2 \end{pmatrix} = \begin{pmatrix} 0 & a\, e^{i\beta\pi R} \\ \frac{1}{a} e^{-i\beta\pi R} & 0 \end{pmatrix} \begin{pmatrix} A_2 \\ B_2 \end{pmatrix}, \quad (4.12)$$

where $a = e^{-\alpha\pi R}$ is the half round trip loss factor, α the total loss per unit length, and R the curvature radius. Note that the direction of propagation of the traveling wave in the resonator and in the coupling should be considered carefully as done in eq. 4.12.

The coupling matrix for $(B_3, A_3) \rightarrow (B_4, A_4)$ is obtained in the same way as eq. 4.11. For asymmetric coupling two different coupling matrixes $\mathbf{K_1}$ and $\mathbf{K_2}$ should be used. For some applications it might be advantageous to choose them independently (e.g. [73, 25]). Therefore, the total transfer matrix $\mathbf{T}$ for the single racetrack of fig. 32 is

$$\begin{pmatrix} B_4 \\ A_4 \end{pmatrix} = \mathbf{T} \begin{pmatrix} A_1 \\ B_1 \end{pmatrix} = \mathbf{K_2} \cdot \mathbf{P} \cdot \mathbf{K_1} \begin{pmatrix} A_1 \\ B_1 \end{pmatrix}. \quad (4.13)$$
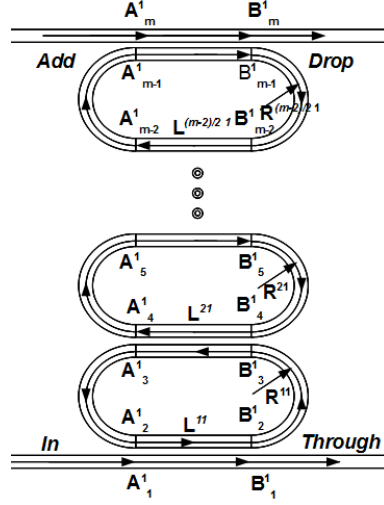
58

Figure 33: *The racetrack CROW.*

It is now possible to extend the transfer matrix model to a CROW structure, as shown in fig. 33. In general racetracks can be assembled in a matrix such as in fig. 33. For this reason, let us consider a matrix of resonators, each one is characterized by the four port fields A_l^j and B_l^j, with ($l = 1..m$ the resonator row index and $j = 1..n$ the resonator column index). Each racetrack resonator has its own upper and lower coupling constants, i.e. for every i-th row and j-th column there is a coupling matrix $\mathbf{K}^{ij}$. Analogously there is an internal propagation matrix $\mathbf{P}^{ij}$, and a length and radius parameter L^{ij} and R^{ij} respectively.

The total transfer matrix $\mathcal{T}^1$ for a CROW, is a generalization of eq. 4.13 as follows

$$\begin{pmatrix} A_m^1 \\ B_m^1 \end{pmatrix} = \mathcal{T}^1 \begin{pmatrix} A_1^1 \\ B_1^1 \end{pmatrix} = \mathbf{K}^{\frac{m}{2}1} \cdot \prod_{i=1}^{m/2-1} \mathbf{P}^{i1} \cdot \mathbf{K}^{i1} \begin{pmatrix} A_1^1 \\ B_1^1 \end{pmatrix}, \tag{4.14}$$

with ($m = 4, 6, 8, ...$). Please note that the transfer matrix formalism reflects the direction of the input and output signals. Depending whether the number of rows is odd or even, the output signal in resonance with the CROW will travel in the opposite or in the same direction of the input signal, respectively. The field vector elements of eq. 4.13 and 4.14 are exchanged accordingly (the former is written according to fig. 32 the latter and following equations to fig. 33).

Transfer matrixes $\mathbf{K}^{ij}$, $\mathbf{T}$ and $\mathcal{T}^1$ are involutions, i.e. they are equivalent to their own inverse and $\det \mathbf{K}^{ij} = \det \mathbf{P} = -1$, which implies $\det \mathbf{T} = \det \mathcal{T}^1 = -1$, always. Therefore, once the fields A_1^1 at port In and A_m^1 at port Add are defined, it is then straightforward, by applying eq. 4.10, to obtain the single resonator's behavior at the $Through$ and $Drop$ ports B_1^1 and B_m^1 as

$$
\begin{pmatrix} B_1^1 \\ B_m^1 \end{pmatrix} = \frac{1}{T_{12}} \begin{pmatrix} -T_{11} & 1 \\ 1 & T_{22} \end{pmatrix} \begin{pmatrix} A_1^1 \\ A_m^1 \end{pmatrix} , \tag{4.15}
$$

with $T_{ij}, (i, j = 1, 2)$ the elements of the transfer matrix $\mathcal{T}^1$. For most applications A_m^1 is set to zero, but this is not necessary. Eq. 4.15 holds provided that the signals are not contra-directional.
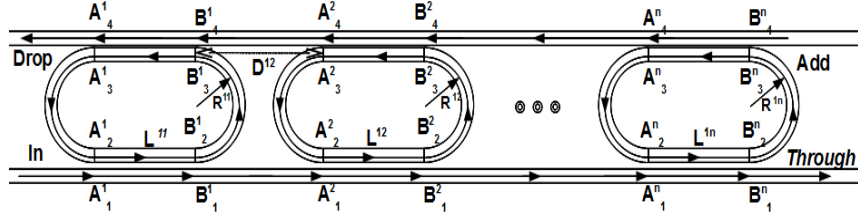

Figure 34: *The dc-SCISSOR.*

Let us consider a double channel SCISSOR (dc-SCISSOR), as shown in fig. 34. Proceeding as have been done in 4.10, the relation $(A_1^1, A_4^1) \to (B_1^1, B_4^1)$ can be obtained from 4.13 (extending the indexing accordingly). This leads to a 'scattering matrix' $\mathbf{S}^{11}$ as

$$
\begin{pmatrix} B_1^1 \\ B_4^1 \end{pmatrix} = \mathbf{S}^{11} \begin{pmatrix} A_1^1 \\ A_4^1 \end{pmatrix} = \frac{1}{T_{22}} \begin{pmatrix} -T_{21} & 1 \\ -1 & T_{12} \end{pmatrix} \begin{pmatrix} A_1^1 \\ A_4^1 \end{pmatrix} . \tag{4.16}
$$

We can introduce an external propagation matrix $\mathbf{Q}^{j\,j+1}$ connecting the j-th to j+1-th column resonator, which in the case of the first and second racetrack is defined by

$$
\begin{pmatrix} A_1^2 \\ A_4^2 \end{pmatrix} = \mathbf{Q}^{12} \begin{pmatrix} B_1^1 \\ B_4^1 \end{pmatrix} = \begin{pmatrix} e^{i\beta D^{12}} & 0 \\ 0 & e^{-i\beta D^{12}} \end{pmatrix} \begin{pmatrix} B_1^1 \\ B_4^1 \end{pmatrix} , \tag{4.17}
$$

60

where D^{12} is the distance separating the resonator's first from second straight arm, as shown in fig. 34.

Applying another scattering matrix for the second resonator $\mathbf{S}^{12}$ and putting together eq. 4.16 and 4.17 gives

$$
\begin{pmatrix} B_1^2 \\ B_4^2 \end{pmatrix} = \mathbf{S}^{12} \cdot \mathbf{Q}^{12} \cdot \mathbf{S}^{11} \begin{pmatrix} A_1^1 \\ A_4^1 \end{pmatrix}. \tag{4.18}
$$

The complete description of the single SCISSOR structure through the scattering matrix $\mathcal{S}_\mathbf{x}^\mathbf{1}$ is now straightforward

$$
\begin{pmatrix} B_1^n \\ B_4^n \end{pmatrix} = \mathcal{S}_\mathbf{x}^\mathbf{1} \begin{pmatrix} A_1^1 \\ A_4^1 \end{pmatrix} = \mathbf{S}^{1n} \cdot \prod_{j=1}^{n-1} \mathbf{Q}^{j\,j+1} \cdot \mathbf{S}^{1j} \begin{pmatrix} A_1^1 \\ A_4^1 \end{pmatrix} ; n \geq 2. \tag{4.19}
$$

Considering that $\det \mathbf{S}^{1j} = \det \mathbf{Q}^{j\,j+1} = 1$ implies $\det \mathcal{S}_\mathbf{x}^\mathbf{1} = 1$, the analogue of eq. 4.15 for the SCISSOR is then

$$
\begin{pmatrix} B_1^n \\ A_4^1 \end{pmatrix} = \frac{1}{S_{22}} \begin{pmatrix} 1 & S_{12} \\ -S_{21} & 1 \end{pmatrix} \begin{pmatrix} A_1^1 \\ B_4^n \end{pmatrix}, \tag{4.20}
$$

with $S_{ij}, (i, j = 1, 2)$ the elements of the scattering matrix $\mathcal{S}_\mathbf{x}^\mathbf{1}$. For the single resonator cell it reduces to eq. 4.15 showing that $T_{22} = -T_{11}$.

Finally we can extend this approach to serially-parallel cascaded resonators, or the twisted dc-SCISSOR, as shown in fig. 35.

Again, applying eq. 4.10 to the column transfer matrix of each CROW $\mathcal{T}^j$, $(j = 1, .., n)$, we obtain the scattering matrix $\mathcal{S}_y^j$ which relates fields (A_1^j, A_m^j) to (B_1^j, B_m^j), and going through the same steps of eq. 4.16 to 4.19 leads to

$$
\begin{pmatrix} B_1^n \\ B_m^n \end{pmatrix} = \mathcal{S}_\mathbf{y}^\mathbf{n} \cdot \prod_{j=1}^{n-1} \mathbf{Q}^{j\,j+1} \cdot \mathcal{S}_\mathbf{y}^\mathbf{j} \begin{pmatrix} A_1^1 \\ A_m^1 \end{pmatrix} ; \qquad n \geq 2, \tag{4.21}
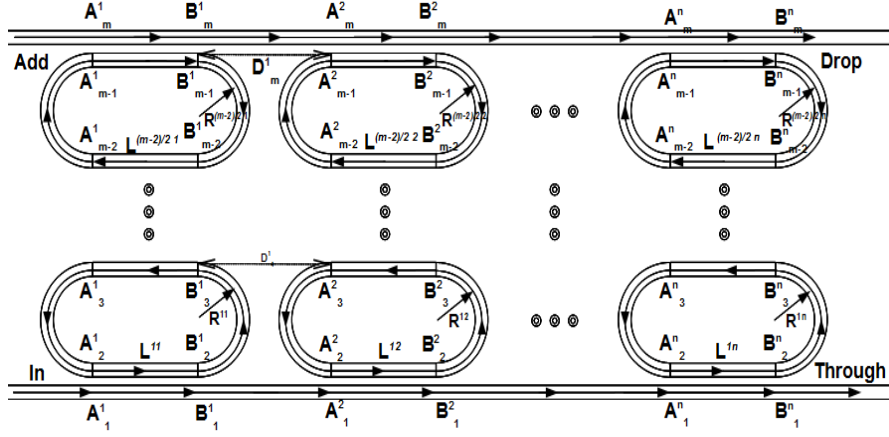$$

Figure 35: *The twisted dc-SCISSOR.*

which is a linear system in two unknowns and two known variables, therefore resolvable.

Note that, it is also possible to think in terms of power conservation. If we consider a generic device, not necessarily a single resonator, but any possible SCISSOR (or CROW) as a black box network with an Input, a Through, a Drop and an Add port, it must hold that the loss is given by

$$Loss = |A_{In}|^2 - |A_D|^2 - |A_{Th}|^2 = I_{In} - I_D - I_{Th} \,, \tag{4.22}$$

where each element refers to the power measured in the corresponding port. From now on we will label the In, Through, Drop and Add ports amplitudes and intensities as A_{In}, A_{Th}, A_D, A_{Ad} and I_{In}, I_{Th}, I_D, I_{Ad} respectively.

We can express this with eq. 4.20 (or eq. 4.15) in terms of the scattering (or transfer) matrix elements, and obtain

$$Loss_S = \left(1 - \left|\frac{S_{21}}{S_{22}}\right|^2 - \left|\frac{1}{S_{22}}\right|^2\right) * |A_1^1|^2 \,, \tag{4.23}$$

for the SCISSOR, and

$$Loss_C = \left(1 - \left|\frac{1}{T_{12}}\right|^2 - \left|\frac{T_{11}}{T_{12}}\right|^2\right) * |A_1^1|^2 \,, \tag{4.24}$$

for the CROW. Tough the information on the phase are lost, there can be situations where this approach is useful.

4.3 Examples of TMM simulations and fabrication errors analysis

At this point we had sufficient data and knowledge of the analytical theory to write a simulation software code to analyze the resonant structures spectral behavior (we implemented it as a Matlab code). As an example we model a SCISSOR based on the SOI waveguides discussed in chapter 3 (220nm core thickness, 0.5 μm width, $2\mu m$ and $0.75\mu m$ buffer and SiO_2 top cladding thicknesses, respectively) and made of equal racetrack resonators ($L = 10\,\mu m$, $R = 3.25\,\mu m$, and 0.024 dB/90° bend loss). The spacing D between the resonators is fixed to obtain coherent superposition. Its length can be calculated as follows. The resonant wavelength of the m-th resonator mode is

$$\lambda_m = n_{eff}\frac{2L + 2\pi R}{m}\,,\tag{4.25}$$

and the phase shifts introduced by the resonators and by their separation at some wavelength λ are, respectively,

$$\Phi_R = \frac{2\pi}{\lambda}n_{eff}\pi R\,; \qquad \Phi_B = \frac{2\pi}{\lambda}n_{eff}(2L + 2D + \pi R)\,.\tag{4.26}$$

At resonance ($\lambda = \lambda_m$), the phase difference must be

$$\Delta\Phi = \Phi_B - \Phi_R = \frac{2\pi}{\lambda_m}n_{eff}(2L + 2D) = 2\pi\,n,\tag{4.27}$$

with $n \geq 1$ an integer multiple. From this and eq. 4.25 the coherence condition fixes the length D as

$$D = L\left(\frac{n}{m} - 1\right) + \frac{n}{m}\pi R\tag{4.28}$$

where the simplest case with $n = m$ (i.e., the Free Spectral Range (FSR) of the resonator and Bragg modes is set to be identical) leads to an inter-resonator distance $D = \pi R$ independent from the racetrack length L.

Now we can build analytically the resonator sequences. Since we are considering all resonators equal we will drop the indices in the formalism. For example, for a single row of racetrack SCISSOR, one must use the matrix $\mathbf{T} = \mathbf{K} \cdot \mathbf{P} \cdot \mathbf{K}$ of the first resonator cell

in eq. 4.13 (or $\mathcal{T}^1$ in eq. 4.14 with m=4) with $\mathbf{K}$ and $\mathbf{P}$ given in eq. 4.11 and 4.12 respectively. $\mathbf{T}$ gives the spectral output of the single resonator via eq. 4.15. Then, from the elements of $\mathbf{T}$, the scattering matrix $\mathbf{S}$ (eq. 4.16) is obtained. The external propagation matrix $\mathbf{Q}$ is given by eq. 4.17, and the total scattering matrix $\mathcal{S}_x^1$ by 4.19 with n=2, 4, 8 for the 2, 4, 8 element SCISSOR, respectively. Finally, the Through and Drop port outputs are obtained by eq. 4.20. Whereas for the CROW structure one proceeds in a similar way but by applying eq. 4.14 only and with $m = 4, 6, 8, 10$ for the case of the structures of 1,2,4,8 cascaded resonators respectively.

In principle this should be sufficient to simulate the desired spectrum. There is however a practical drawback. Devices which must fulfill a coherence condition are highly sensitive to the statistical disorder induced by the technological process in use.

Experimentally, fabrication tolerances can have important repercussions on the performance of the structure[29]. Etching and photoresist exposure are the main photolithographic processes which contribute to random statistical disorder at the nanometer scale. At a scale of about 5nm the SCISSOR bends, the waveguide width, the gap spacings, and other parameters are affected by random fluctuations caused by these fabrication imperfections. This implies that the optical paths of the resonators in a SCISSOR, as also its mutual inter-resonator distances, are slightly randomized with respect to the nominal parameters. For our applications of interest this has important consequences. At present, this spectrum impairment sets the main practical problems, which however will possibly be solved or mitigated with next generation lithographic technologies.

To have a measure of the spectral impairment which might occur due to fabrication errors, we assume a $\pm 5nm$ random shift in the inter-resonator distance D from the ideal value of eq. 4.28 and on the curvature radius R. Fig. 36 (left) shows the ideal case for the SCISSOR with 1,2,4 and 8 racetracks (blue, green, brown, and red lines respectively), and the same structure simulated again introducing a $\pm 5nm$ uniform

random fluctuation (fig. 36 right). Independently from the number of resonators involved the FSR remains the same but it is possible to choose different finesse (FSR/$\Delta\lambda$). Note also how on resonance light is recovered in the 8 racetrack SCISSOR versus the single resonator.

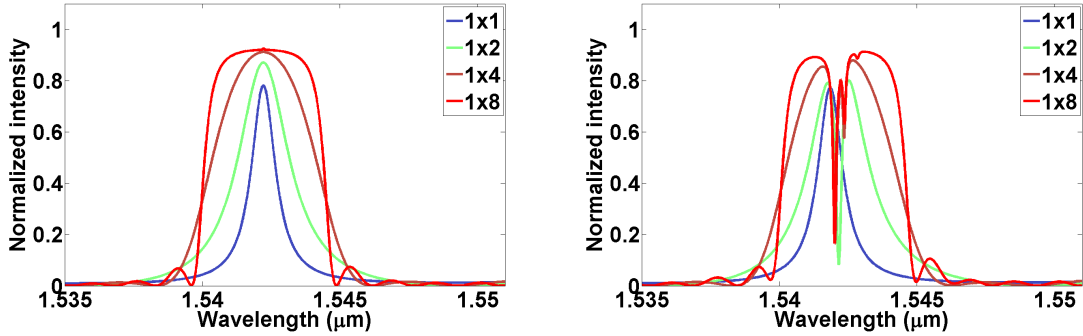**Figure 36:** *The Drop port signal of an ideal $1 \times (1, 2, 4, 8)$ SCISSOR (left) and the same with a $\pm 5nm$ randomization of the separation distances and curvature radii.*

Characteristic for the dc-SCISSOR structure is its flat box spectrum increase in spectral width with the increases of the number of resonators. As we will see later, this is why dc-SCISSOR structures are particularly useful for band routing applications. Longer chains of coupled resonators produce resonant modes with larger full width at half maximum (FWHM), i.e. a response where the modes change from a channel behavior (higher quality factor and smaller width, $\Delta\lambda$, at FWHM) to band like behavior (lower quality factor and larger $\Delta\lambda$). According to the number of cascaded resonators the spectrum will be characterized by a higher order filter behavior and, when the inter-resonator distance is carefully chosen (in our case $\pi R = 10.21\mu m$) so that the resonator modes and the Bragg modes will overlap, then also a larger FSR will be obtained [21, 22, 23, 24, 25, 26, 74]. Therefore, it is possible to accomplish channel or band routing according to the number of resonators one chooses.

However, it is observed that the fine tuning of D and R is critical to maintain coherence: for a 5 nm departure dips appear in the Drop spectrum due to the lost constructive interference conditions. This can be seen as a spectrum impairment, or on the contrary,

as very high Q resonances due to this nanometric structural disorder. These transmission dips are a manifestation of the Coupled Resonator Induced Transparency (CRIT), i.e. the optical microresonator analog of Electromagnetic Induced Transparency (EIT), where light is not coupled into the resonators at their resonant frequency ([47, 48]) and are a signature for large group index and slow light phenomena. For several resonators this manifests in multiple CRIT phenomena ([49, 50]), because the offset in the inter-resonator distance induces a slight shift between the resonators and Bragg modes. These have also been studied recently [29].

The same comparison has been made with an ideal and randomized $(1, 2, 4, 8) \times 1$ CROW structure, a shown in fig. 37 left and right respectively. The ideal spectrum shows the characteristic CROW (1,2,4,8) Drop port dips (the lateral dips are however barely discernable). This time the randomization was applied obviously only on the radius of the racetracks and qualitatively one sees that the sensitivity to the same magnitude of fabrication errors in a CROW can be considered less detrimental than those occurring for the SCISSOR.
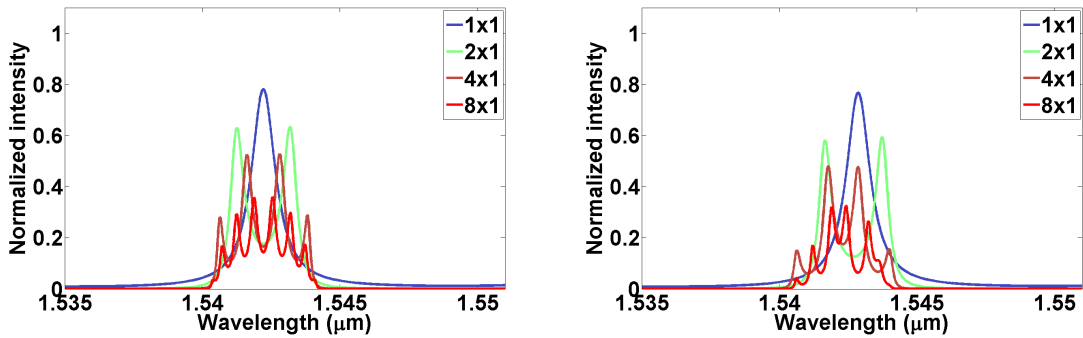
Figure 37: *The Drop port signal of an ideal $(1, 2, 4, 8) \times 1$ CROW (left) and the same with a $\pm 5nm$ randomization of the curvature radii.*

In order to try to quantify this effect the following numerical experiment was done. The spectral deviation from that of an ideal SCISSOR of eight racetracks with the above mentioned properties was estimated. A random parameter fluctuation range was set in $\pm \Delta$ nm on each parameter (eg. $L \pm \Delta$ nm, etc.). By randomizing the parameters (i.e.

66

Figure 38: *Estimate of the spectral noise intensity with increasing parameter randomization in a 1×8 SCISSOR.*

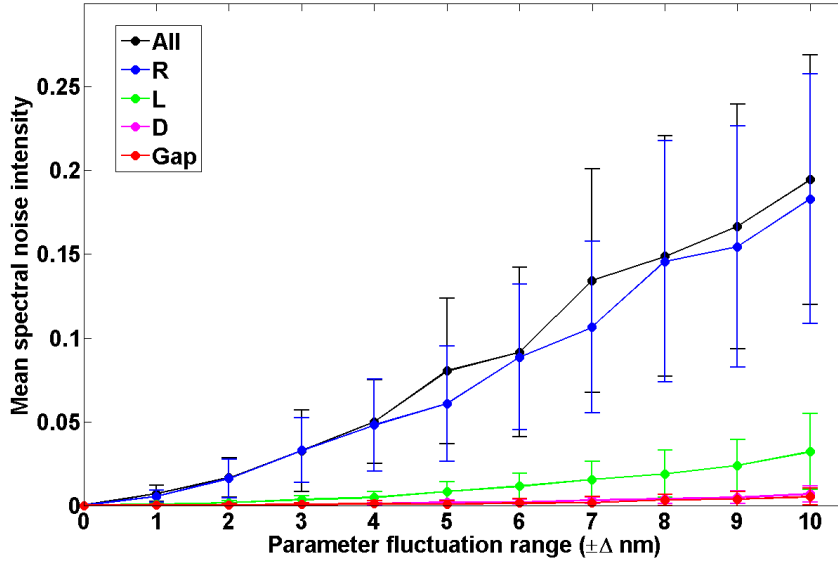the coupling section length L, the radius of the bends R, the inter resonator distance D, the gap, and finally all these together), the induced 'noise', or mean 'spectral noise intensity', $SNI(\Delta)$, was determined. This quantity was calculated as a mean normalized power loss of the ideal signal, i.e. unity minus the numerical integral of the fraction between the normalized intensity of the ideal spectral curve, $I(\lambda)$, over that obtained with parameter randomization Δ, $I'(\lambda, \Delta)$, over the spectral domain of one mode, D_λ. In formula:

$$SNI(\Delta) = 1 - \frac{1}{D_\lambda} \int_{D_\lambda} \frac{I(\lambda)}{I'(\lambda, \Delta)} \, d\lambda \approx 1 - \frac{1}{N} \sum_{i=1}^{N} \frac{I(\lambda_i)}{I'(\lambda_i, \Delta)} \,, \qquad (4.29)$$

where the right hand term is the numerical approximation, and $N = D_\lambda / \Delta\lambda$ the number of wavelength steps over D_λ, with $\Delta\lambda$ the wavelength step size used in the numerical integration (here of $\Delta\lambda$=0.01nm). Then, for a specific parameter fluctuation, running the TMM code simulation one obtains a perturbed spectrum, and from this a specific 'noise' value. This simulation was run 100 times to obtain a statistical mean and a standard deviation. This procedure is repeated for 10 parameter randomizations from 1 to 10 nm. Fig. 38 shows the so obtained results with standard deviation error

bars. One can notice that the red, magenta and green lines, those representing the spectral impairment induced because of the fabrication errors over the gap, the inter resonator distances and the coupling section lengths respectively, contribute to the total spectral impairment (black line) much less than that caused by the errors on the radius of the racetracks bends (blue line). This is natural, since an error on the radius determines π times an error on the bend length, and correspondingly more phase shift. The perturbation of the spectrum can be approximately seen as a function growing linearly with randomization. This does however not convey the real effect of fabrication errors, it is instead the non negligible scattering around the mean represented by the error bars. In practical terms this means that one has to expect large differences in the spectral quality over every fabricated SCISSOR device, also if the fabrication technology remains the same.

Therefore, one must always keep in mind that SCISSOR structures are very sensitive also to tiny departures from some nominal theoretical values and when real SCISSOR devices must be fabricated for practical purposes it is of extreme importance to carefully evaluate the effects that the statistical fabrication disorders produce on the desired performance.

Another aspect which was worth of some attention was the question if also the fluctuations in the waveguide structure itself could have damaging effects on the spectral performance of the devices. Looking at a Scanning Electron Microscope (SEM) image of a silicon waveguide one can notice a slight but possibly non negligible fluctuation in its width along its length. The effective index and its dispersive properties depend strongly form the geometrical structure of the waveguide. The problem is that randomizations induced on the waveguide widths and its core height can therefore lead to effective- and group- index, as group velocity dispersion (GVD) variations compared to the expected one, which in turn can potentially alter the device performance considerably. On the other side if the total length of the waveguides in a device is large enough, one can expect that these fluctuations are statistically smoothed out and can be considered

negligible nevertheless. The question arises if the structures in our devices, for instance the coupling section in a racetrack of L=10 μm, are long enough to obtain this statistical smoothing? We answer this question positively for the following reasons.
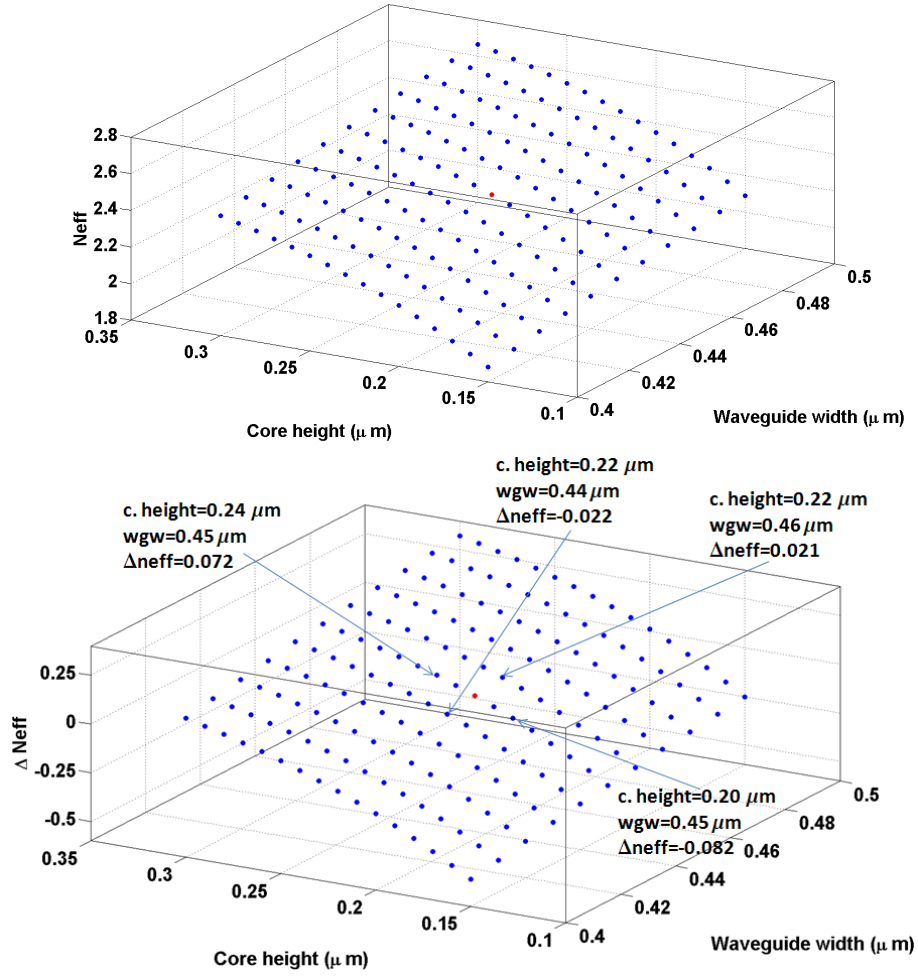
Figure 39: *The dependence of the effective index (top) and the deviation of the effective index from the nominal waveguide (red spot at wgw=0.45μm and core height 0.22μm), at $\lambda = 1.55\mu m$ in TE-polarization.*

Extending the calculations done in section 3, an array of data were processed which relate the waveguide width and the core height with the effective index, and the deviations in the effective index of all the waveguide structures from the nominal one of 0.45μm width and 0.22μm core height. Fig. 39 top shows the distribution of effective indexes around the nominal waveguide indicated by the red spot at telecom wavelength

of $\lambda = 1.55\mu m$, in TE-polarization.

The deviation of the effective index from the nominal waveguide is shown in fig. 39 bottom. It represents the same data of fig. 39 top but with the effective index of the nominal waveguide ($n_{eff} = 2.34$) subtracted to highlight the differences. This conveys some information on the effective index variation to be expected due to lithographic imperfections. For example LETI declares an error on $220 \pm 20nm$ on the core height. According to this calculation, as indicated by the arrows and labels in fig. 39 bottom, the variation of the core height from 0.20 to 0.24 μm, for a constant waveguide width of 0.45 μm, amounts to a variation in the effective index of about $\Delta_{neff} = 0.154$. On the other side, maintaining the core height at 220 nm and varying the waveguide width from 0.44 μm to 0.46 μm, induces an effective index change of about $\Delta_{neff} = 0.043$. Therefore, in TE-polarization, the sensitivity to imperfections in the core height is almost four times larger than those to waveguide width. Fortunately this is not a real problem since the error on the silicon layer height is mainly caused by the epitaxial layering process during fabrication. Once the wafer is produced, tough not having the nominal height of 220nm, it will have nevertheless a uniform height of the silicon layer over the whole surface. Not so for the waveguide width fluctuations which are caused by the photoresist and the etching process imperfections, i.e. they are present from point to point in the real device. From the above calculations one can estimate that for a waveguide width of 0.45 μm and randomization of about $\pm$ 5 nm (a typical order of magnitude of mean fluctuation inferred from SEM images), an effective index variation of at least $\Delta_{neff} = 0.02$ should be expected. This should induce on a waveguide of $L = 10\mu m$ length the same optical phase shift equal to another waveguide of length $L' = L(1 + \Delta_{neff}/neff)$. In our case it would be of about $L' = 10.085\mu m$, i.e. optical length fluctuations, caused by the effective index variations due to waveguide fluctuations, up to 85 nm, which would lead to huge spectrum impairments. This has not been observed. Which means that on lengths of the order of $10\mu m$ the fabrication imperfections have been smoothed out statistically, and that one does not have to worry

too much about waveguide and core height fluctuations for devices whose footprint is larger than 100 μm^2.
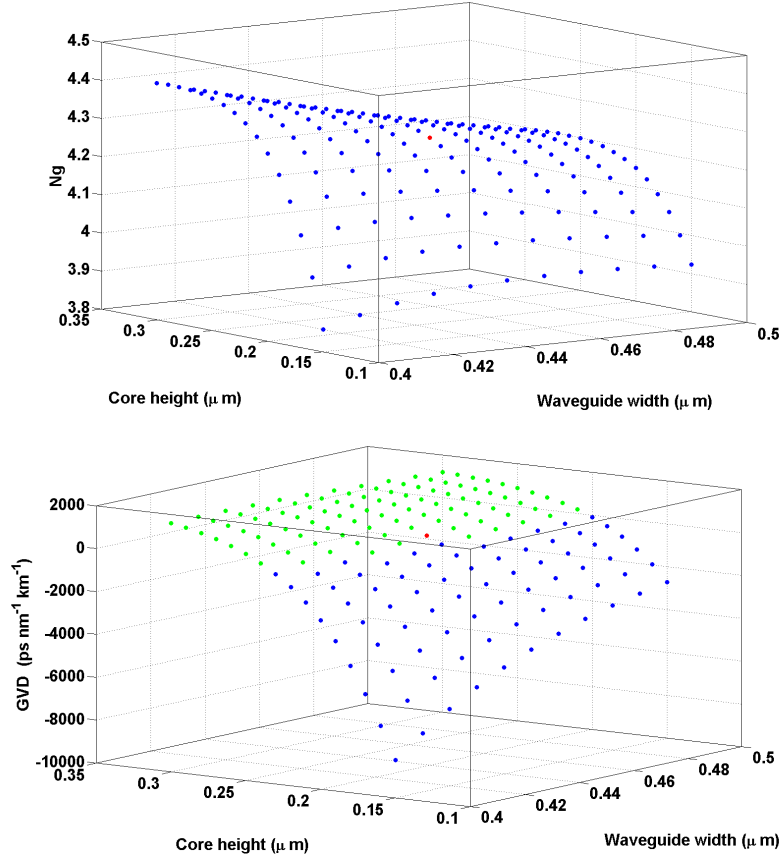

Figure 40: *The dependence of the group index (top) and the GVD (bottom; green points: anomalous diesperison; blue points: normal dispersion) from waveguide width and core height at $\lambda = 1.55\mu m$ in TE-polarization (red spot at wgw=0.45μm and core height 0.22μm).*

For completeness we add also the graphs for the the group index and the GVD at telecom wavelength of $\lambda = 1.55\mu m$, again in TE-polarization. These have been obtained directly from the wavelength dependence of the effective indexes for each waveguide width and core height resorting to eq. 3.10 and eq. 3.11 (modified to a third order polynomial regression to obtain higher accuracy in the derivatives). Fig. 40 top shows the distribution of the group index. The nominal waveguide (red spot) lies on a point of the surface where the steepness is quickly increasing. Which means that, for deviations from the theoretical waveguide, and because of eq. 3.13 and eq. 3.15, this can also have

non negligible effects on the FSR. But perhaps the most interesting fact can be seen in fig. 40 bottom for the GVD distribution. The green points represent the set of waveguide widths and core heights for which anomalous optical dispersion occurs (high frequency components travel faster than the lower ones), while conversely the blue points show the region of normal dispersion (low frequency components travel faster than the higher ones). The nominal waveguide turns out to be only slightly normally dispersive but is placed very near to the zero GVD line. This can be very useful for optical pulse shaping minimizing pulse broadening since, as well known, dispersive effects induce temporal spreading of the light pulses representing bit-streams and which will spread in time, merging together, and rendering the bit-stream unintelligible.

Despite the above mentioned limitations on the spectral impairment, these latter aspects on statistical smoothing of the waveguide fluctuations and the near zero GVD of the nominal waveguide were more encouraging elements, and therefore it was worth to concentrate our efforts on the practical realization of SCISSOR devices.

.

5 Design and Validation by Optical Testing

5.1 Mask design and wafer fabrication

Once the theoretical and analytic aspects were clarified the phase of the concept layout, mask design and wafer fabrication supported by the numerical investigation of the test devices was initiated. The modeling and simulation of photonic integrated circuit (PIC) was realized essentially by the interaction of three complementary activities. First that of parameter estimation by determining the wavelength dependent racetrack's coupling lengths, the coupling coefficients and obtain from these the proper gap spacings with a full vectorial finite difference mode solver (as explained in section 3, and as published in [74]). Secondly, with the so obtained parameters, we perform simulations of the spectral response of the single SCISSOR, CROW and its combination to analyze the Drop and Through signals behavior with varying phase difference at the Input ports. This was done by describing the resonators collective effect with the TMM (see section 4). Finally we performed the simulations of silicon device components like the crossings, the MMI splitters, and tapers which were done through FDTD packages. This furnished an estimate of the losses and crosstalk we had to expect for the real devices. All the mentioned parameters and design specifications were intended for TE-polarization.

As to the type of fabrication employed, the devices were produced using LETI and IMEC photonic process technologies [75] on 200mm SOI wafers. These were fabricated with a 220nm thickness Si crystalline film on $2\mu m$ buried oxide substrate and a SiO_2 top cladding of $0.75\mu m$. The mask was DUV 193nm lithography. We opted also for different exposure doses so that some critical feature sizes change as the exposure dose varies (each column in the matrix of dies on the wafer is printed with a certain dose so that the feature size varies from one side to the other of the wafer). This made it possible to design several different devices with slightly different parameters on the mask, like the waveguide width and the spacings. These were $0.5\mu m$ or $0.45\mu m$ for the waveguide widths and spacings of 160, 180 or 200nm with section lengths coupled to the

Through and Drop port waveguides of $L = 7.5, 10, 15\mu m$. The curvature radius for the bend sections of the racetracks was $R = 3.25\mu m$. The bend losses were obtained by evaluating the light absorbtion on a chain of 100 serially adjoint bends of the same type. A loss of about $-0.025 dB/90°$ was measured ([76]). Light insertion and extraction was realized by coupling a $2\mu m$ diameter fiber to a $2\mu m$ wide waveguide on chip, which then shrinks adiabatically for $500\mu m$ down to the $0.5\mu m$ or $0.45\mu m$ waveguides.
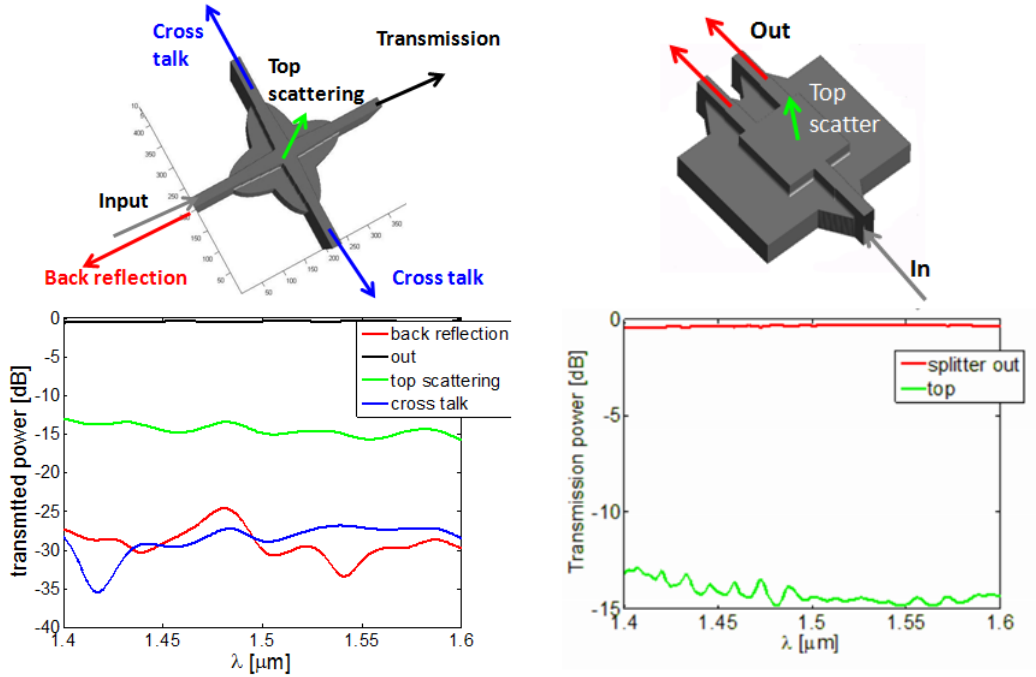

Figure 41: *Layout and simulation results of the double etched crossing with elliptical mode expansion (left) and the MMI splitter (right), and respective graphs of the reflections, cross talk and scattering.*

Some components like crossings and MMI splitters were processed in two etch layers, first a shallow etch of 70nm followed by a deep etching. The crossing employed were designed on a model of elliptical mode expansion of the waveguide core [77] minimizing the losses due to diffraction of the waves lateral broadening at the intersection region (shallow etching reduces the lateral index contrast lowering further the diffraction, back-reflections and crosstalk). The layout and some simulation results are shown in fig. 41 left.

Measurements on a chain of cascaded devices show -0.35 dB loss per crossing confirming

the simulation results which indicated also a crosstalk mean value of about $-27dB$, back-reflection of 0.17% with a major contribution to losses of 3.6% because of top scattering. The MMI splitters (see fig. 41 right) used a similar two layer technology [8] and had about -0.4dB total loss and 4.5% top scattering, but showed also to be affected by strong imbalance between the two output arms (possibly due to layer misalignment during the fabrication process, or other unknown causes). This imbalance made it very difficult to use the reference signals for data normalization. A careful analysis later showed that a $0.5\mu m$ wide waveguide is no longer strictly single mode but already the second mode appears at telecom wavelengths, and that this might have contributed to the MMI imbalance. Fortunately this did in no way impair the performance of the other devices since this second mode is very lossy and does not disturb the measurements anyway. However, this resulted in the fabrication of some wafers with the waveguide of $0.5\mu m$ width while later we switched to $0.45\mu m$ width waveguides, which are definitely single mode.

The next page illustrates some snapshots of the wafer produced and the GDS II designed with an appropriate mask layout design software [78]. Fig. 42 shows a microscope image of the die in the background making the silicon circuits visible. Some parts are magnified where crossings and MMI splitters were present and making the double etching visible. On the lower left a photograph of the wafer was inserted. The right column of fig. 43 is a layout of the PIC designed with the GDS II format. Some parts are magnified to show the graphical aspect of some devices as they have been fabricated. On the right the SEM image of racetracks, crossings and MMI splitters has been added.

5.2 Some first optical tests and validations

The wafers contained also some optical test structures which served as reference and furnished some quantitative features essential for the overall understanding of the performance and quality of the routing devices. For example, before testing the full
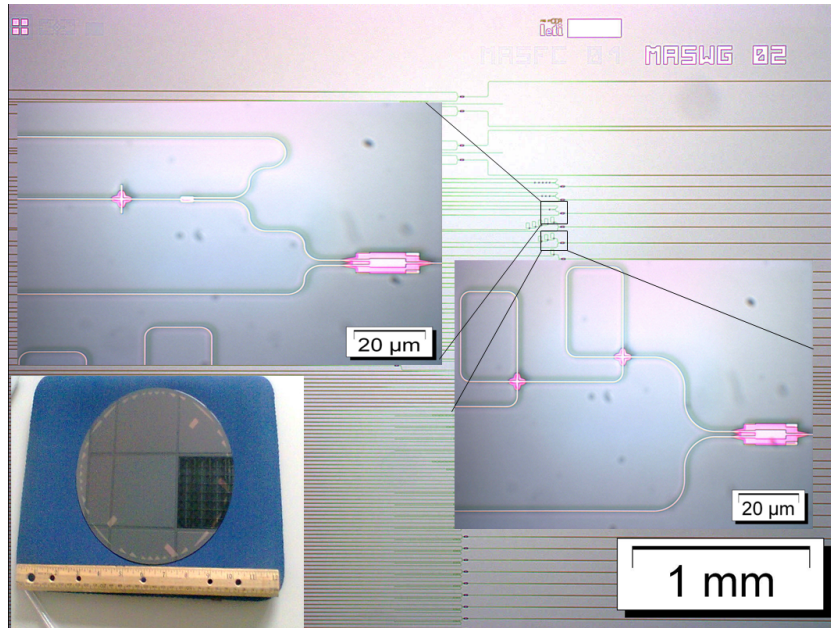
Figure 42: *Optical microscope pictures of the silicon circuits, zoom on the MMI splitters and crossings, and the wafer (lower left). Fabrication technology: LETI.*

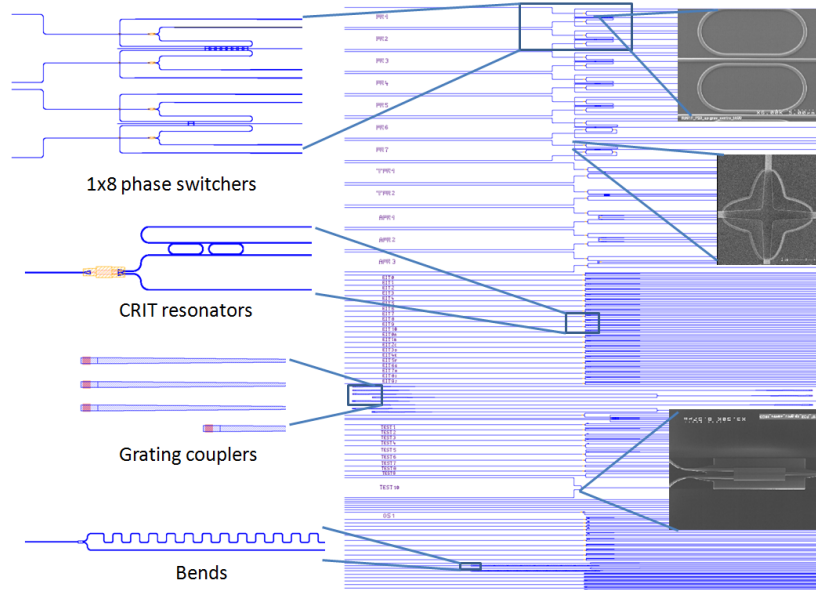**Figure 43:** *GDS II layout of one of the three designed wafers with some graphical zoom and the SEM images of the racetracks, crossings and MMI splitters (right side). Fabrication technology: LETI.*

routing devices we wanted to control separately the response of single resonators and their arrangement in SCISSOR structures characterized by the same parameters (R=3.25μm, $L = 10\mu m$, gap=160 nm, D=10.21μm).

Fig. 44 shows a comparison between the simulation of the theoretical model and the measured devices of the single resonator (black line) and the 2, 4, and 8 racetrack SCISSOR (red, blue, green lines respectively). There is of course a difference in the wavelength position of the mode.
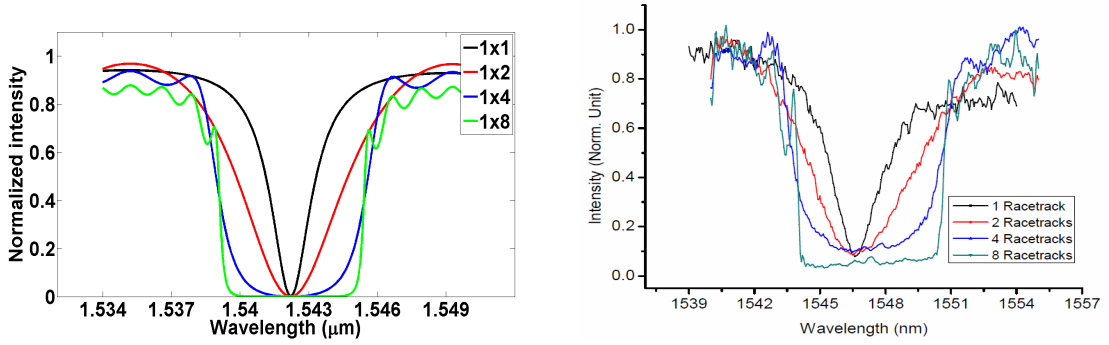

Figure 44: *Transmission spectrum of the $1 \times 1, 2, 4, 8$ racetrack SCISSOR (R=3.25μm, L = 10μm, gap=160 nm, D=10.21μm).*

The reason for this has already been explained in section 3.5, i.e. a slight discrepancy between the theoretical and the real dispersion law shifts the spectrum. There is also a slight difference in the pass-band widths, the theoretical curves predict a smaller bandwidth. This is due to the fact that in our modeling the coupling section considered was only the straight part of the resonator, while rigorously also the coupling on the curved part should have been taken into account. But taking into account also this aspect would have greatly complicated the analytical calculations, and since for our purposes an exact bandwidth evaluation was not so important, we considered this still a negligible error (however, we could also observe that by decreasing the gap of about 10 nm with respect to the nominal value, could be considered a satisfying correction to the otherwise underestimated coupling strength). The quality factor of the single racetrack shows to be about $Q = 600$. The asymmetries in the measured spectrum, especially on the single racetrack resonance, is caused by the MMI wavelength dependent imbalances which rendered difficult to evaluate the correct normalization at the reference port for every wavelength.

Figures 45 show the measurements of a set of waveguide coupled double racetrack add-drop filters, we shortly labeled 'CRIT resonators' in fig. 43, because they were expressively designed to check the induced transparency effect and to study the shift between the resonator and Bragg band (see discussion in section 4.3).
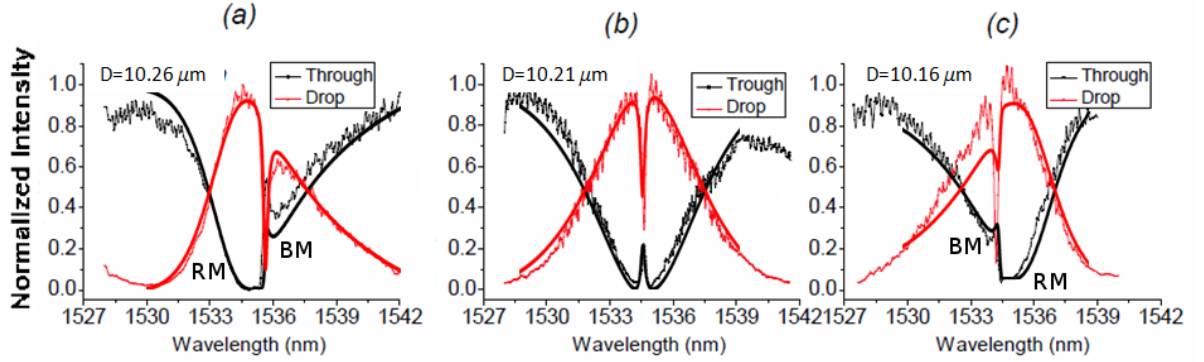

Figure 45: *CRIT effects and resonator and Brag band shifting.*

The parameters of the two resonators were the same as those of fig. 44 (red line), but with one of them having an optical path slightly detuned on the coupling section of about 5nm to induce a shift of the resonance peaks, and with different inter-resonator distances of $D = 10.26\mu m$, $D = 10.21\mu m$ and $D = 10.16\mu m$, which lead to the resonance to Bragg shift in the spectrum as shown in fig. 45 (a), (b), and (c) respectively. In order to test further our simulation code each figure shows the superimposed theoretical solid curves (red: Drop, black: Through). Fig. 45 (b) shows the case where the inter-resonator distance D is tuned to the coherence condition where the CRIT effect occurs, i.e. when the round-trip phase between the two resonators is a multiple of 2π.

In this situation both the drop and the transmission modes are symmetric but a high quality factor CRIT dip appears. However, for values of $D \neq \pi R$ (see eq. 4.28) the resonator and Brag modes (RM and BM in fig. 45) no longer overlap. For larger (shorter) values the Bragg band is red (blue) shifted as shown in fig. 45 (a) (fig. 45 (c)), while the resonator band maintains its symmetry. The overlap with the solid theoretical curves obtained from the simulations is good but showed also the high sensitivity to fabrication errors of this structure. In fact, only the simulation for the case of coherence

condition of fig. 45 (b) resulted from the nominal parameters, while fig. 45 (a) and fig. 45 (c) showed a best fit by introducing a different racetrack radius of one of the resonators and a different distance D (about $\triangle R = +3nm$ and $\triangle D = +5nm$ for both fig. 45 (a) and (c)). This little discrepancy was expected since ΔR and ΔD have the order of magnitude of the fabrication errors. It became clear that the spectral analysis of CRIT effects could in principle be used also as a way to measure statistical disorders.

But the wafers designed contained also some photonic structures which wanted to test other types of physical effects. For example a couple of resonators were arranged in such a way to test the Venier effect [79]. The Venier effect suppresses one of the modes of the resonant system increasing twice the FSR. This can be attained in a configuration like that shown in fig. 46 (a) by imposing the optical path in one of the resonators to be twice that of the other (i.e. the smaller racetrack suppresses half of the resonances of the larger one and only those they have in common remain).
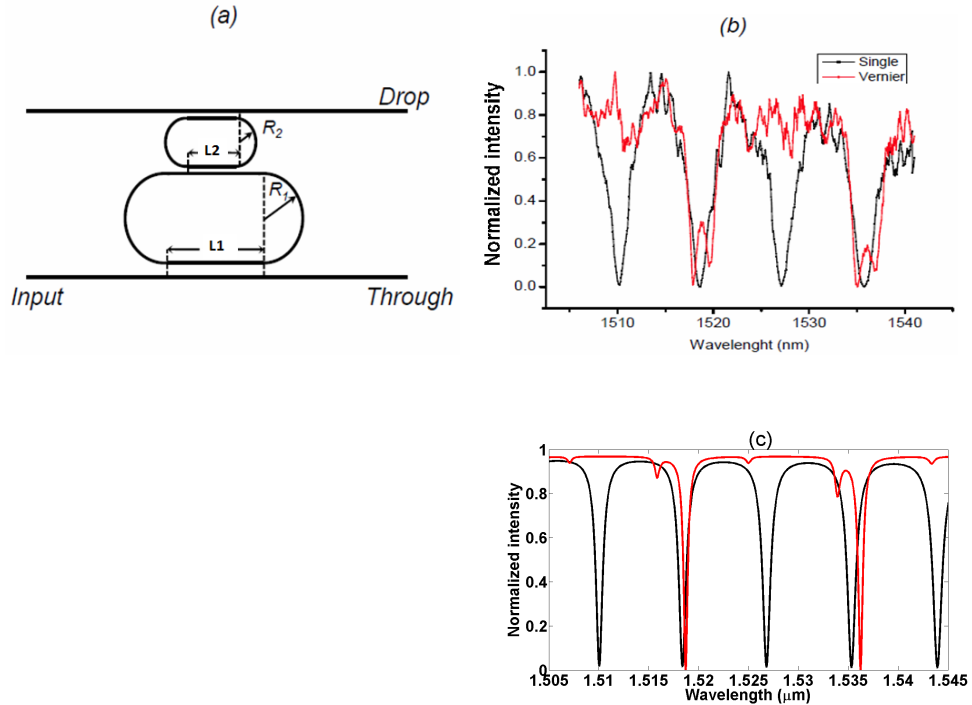

Figure 46: *The Venier effect. (a): The device structure; (b) the spectral response of the larger resonator and the Venier structure; (c): the simulated spectrum.*

79

This can be done, for example, by fabricating the two resonators with two different radius ($R_1 = 7.25\mu m$, $R_1 = 3.25\mu m$) and coupling sections lengths ($L_1 = 10\mu m$, $L_2 = 5.785\mu m$). The obtained spectral response is shown in fig. 46 (b). It confirms the predicted behavior: the black line represents the single (larger) resonator response, while in the red spectrum one of the modes has been clearly suppressed approximately doubling the FSR from 8 nm to 17 nm. The splitting of the modes are due to the strong coupling of the two resonators (gap spacing of 180 nm). A difference in the splitting can be observed between the theoretical curves and the measured ones. But this is only because the dips splitting and relative extinction depths are very sensitive to wavelength and are difficult to match exactly numerically (on other parts of the spectrum also the numerical simulation showed alternating dip intensities). This however does not alter the main result we were looking for, our algorithm predicted the observed FSR doubling.

Another interesting (serendipitously discovered) effect that we could observe was that of how a resonant structure, despite being very small and in over-coupling regime, can nevertheless manifest high quality factor modes. Usually one thinks that strong coupling leads to low quality factors, here we report of the opposite effect whereby strong coupling can lead also to high quality factors. We remind that the cross-coupling coefficient increases with increasing wavelength (the evanescent tail tends to spread, therefore the coupling length decreases and the cross-coupling increases because of eq. 2.46). This implies a decrease of the quality factor for increasing wavelength, as the wavelength scan measurement of the spectrum of a single resonator reveals.

Top of fig. 47 shows a wavelength scan from $1.5\mu m$ to $1.6\mu m$ of a racetrack resonator ($R = 3.25\mu m$, $L = 7.5\mu m$, wgw=$0.5\mu m$, gap=$0.18\mu m$). The steadily increasing FWHM of the modes visible in the Drop or Through signal is evident, which means that the quality factor is decreasing. However, from eq. 2.53 we know also that the coupling coefficients are periodic functions in L, i.e. the coupling strength is periodic with the coupling section length. From this follows that, once the coupling section reaches the coupling length, i.e. the maximum of power is coupled to the other waveguide, another
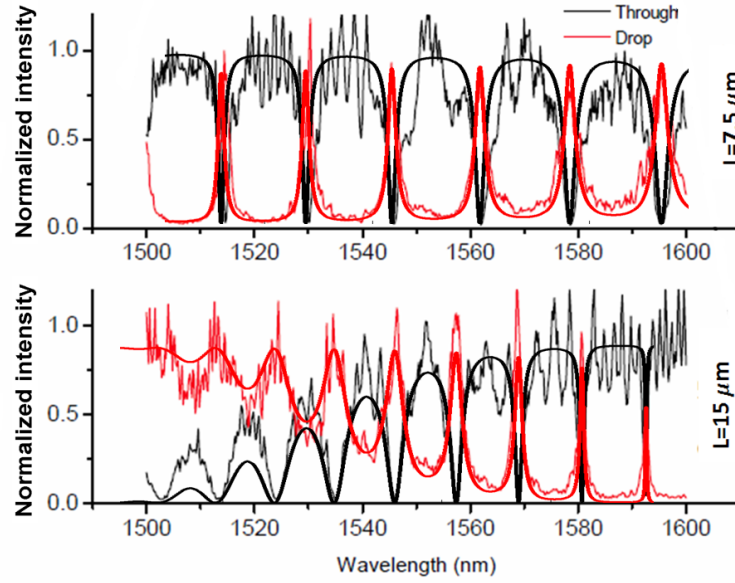
Figure 47: *Spectra of a racetrack resonators showing over-coupling effects (simulation: continuous lines). Top: with $L = 7.5\mu m$ coupling section. Bottom: with $L = 15\mu m$ coupling section.*

increase would lead not to more but to less power coupling, and consequently the quality factor begins to decrease again. Or, to put it in other words, the light is first coupled into the resonator straight coupling section, but before it can circulate towards the bent waveguide, part of its power couples back to the bus waveguide. This can be seen in the spectrum of the bottom of fig. 47 where a resonator with twice the coupling section, a smaller gap spacing and waveguide ($L = 15\mu m$, wgw=0.45μm, gap=0.16μm) was employed to obtain a still strong coupling regime. The continuous lines represent the result of the simulations. It fits well the data, however we had to notice that this is only the case if the (wavelength dependent) coupling length is decreased by 15-20% compared to the theoretically predicted one. The real cause of this discrepancy is not entirely clear. It might be due to the fact that the real device had different dimensions from those declared (exposer dose error might well induce $\pm$ 10 nm waveguide or gap spacing widths deviations which can influence the coupling length), the mode solver tendency to slightly overestimate coupling lengths might increase for smaller gaps, as in the present case, or both effects combined. Anyhow, despite these limitations, the qualitative behavior of the over-coupling effect is clear.

The devices and its measures proposed in this section were only some examples used as test and calibrating tools. The above given examples showed that there is a satisfying correlation between the theoretical model, its numerical implementation and the real devices behavior. The real aim of the three wafers designed and fabricated however was that to produce some photonic circuits demonstrating optical routing and switching functions with light. This is what will be described in the following sections.

6 Wavelength Routing Functions of SCISSOR and CROW

We will discuss three types of light routing/switching applications. The next section will discuss theoretically several phase switching photonic structures and proof its feasibility by presenting a device which has been fabricated and tested for this purpose. Later, a possible application where phase switching and narrow band channel routing are combined together will be analyzed also. Whereas in this section a couple of devices designed to obtain CWDM, i.e. where larger spectral bands instead of narrow band channels are routed, will be presented.

6.1 SCISSOR routing for coarse WDM applications: the one-directional band router

A way to separate light signals from a single multispectral source into wide spectral bands, i.e. operating CWDM, can be obtained by resorting to the SCISSOR low quality factor flat-box spectral response evident in fig. 36. Fig. 48 shows a simple example of how band-routing can be achieved. A single input waveguide is side coupled to four 1x8 SCISSOR devices each tuned on a different band leading to five outputs, i.e. it can be considered a 1×5 band router. The mode separation between the different SCISSOR can be obtained by differentiating their optical path, for example by changing slightly the radius or the length of the coupling section of the racetracks. The crosstalk between the bands must be evaluated by choosing carefully the gap separation between the input bus waveguide and the resonators. In our example we used the same technology described in the previous sections, the gap separation was 280 nm and, while the racetrack radius was maintained equal in all the resonators ($R = 3.25 \mu m$), to obtain an equally spaced band separation for all four SCISSOR devices a coupling section of $L = 10 \mu m$, $L = 10.085 \mu m$, $L = 10.17 \mu m$, and $L = 10.255 \mu m$ was chosen respectively. In
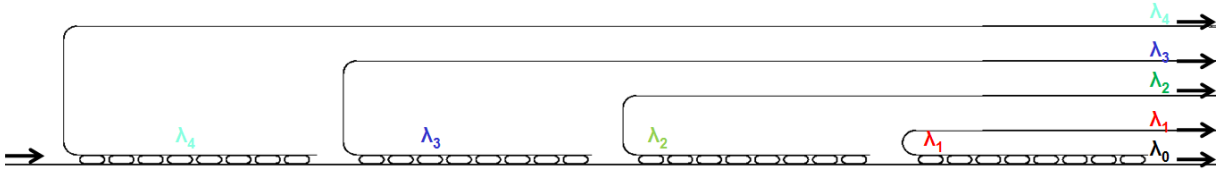
Figure 48: *The 1×5 SCISSOR-band router. The incoming light on the left is routed to five possible outputs according to its wavelength.*

this way the input light could be coupled according to its wavelength into one or the other SCISSOR which were designed to resonate at four different bands with central wavelengths λ_{1-4} and each with a separate output. This might be considered the most immediate and intuitive way to obtain band routing functions one can think of but, to the best of our knowledge, it has never been conceived and realized in a real device.

Knowing that fabrication errors, especially due to effective index variations induced by waveguide width fluctuations (here of nominal $0.45\mu m$), in order to be sure that the whole spectrum would have been overlapped by all the mode resonances, i.e. no wavelength would have been kept out by the routing structure and all the FSR would have been covered by the four modes, the crosstalk between the bands was maintained high on purpose.

The top of fig. 49 shows the spectral response obtained by TMM simulation of the 1×5 router, on the left in normalized intensity, and on the right in logarithmic scale (dB), where the simulation considered a gap of 250nm. The experimental data are shown in the two graphs of the lower part of fig. 49 and match satisfyingly the theoretical expected response with this gap. The discrepancy between the real and theoretical gap spacing is possibly explained with the fact that we selected a low dose die of the wafer which leads to smaller spacings between the waveguides than the nominal values. It appears that the spectral width of the bands becomes steadily narrower from the first to the last SCISSOR. This is caused by the fact that the finite roll off of every band leads to a band edge cutoff of the sidelobes of the mode which is injected towards the next resonating structure which in turn 'sees' at its input a decreased spectral width. The
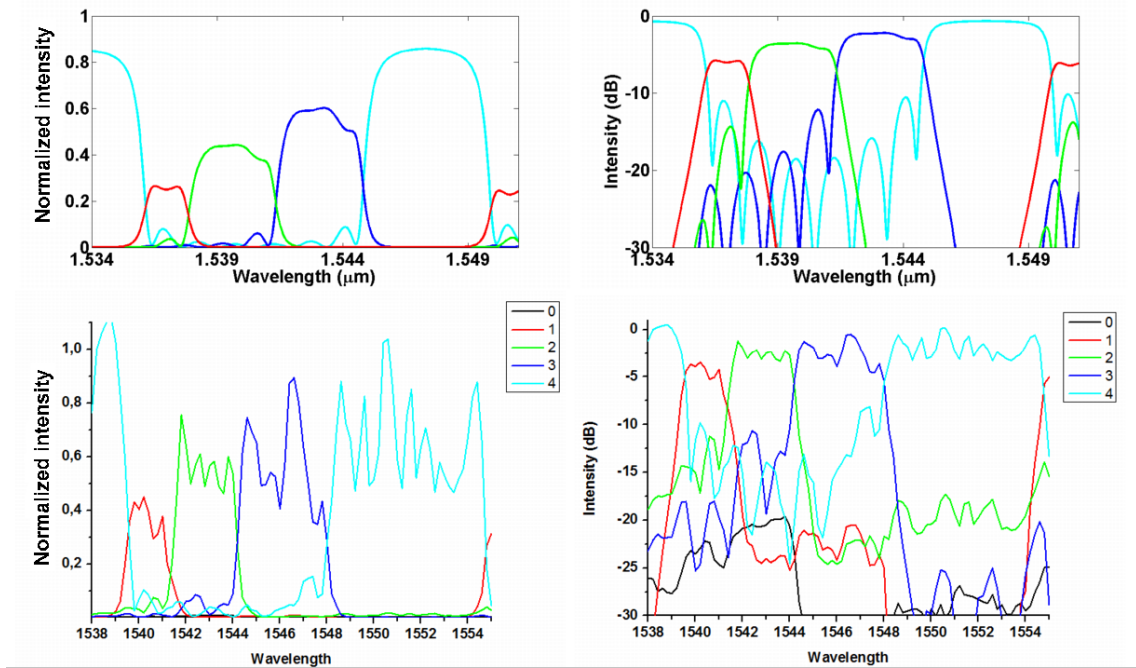
84

Figure 49: *Spectral response of the 1×5 SCISSOR-band router (top: simulation, bottom: measurement; left: normalized intensity, right: logarithmic scale (dB)).*

effect applies at every stage and the resulting spectral width of the last mode is smaller than the first one. This is of course undesirable, we didn't consider it initially in the design, and an optimized version of this device will be necessary. For instance, if one rearranges the modes spectral band width of every SCISSOR by tuning the optical length and/or apodizing the gaps it should be possible to optimize the distribution in order to obtain equally wide bands over the entire FSR. However, at least as a proof of concept, one-directional micro-optical band routing by SCISSOR devices has been shown to be possible.

6.2 SCISSOR routing for coarse WDM applications: the bi-directional band router

We were also wondering if, besides a one directional, also a bi-directional routing is possible. Another example of a possible application of the higher order flat-box filtering

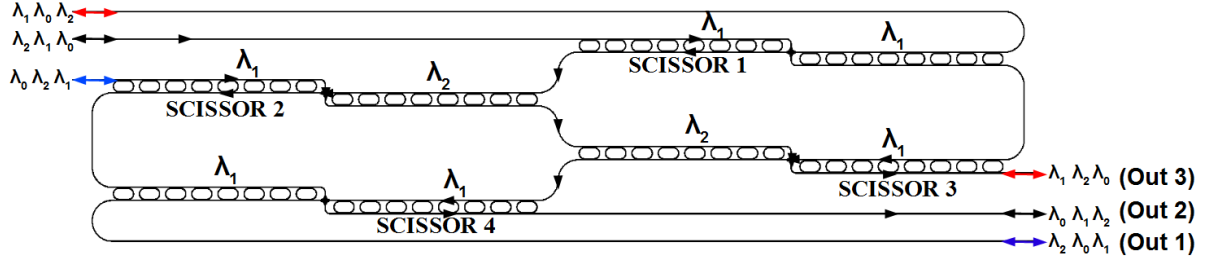behavior of SCISSOR structures for spectral band routing as a bi-directional router is shown in fig. 50.

Figure 50: *A* 3×3 *SCISSOR router*

Following the path of light in the structure one reconstructs the input-output signal table shown on the left and right side of the device (rows go into columns). For example, if a signal of wavelength λ_1 is injected into the lhs second port it will be filtered into the Drop port of SCISSOR 1, goes through the first crossing, will be filtered by SCISSOR 2, encounters the second crossing, and so on (follow the black arrows in fig. 50). For the inverse direction one proceeds in a similar path of add-drop filtering and light crossing outgoing at the rhs of the device.
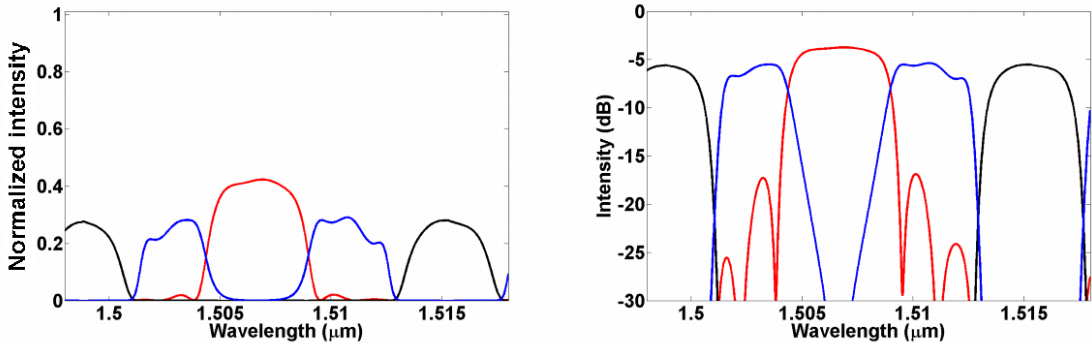
Figure 51: *The* 3×3 *SCISSOR router ideal spectral response at the output ports (blue:Out 1, black: Out 2, red: Out 3) for input signal as in fig. 50, in normalized intenisty (left) and logarithmic scale (right).*

Fig. 51 is the result of a simulation which shows the expected spectral response at the three rhs output ports (blue, black and red lines for output 1,2,3 respectively) for the signal injected in the second port on the lhs, as shown by the arrows in fig. 50, in

Figure 52: *The 3 × 3 SCISSOR router measured spectral response, lines and scales as in fig. 51.*

normalized intensity and logarithmic scale in the left and right graph respectively. For comparison fig. 52 shows the measured spectral response. The match with the expected ideal case of the simulation is not particularly exciting. The weak point of this geometry is that the signal undergoes several attenuations due to couplings and the presence of crossings, together with all the statistical fabrication errors which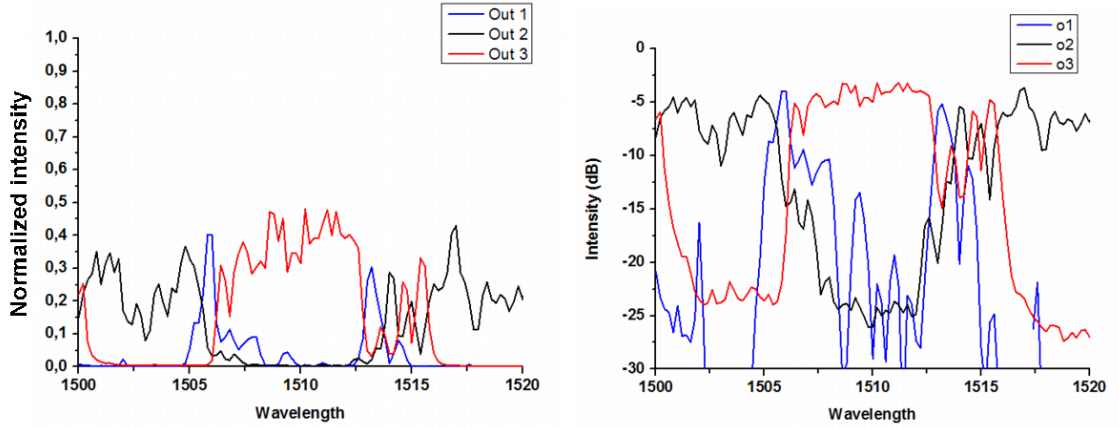 add up at every filtering stage. For example, the light path indicated by the black arrows in fig. 50 will have gone through four SCISSOR and four crossings before arriving at the rhs at the second output port. Moreover, it seems that the band width of the real SCISSOR tended to be larger than in the theoretical simulation. The reason for this is not entirely clear, but might be due to smaller gap spacings etched during the fabrication process possibly resulting from a lower exposer dose. These effects made it very difficult to obtain a satisfying experimental outcome. However, it is worth mentioning the fact that the signal in the two output ports 2 and 3 are separated from each others as expected (with exception on a small region around $\lambda = 1.515\mu m$), while the third channel is also clearly present in the spectral position as it should, tough only with weak intensity and on a smaller spectral range leading to a strong crosstalk with the other two outputs. This can be explained by the same phenomenon of the band-edge cut-off we mentioned for the 1×5 one-directional band router in the previous section, and is naturally stronger for the blue line (λ_0) compared with the other outputs, since it is the residual

87

spectral band left after all the other wavelengths have been filtered out by the SCISSOR structure.

Therefore, several optimizations are still needed to make this bi-directional routing device more efficient. A more careful analysis and design of the spectral width of each SCISSOR, together with its coupling section and waveguide to resonator gap must be chosen differently (i.e. apodization is necessary). However, a first prof of concept has been shown. The spectral bands are routed towards different outputs according to the wavelength as expected. The question at this point is no longer if such kind of devices works, but how far can its performance be enhanced by these optimizations and by future lithographic technologies.

7 Theory of Phase Switching Functions of SCISSOR and CROW

So far a couple of examples of possible photonic devices for WDM applications have been shown. They entirely relied on the principle that the wavelength of an input signal decides the routing direction. However, it will be shown that similar routing functions can be obtained by phase modulation between two or more incoming signals. Some introductory example using light switching by phase modulation or splitting and combining was described in section 2.3, but it was limited to a single wavelength (through eq. 2.54 and eq. 2.80). The single channel photonic switching between co-directionally coupled waveguides is extremely fast (only the traveling time of light through the coupling section structure). On the other side, for practical reasons it might be more useful to apply the same phase switching principle on larger resonant systems. For these, despite having a longer reaction time, since it depends on the power build up of light in the structure, however allow for switching and routing functions of a larger set of channels or even on spectral bands.

7.1 Dual bus resonator phase switching

Let us get back to the elementary example of the single resonator, but this time considering two interfering signals in the Input and Add port, as in fig. 53. We briefly recapitulate what we have seen in sections 4, but by means of the result of section 2.3.

For the sake of simplicity we consider only the case of symmetric coupling, i.e. considering the bus-waveguides spacings and its coupling section lengths to be the same everywhere. We apply the transfer matrix approach. The first step is to relate the amplitudes $(A_1^1, A_2^1) \rightarrow (A_1^2, A_2^2)$. We already know the elementary transfer matrix $\mathbf{M}$ between the coupling section and the resonator from 4.7, but note that this could be obtained also from 2.50 and 2.51, even if through a more elaborate way.
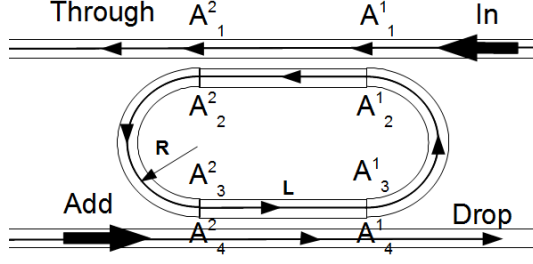
Figure 53: *The single resonator ds-coupler switch.*

Again, as done in section 4 the coupling matrix $\mathbf{K}$ relating $(A^1{}_1, A^2{}_1) \rightarrow (A^1{}_2, A^2{}_2)$ is given by eq. 4.11, where, for the straight sections, the lossless case $(|\kappa_1|^2 + |t_1|^2 = 1)$ will be considered. And also the (forward and backwards) internal propagation matrix $\mathbf{P}$ for the racetrack was given by 4.12.

Now we introduce some modifications and simplifications which are more appropriate for the present problem. We can express the passage $(A^1{}_1, A^2{}_1) \rightarrow (A^2{}_3, A^1{}_3)$ described by $\mathbf{K}$ and $\mathbf{P}$ in a more compact form defining the first 'transfer matrix' $\mathbf{T}^{\mathbf{PK}}$ as their product:

$$\begin{pmatrix} A^2{}_3 \\ A^1{}_3 \end{pmatrix} = \mathbf{T}^{\mathbf{PK}} \begin{pmatrix} A^1{}_1 \\ A^2{}_1 \end{pmatrix} = \mathbf{PK} \begin{pmatrix} A^1{}_1 \\ A^2{}_1 \end{pmatrix} . \tag{7.1}$$

Thus, the amplitudes at the ports of fig. 53 can be related as

$$\begin{pmatrix} A_{Ad} \\ A_D \end{pmatrix} = \mathbf{T^1} \begin{pmatrix} A_{In} \\ A_{Th} \end{pmatrix} = \mathbf{K}\,\mathbf{T}^{\mathbf{PK}} \begin{pmatrix} A_{In} \\ A_{Th} \end{pmatrix} , \tag{7.2}$$

and by rearranging the elements of transfer matrix $\mathbf{T^1}$ into the scattering matrix $\mathbf{S^1}$ accordingly, one obtains

$$\begin{pmatrix} A_{Th} \\ A_D \end{pmatrix} = \mathbf{S^1} \begin{pmatrix} A_{In} \\ A_{Ad} \end{pmatrix} . \tag{7.3}$$

With this we can simulate the device of fig. 53 by choosing the following photonic parameters: bend curvature radius of $3.25\mu m$, gap spacing of $0.2\mu m$, waveguides width

of $0.45\mu m$, waveguide core height of $0.22\mu m$, SiO$_2$ cladding of $0.75\mu m$, and $-0.03dB/90°$ bend loss in TE polarization.

Instead of displaying the spectral response of a resonant structure in terms of wavelength it is possible to put it in qualitatively more general terms. One can consider the system non dispersive on the FSR that separate two modes, and express the spectral scan in the graphs in terms of round trip de-phasing instead of the absolute value of the wavelengths. In fact, according to 3.14, in the case of dispersionless systems the two modes at λ_1 and λ_2 are determined solely by the optical path of the resonator, $p_{opt} = (2\pi R + 2L)\, n_{eff}$ (with n_{eff} the effective index at resonance wavelength of the waveguides), and the mode azimutal number m, as:

$$\lambda_1 = \frac{p_{opt}}{m}, \qquad \lambda_2 = \frac{p_{opt}}{m+1}. \tag{7.4}$$

This means that the difference is

$$\lambda_2 - \lambda_1 = -\frac{p_{opt}}{m(m+1)} = -\frac{\lambda_1}{m+1} = -\frac{\lambda_1 \lambda_2}{p_{opt}}. \tag{7.5}$$

Then the parameter γ representing the round-trip de-phasing of the resonator can be defined as an 'angular deviation' from resonance at some wavelength λ as:

$$\lambda = \lambda_1 + \frac{\gamma}{2\pi}(\lambda_2 - \lambda_1) = \lambda_1 - \frac{\gamma}{2\pi}\frac{\lambda_1 \lambda_2}{p_{opt}}, \tag{7.6}$$

and from which

$$\gamma = 2\pi p_{opt}\frac{\lambda_1 - \lambda}{\lambda_1 \lambda_2} \approx 2\pi p_{opt}\frac{\Delta\lambda}{\lambda^2}.$$

With this convention we can analyze the standard single resonator mode spectrum (fig. 54 left) and see how it is transformed if we inject two normalized input signals, one in the In port and the other into the Add port setting in eq. 7.3 $A_{In} = e^{i\phi_1}$ and $A_{Ad} = e^{i\phi_2}$, with ϕ_1 and ϕ_2 the phases of the In and Add signals respectively. Then for a phase difference of $\Delta\phi = \phi_2 - \phi_1 = \frac{\pi}{2}$, we obtain a response like that of in fig. 54 right.

The shapes of the Drop and Through ports signals become asymmetric. This is the manifestation of the Fano resonance that arises from the interference between the
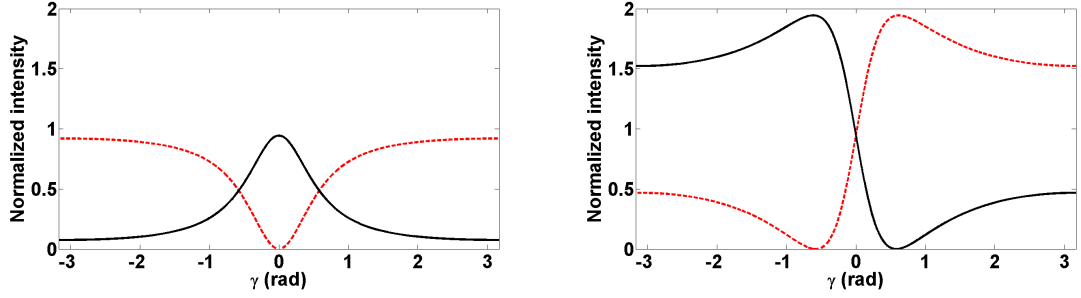
Figure 54: *The single resonator mode spectrum (left) and the dual-bus single resonator Fano resonance spectrum (right) for $\Delta\phi = \frac{\pi}{2}$ (Drop: black solid line, Through: red dashed line).*

resonant modes in the racetrack, where a narrow band superimposes on a flat spectral background [81, 82]. Fano resonances attracted renewed attention in several fields of physics [83]. Recent studies highlighted its applications also for optical micro-resonators [84, 85] and in ring enhanced Mach-Zhender interferometers [86, 87, 80]. The asymmetric line shapes of Fano resonances are due to interference phenomena that can be related to the interaction of a discrete resonator state and the waveguide continuum of propagation modes.

Devices where two phase modulated incoming signals are injected can be used for light switching functions. A high extinction ratio on-off switching for a couple of channels (or bands) can be obtained at the channel wavelength of the Through and Drop extrema. For instance, in our example of fig. 54 right, at around $\gamma = \pm 0.6$, for a de-phasing of $\Delta\phi = \frac{3}{2}\pi$, the Through and Drop ports states are exchanged one into another (not shown, graphically the black solid line would go into the red dashed line). This means that by phase modulation the signal output can be switched off in the Through port to the Drop port, or viceversa.

It is possible to extend this phase switching functions also to a parallel or serially coupled chain of resonators, i.e. like in CROW or SCISSOR, as shown in fig. 55.

Again, as explained in section 4, for the SCISSOR one introduces the external propagation matrix $\mathbf{Q}^j$ of eq. 4.17 connecting the j-th to j+1-th column resonator, where $D^{j\,j+1}$ is the inter-resonator distance separating the resonator's j-th to j+1-th
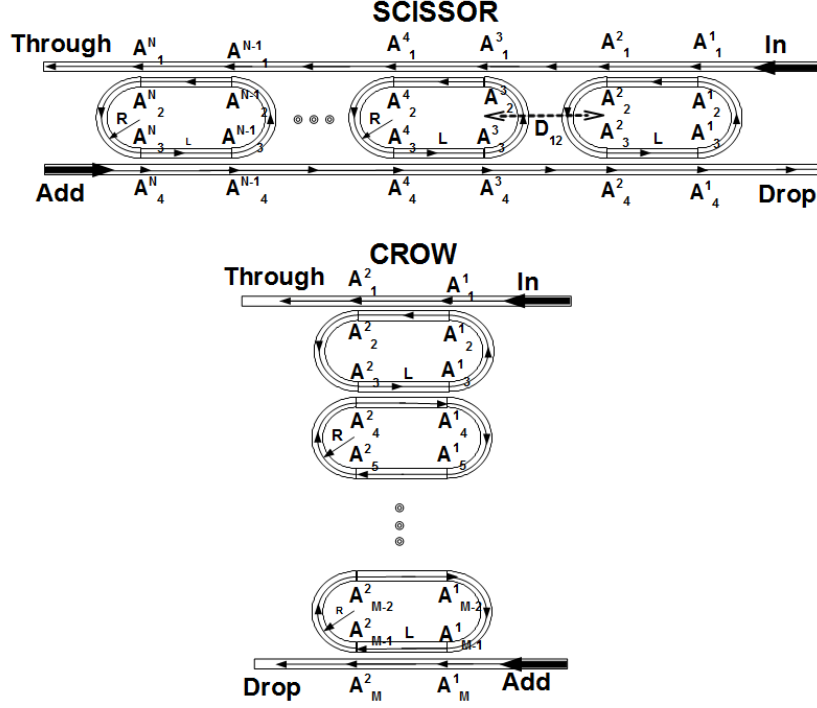
Figure 55: *The dual-bus SCISSOR and dual-bus (even) CROW resonant structure.*

straight arm as shown in the SCISSOR of fig. 55.

Then, eq. 7.3 can be generalized to the SCISSOR structure as a horizontal scattering matrix $\mathbf{S_h}$ as:

$$\begin{pmatrix} A_{Th} \\ A_D \end{pmatrix} = \mathbf{S_h} \begin{pmatrix} A_{In} \\ A_{Ad} \end{pmatrix} = \mathbf{S^N}\,\mathbf{Q}^{N-1}\mathbf{S^{N-1}}...\mathbf{Q^1}\mathbf{S^1} \begin{pmatrix} A_{In} \\ A_{Ad} \end{pmatrix}, \qquad (7.7)$$

and which is 4.19.

For the CROW we simply generalize eq. 7.2 to

$$\begin{pmatrix} A_{Ad} \\ A_D \end{pmatrix} = \mathbf{T^N}...\mathbf{T^2}\mathbf{T^1} \begin{pmatrix} A_{In} \\ A_{Th} \end{pmatrix}, \qquad (7.8)$$

with $\mathbf{T^k}$ (k=1,..,N) the transfer matrix for the k-th row resonator given by eq. 7.1, and which is equivalent to eq. 4.14. From this we obtain, again as in eq. 7.3, the vertical scattering matrix $\mathbf{S_v}$

$$\begin{pmatrix} A_{Th} \\ A_D \end{pmatrix} = \mathbf{S_v} \begin{pmatrix} A_{In} \\ A_{Ad} \end{pmatrix}.$$ (7.9)

Note that for an even number of resonators the CROW becomes co-directional, i.e. the In-Through and Add-Drop signals travel in the same direction. This might be useful for practical applications.
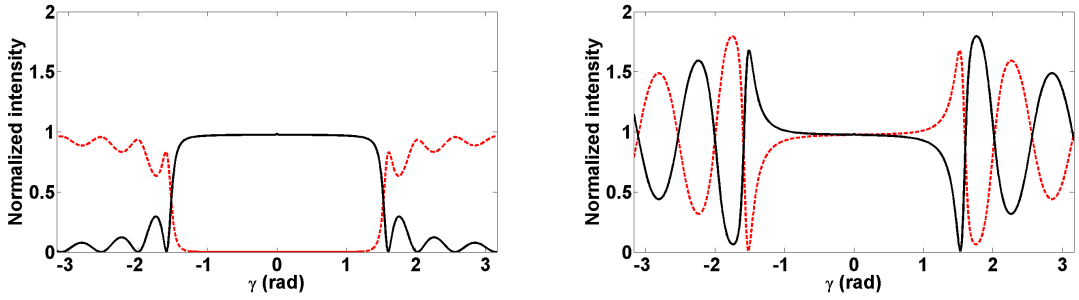

Figure 56: *The single (left) and dual-bus (right) eight resonator SCISSOR spectrum for $\Delta\phi = \frac{\pi}{2}$. (Drop: black solid line, Through: red dashed line)*

Fig. 56 shows the example for the SCISSOR spectrum made of a chain of eight resonators obtained from eq. 7.7 (the black solid line for the Drop port and the red dashed line for the Through port). The first graph (left of fig. 56) represents the spectrum where only one signal is injected: the higher order flat-box spectrum appears.

When a second signal with the same amplitude at the Add port is turned on, with a de-phasing of $\Delta\phi = \frac{\pi}{2}$, the spectral behavior of the second graph appears (right of fig. 56). This state depends strongly from the de-phasing value and it can be flipped to a specular behavior by exchanging the Drop and Through port signal's phase, as already noted for the case of the single resonator. This phase switching could be applied best at the frequency of maximal contrast between the Through and Drop (e.g. here at about $\gamma = \pm 1.5$, right of fig.56): by maintaining the same amplitudes on the inputs but for a de-phasing of $\Delta\phi = \frac{3}{2}\pi$ it is possible to switch the light from the Through to the Drop port, or viceversa. Compared to the single resonator case, possibly a couple of channels (or bands) more might be used for phase switching functions (in our example the lobes

at around $\gamma = \pm 1.75$), but with lower extinction rates. Therefore, under this respect, the SCISSOR geometry presents limited advantages over the single resonator case of fig. 54.
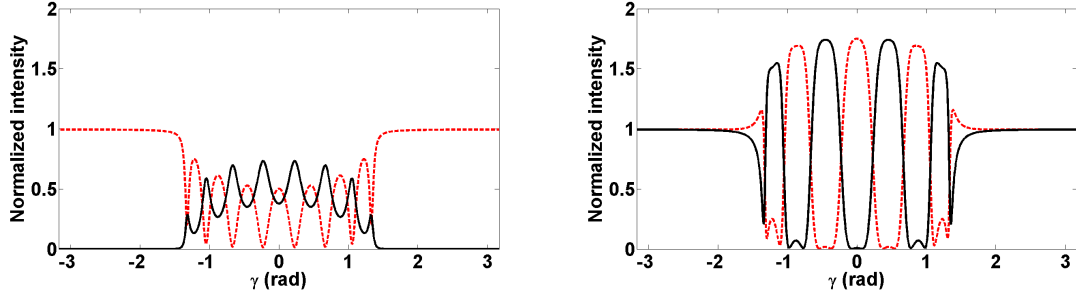

Figure 57: *The single (left) and dual-bus (right) eight resonator CROW spectrum for $\Delta\phi = \frac{\pi}{2}$. (Lines as in fig. 56)*

The case for the CROW structure, also made of a chain of eight resonators, and obtained from eq. 7.9, is shown in fig. 57. As in the previous case the left and right graphs represent the single- and double-bus spectra for the same de-phasing. Here we have a quite different situation: given N serially coupled resonators, the N Drop peaks of the first CROW spectrum (one input signal only, left fig. 57) is converted into a system of N-1 bands by turning on the second input signal with a $\Delta\phi = \frac{\pi}{2}$ de-phasing (right of fig. 57). Again, for a de-phasing of $\Delta\phi = \frac{3}{2}\pi$, one can flip the Through $\leftrightarrow$ Drop port outputs into each others by phase modulation.

Not all bands have the same extinction efficiency, only the central ones exhibit an almost ideal on-off state, but the CROW geometry has the advantage over the SCISSOR and single resonator structures that it exhibits several bands, proportional to the number of resonators and in principle limited only by practical considerations imposed by the fabrication tolerances. The width of each band depends from the photonic parameters and the number of resonators used to build the device (in our example these are of the order of 1nm width), but in principle several narrow width channels could be arranged in each of the bands and a sort of "photonic packet phase switching" can be achieved whereby several channels can be re-direct towards one or the other output port by phase modulation. Note that a device working on such principle
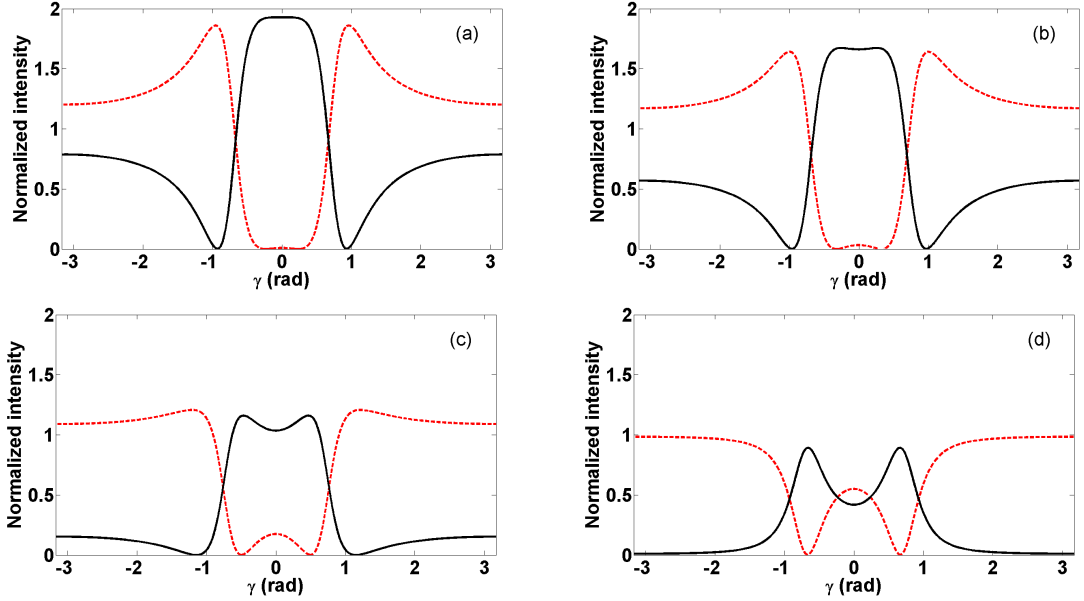
Figure 58: *The dual-bus two resonator CROW spectrum with $A_{In_1} = e^{i\pi/2}$, $I_{In_2} = (1, 0.75, 0.25, 0)$ ((a), (b), (c), (d) respectively). (Lines as in fig. 56.)*

can be useful also as a micro-optical interleaver, i.e. as a device that separates a set of channels/bands into two sets of signals towards the Drop and Through ports.

Another example of how a spectrum transforms from the two-bus to one-bus case is given in fig. 58 for two resonator CROW device with $\Delta\Phi = \frac{\pi}{2}$ and with different input imbalances ($I_{In_2} = (1, 0.75, 0.25, 0)$ for fig.58 (a), (b), (c), (d) respectively). The two resonator CROW is interesting since for the single band it takes a larger part of the spectrum compared to the previous eight resonator CROW of fig.57 and is therefore more useful for band routing applications. Fig. 59 represents the phase scan for each of the cases of fig. 58 where the wavelength is fixed at $\gamma = 0$. For example fig. 59 (a) represents the variation of the Drop and Through port signal intensity by changing the relative phase between the two balanced input (In and Add) ports at the fixed center resonant wavelength. Band switching is obtained by π de-phasing.

.
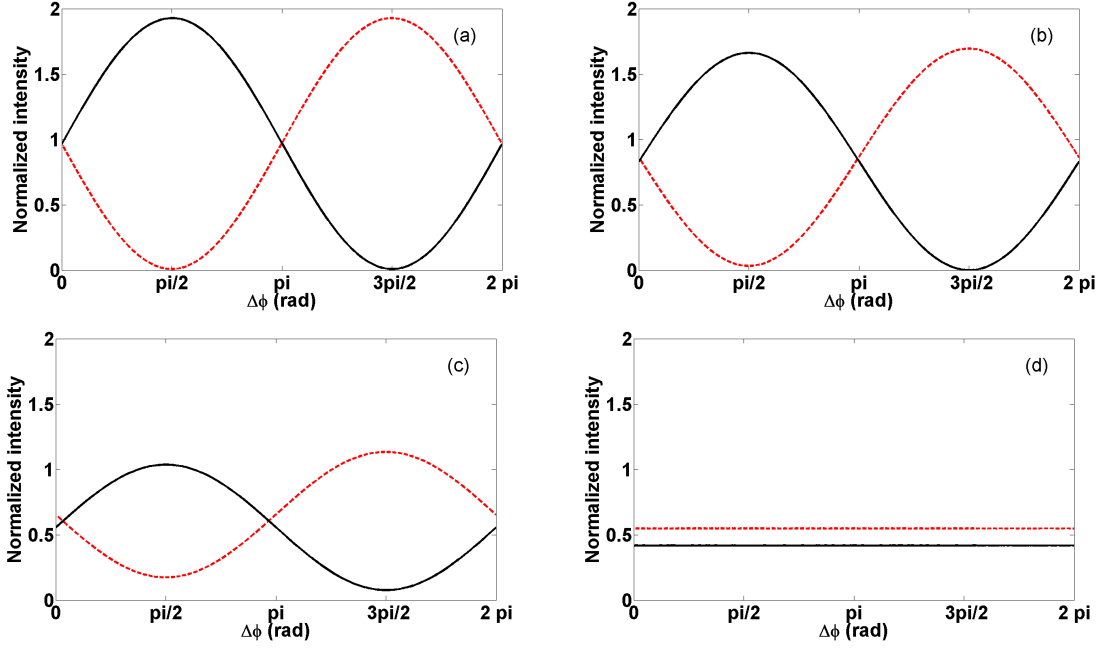
Figure 59: *The dual-bus two resonator CROW phase response at $\gamma = 0$, with $A_{In_1} = e^{i\Delta\Phi}$, $I_{In_2} = (1, 0.75, 0.25, 0)$ ((a), (b), (c), (d) respectively). (Lines as in fig. 56.)*

.

7.2   Three bus resonator phase switching

The preceding sections were originally inspired by the necessity to describe a structure like that of fig. 60. It shows a ds-coupling phase switching scheme based on a single pair of racetrack resonators but with three bus waveguides. It should work as follows. If the amplitudes of the input signals, A_{In_1} and A_{In_2}, are tuned on a resonant mode wavelength and have the same amplitude then, according to their relative phase, they will interfere constructively or destructively in the Drop port. In the former case the power is expected to couple into the Drop port, while in the latter case the light will not couple and travel towards the Through ports.

Now, we would like to write a system of equations and conditions that relate the known amplitude $A^1_1 = A_{In_1}$, $A^2_4 = A_{Ad}$, $A^1_7 = A_{In_2}$ to the unknown $A^2_1 = A_{Th_1}$, $A^1_4 = A_D$ and $A^2_7 = A_{Th_2}$. To characterize quantitatively the response of the device also for

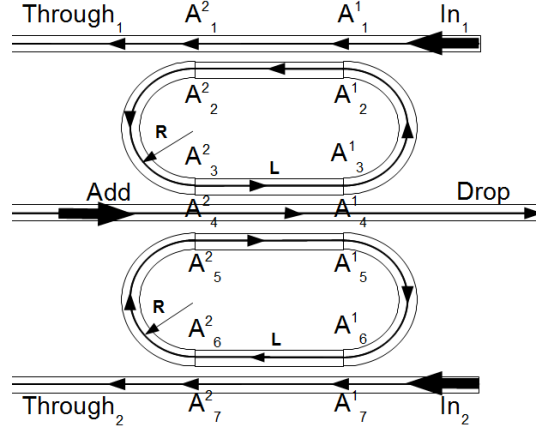**Figure 60:** *The resonator pair ds-coupler switch.*

different amplitudes and phases we obtained the general transfer matrix $\mathbf{T}$ which describes the behavior of the device of fig. 60:

$$
\begin{pmatrix} A_{Th_1} \\ A_D \\ A_{Th_2} \end{pmatrix} = \begin{pmatrix} T_{11} & T_{21} & T_{31} \\ T_{21} & T_{22} & T_{21} \\ T_{31} & T_{21} & T_{11} \end{pmatrix} \begin{pmatrix} A_{In_1} \\ A_{Ad} \\ A_{In_2} \end{pmatrix} = \mathbf{T} \begin{pmatrix} A_{In_1} \\ A_{Ad} \\ A_{In_2} \end{pmatrix}, \tag{7.10}
$$

where the explicit calculation of the matrix elements is given in the appendix. The symmetry of $\mathbf{T}$ makes it clear that we assumed a symmetric device: the paths $(In_1 \rightarrow Through_1,\ In_1 \rightarrow Drop,\ In_1 \rightarrow Through_2)$, are considered equivalent to paths $(In_2 \rightarrow Through_2,\ In_2 \rightarrow Drop,\ In_2 \rightarrow Through_1)$ respectively.

Figures 61 show the obtained spectral response of the single Input-bus resonator pair ds-coupler, that is when only one input signal is injected ($A_{In_1} = 1$, $A_{Ad} = 0$, $A_{In_2} = 0$), with different coupling section lengths of $L = 10\mu m$ and $L = 3\mu m$ (left and right of fig.61 respectively). In the former case the power which does not exit the Drop channel (black solid line) and goes towards the Through$_2$ port (blue dotted-dashed line) represents the cross-talk of the device which shows to be very strong at resonance, the power is almost equally distributed among the Drop and Through$_2$ port with a very low Q. In the latter case, the cross-talk is much smaller and for this reason it might be considered preferable, especially where high quality factors are needed, even if the price
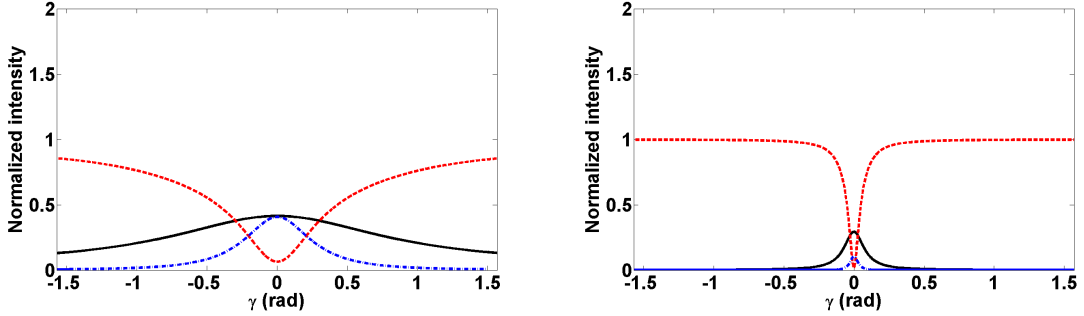
Figure 61: *Spectral response of the device in fig. 60, with $A_{In_1} = 1$, $A_{Ad} = 0$, $A_{In_2} = 0$, $L = 10\mu m$ (left) and $L = 3\mu m$ (right) (Drop port: black solid line, Through$_1$ port: red dashed line, Through$_2$ port: blue dotted-dashed line.)*

to pay is a weaker Drop signal. However, as we will see, if manipulated properly, in a dual-bus device strong coupling itself can be used to suppress cross-talk without loosing too much Drop intensity.

Figures 62 show the case of a device (from now on always $L = 10\mu m$ coupling section) where both input signals have the same amplitude but a different phase difference of $\Delta\phi = (0, \frac{\pi}{4}, \frac{3}{4}\pi, \pi)$ (fig. 62(a), (b), (c), (d) respectively). As expected, when the two input signals are in phase, and the wavelength is resonant with the two racetracks, then most of the power is transferred to the Drop port.

The Through ports will not exhibit complete extinction due to cross-talk effects (fig. 62(a)). Similarly, when they are in anti-phase (fig. 62(d)) in the Drop port the destructive interference is complete and no signal is observed, while most of the power goes straight in the Through ports (the Through minima at resonance are due to the resonator round trip losses). But, except for the perfect phase or anti-phase cases, the Through ports resonance shapes become asymmetric and manifest Fano resonance (fig. 62(b) and 62(c)). The Fano asymmetry is stronger for $\Delta\phi = \frac{3}{4}\pi$ of fig. 62(c) than for $\Delta\phi = \frac{\pi}{4}$ of fig. 62(b) where it appears still only as a 'bump' in the resonance shape of fig. 62(a). The point of interest however is that the two Through shift away from each others. With no de-phasing the Through ports minima coincide with the Drop maximum at λ_0, otherwise they quickly split apart ($\lambda_F = \lambda_0 \pm 0.8nm$ in our case,
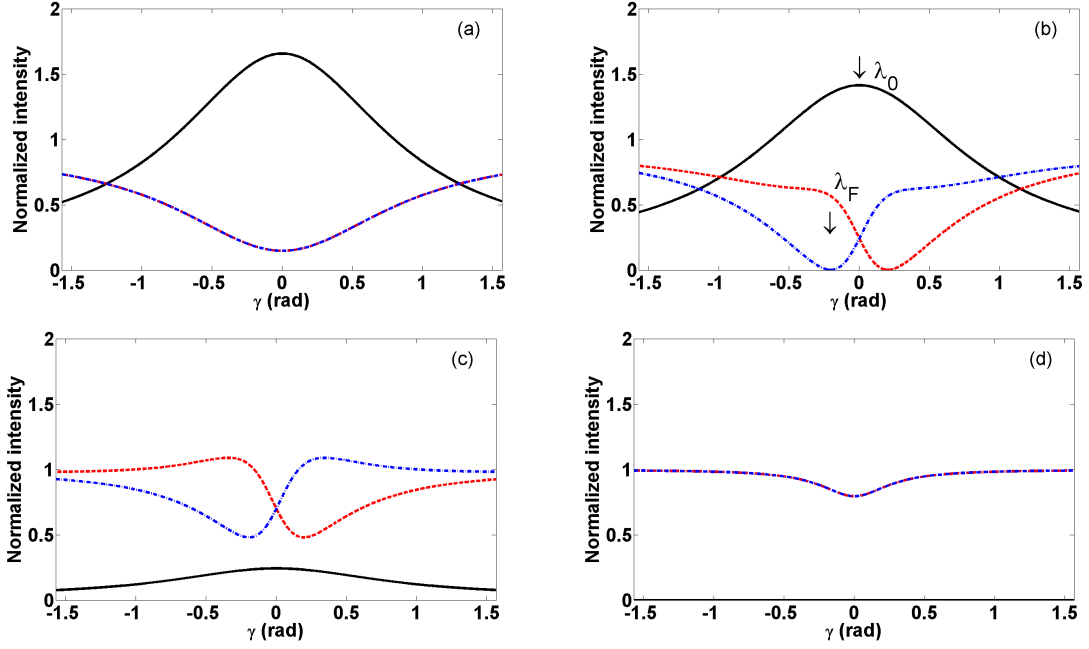
99

Figure 62: *Spectral response of the device in fig. 60, with $A_{In_1} = (1, e^{i\frac{\pi}{4}}, e^{i\frac{3}{4}\pi}, e^{i\pi})$ ((a), (b), (c), (d) respectively), $A_{Ad} = 0$, $A_{In_2} = 1$. (Lines as in fig. 61.)*

already for $\Delta\phi = \frac{\pi}{10}$). Moreover, the Through ports resonance depth depends from the de-phasing and reaches almost complete extinction at $\Delta\phi = \frac{\pi}{4}$ for our case (fig. 62(b)). Similarly to what we have seen for the ds-coupler switch in section 2.4 this is potentially useful to build phase switching devices with good on-off extinctions, even if they exhibit strong cross-talk in the single-bus arrangement.

To highlight this we repeated the calculations, this time fixing the excitation input signals at the resonant or at the 'Fano wavelength' (λ_0 or λ_F respectively), and varying $\Delta\phi$. At the same time we were also interested in seeing how the system behaves for different input intensities, for instance maintaining one of the input ports with fixed intensity while varying the intensity of the other.

The result is shown in fig. 63 for wavelength λ_0 and in fig. 64 for wavelength λ_F, for four different inputs ($I_{In_2} = \delta \times I_{In_1}$ with $\delta = (1, 0.75, 0.25, 0)$). The following can be observed. First of all by comparing fig. 63 (a) with fig. 64 (a) one can see that, for perfect input balance, the Drop port signal turns on and off completely, but the

Figure 63: *Phase response of the device in fig. 60 at λ_0, with $A_{In_1} = e^{i\Delta\Phi}$, $A_{Ad} = 0$, $I_{In_2} = (1, 0.75, 0.25, 0)$ ((a), (b), (c), (d) respectively). (Lines as in fig. 61.)*

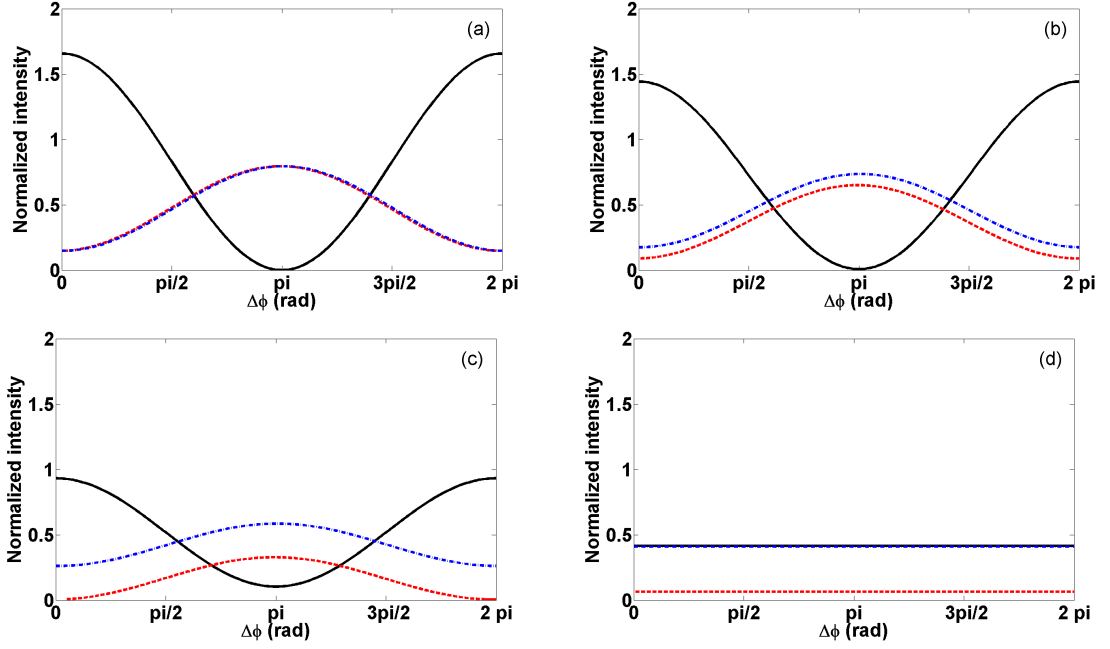**Figure 64:** *Phase response of the device in fig. 60 at λ_F, with $A_{In_1} = e^{i\Delta\Phi}$, $A_{Ad} = 0$, $I_{In_2} = (1, 0.75, 0.25, 0)$ ((a), (b), (c), (d) respectively). (Lines as in fig. 61.)*
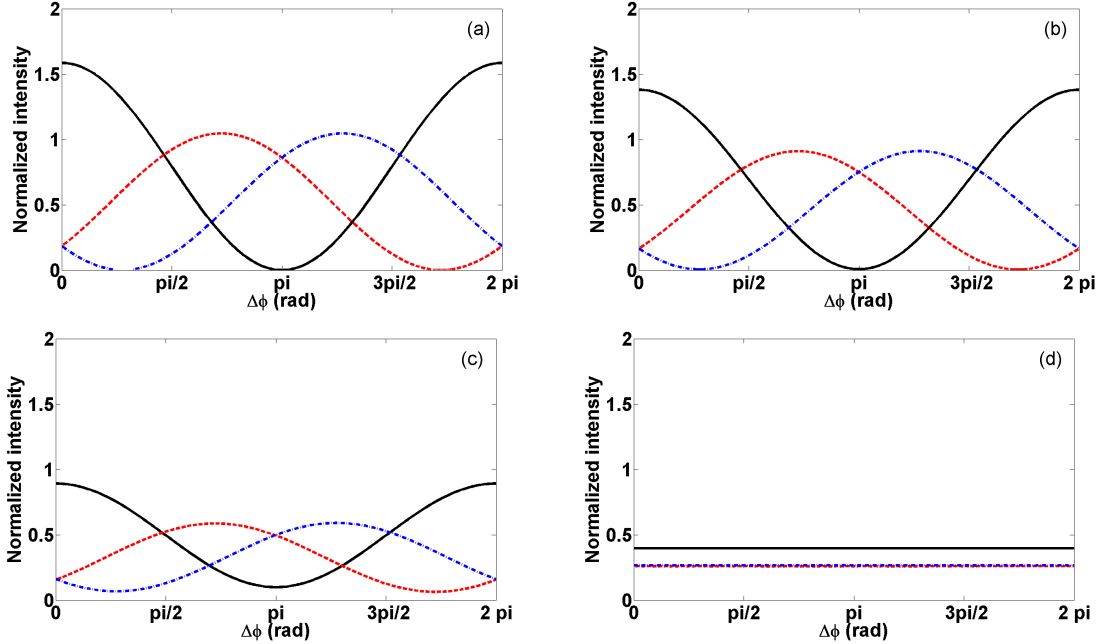
Through ports light intensity is never extinguished, whatever the de-phasing. While in fig. 64 (a) one of the Through signals is almost perfectly off for some de-phasing value.

In this sense phase switching at λ_F is more efficient. The case of fig. 64 is also interesting because three phase switching states are possible: at $\Delta\phi = \frac{\pi}{4}$ the Drop and Through$_1$ are on and Through$_2$ is off, at $\Delta\phi = \pi$ the Drop is off and both Through are on, and at $\Delta\phi = \frac{7}{4}\pi$ the Drop and Through$_2$ are on and Through$_1$ is off. Secondly, from figs. 63 and 64 it becomes clear how a ds-resonator phase switch device must be robust against the bus signal imbalance. An imbalance of about $\delta = 0.5$ at $\Delta\phi = \pi$ is needed to prevent the Drop ports extinction in both cases. The case tuned on λ_F shows also that the Through port signals are more intense than in the case for λ_0 which might be useful for practical purposes.

Repeating these simulations for the same device but with with weak couplings, e.g. with an $L = 3\mu m$ coupling section, would lead to similar theoretical conclusions tough with weaker outputs (not shown here, but similar to fig. 64(c)), and with 'Fano splitting' of the Through anti-resonances almost an order of magnitude smaller which would make it more difficult to exploit it from the practical point of view. Therefore, if high quality factors are not essential (for instance for band- instead of channel-routing systems), to attain efficient dual-bus phase switching strong coupling with cross-talk suppression can be used.

If one desires to expand this analysis also to a SCISSOR, we have only to relate the Through and Add ports of one pair of resonators to the next pair separated by a (bend) center to center distance D, as shown in fig. 65. To do that we must first transform properly $\mathbf{T}$ of eq. 7.10 into the 'scattering matrix' $\mathbf{S}$ such that

$$\begin{pmatrix} A_{Th_1} \\ A_{Ad} \\ A_{Th_2} \end{pmatrix} = \mathbf{S} \begin{pmatrix} A_{In_1} \\ A_D \\ A_{In_2} \end{pmatrix} . \tag{7.11}$$
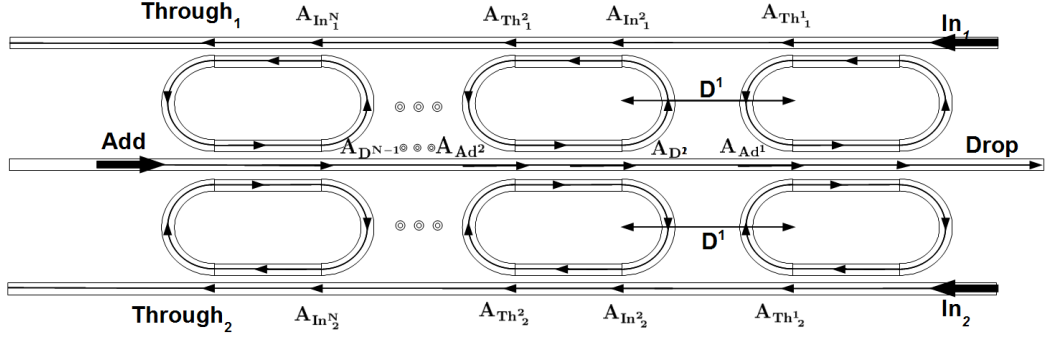
Figure 65: *The 2xN SCISSOR phase switch.*

After simple standard algebraic manipulation one sees that:

$$\mathbf{S} = \frac{1}{T_{22}} \begin{pmatrix} T_{11}T_{22} - T_{12}T_{21} & T_{12} & T_{31}T_{22} - T_{12}T_{21} \\ -T_{21} & 1 & -T_{21} \\ T_{31}T_{22} - T_{12}T_{21} & T_{12} & T_{11}T_{22} - T_{12}T_{21} \end{pmatrix}, \tag{7.12}$$

where the lower indexes indicate the row $\times$ column element of $\mathbf{T}$.

Then, by introducing an external propagation matrix $\mathbf{Q^k}$ which connects the Through and Add ports of the k-th pair of resonators with the In and Drop ports of the k+1-th pair as:

$$\begin{pmatrix} A_{In_1^{k+1}} \\ A_{D^{k+1}} \\ A_{In_2^{k+1}} \end{pmatrix} = \mathbf{Q^k} \begin{pmatrix} A_{Th_1^k} \\ A_{Ad^k} \\ A_{Th_2^k} \end{pmatrix} = \begin{pmatrix} e^{i\beta D^k} & 0 & 0 \\ 0 & e^{-i\beta D^k} & 0 \\ 0 & 0 & e^{i\beta D^k} \end{pmatrix} \begin{pmatrix} A_{Th_1^k} \\ A_{Ad^k} \\ A_{Th_2^k} \end{pmatrix} \quad (k = 1, .., N), \tag{7.13}$$

we can express the general equations for the device of fig. 65 with a total transfer matrix $\mathbf{S}_{Tot}$:

$$\begin{pmatrix} A_{Th_1^N} \\ A_{Ad^N} \\ A_{Th_2^N} \end{pmatrix} = \mathbf{S}_{Tot} \begin{pmatrix} A_{In_1^1} \\ A_{D^1} \\ A_{In_2^1} \end{pmatrix} = \mathbf{S}^N \mathbf{Q}^{N-1} \mathbf{S}^{N-1} \cdots \mathbf{Q}^1 \mathbf{S}^1 \begin{pmatrix} A_{In_1^1} \\ A_{D^1} \\ A_{In_2^1} \end{pmatrix}. \tag{7.14}$$

And finally, after applying again transformation 7.12, this time to $\mathbf{S}_{Tot}$, we will have the complete set of equations which describe the ports amplitudes as

$$\begin{pmatrix} A_{Th_1^N} \\ A_{D^1} \\ A_{Th_2^N} \end{pmatrix} = \mathbf{T}_{Tot} \begin{pmatrix} A_{In^1_1} \\ A_{Ad^N} \\ A_{In^1_2} \end{pmatrix}, \tag{7.15}$$

which is the generalized version of eq. 7.10.

Figure 66: *Spectral response of the 2x8 SCISSOR switch of fig. 65 with 1, 2, 4, 8 pairs of resonators ((a), (b), (c), (d) respectively), and inputs $A_{In_1} = 1$, $A_{Ad} = 0$, $A_{In_2} = 0$. (Lines as in fig. 61)*

Fig. 66 shows the so obtained spectral response for the 1,2,4, and 8 pair SCISSOR phase switch (fig.66 (a), (b), (c), (d) respectively) with only one input signal. The (N-1) central dips are *not* due to fabrication tolerances ([29], [51]), but are intrinsic due to the existence of the central Drop port between the two resonator chains. The system behaves like a twisted SCISSOR row with asymmetric gaps which introduce a correspondent tiny asymmetric de-phasing at each resonator gap leading to CRIT-like features. It is in this spectral region, near the center of the resonance band, where light couples more efficiently into the resonators and travels repeatedly through them

producing slow light effects. For this reason it is also in this central CRIT-like region where most of the attenuation occurs due to radiation and roughness losses on the resonator bends. Note how, aside from the flat-box spectrum, despite strong input imbalance, the two Through ports response (red dashed and blue dotted-dashed lines) tend to merge together inside the mode's spectral range with the increasing number of resonator pairs. This is because in an N-pair SCISSOR the light that crosses the first pair of resonators provides a less imbalanced input into the following pair, and so on. At the end of the chain the balance between the two signals tends to be restored. This robustness of SCISSOR devices against imbalances could have practical advantages where a precise power injection is uncertain or difficult to tailor.
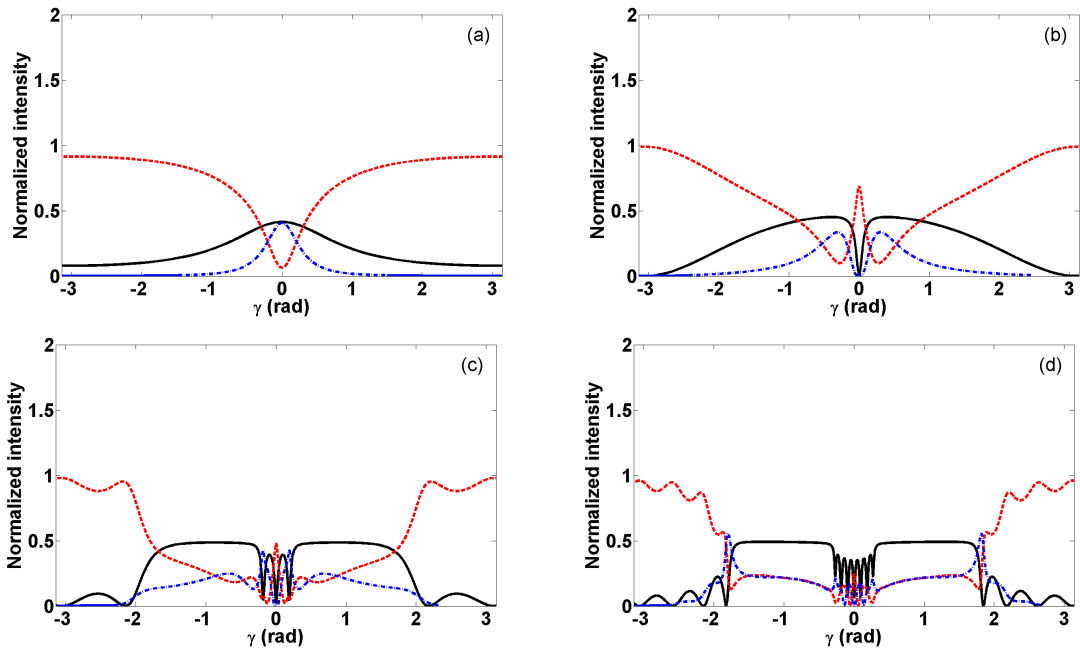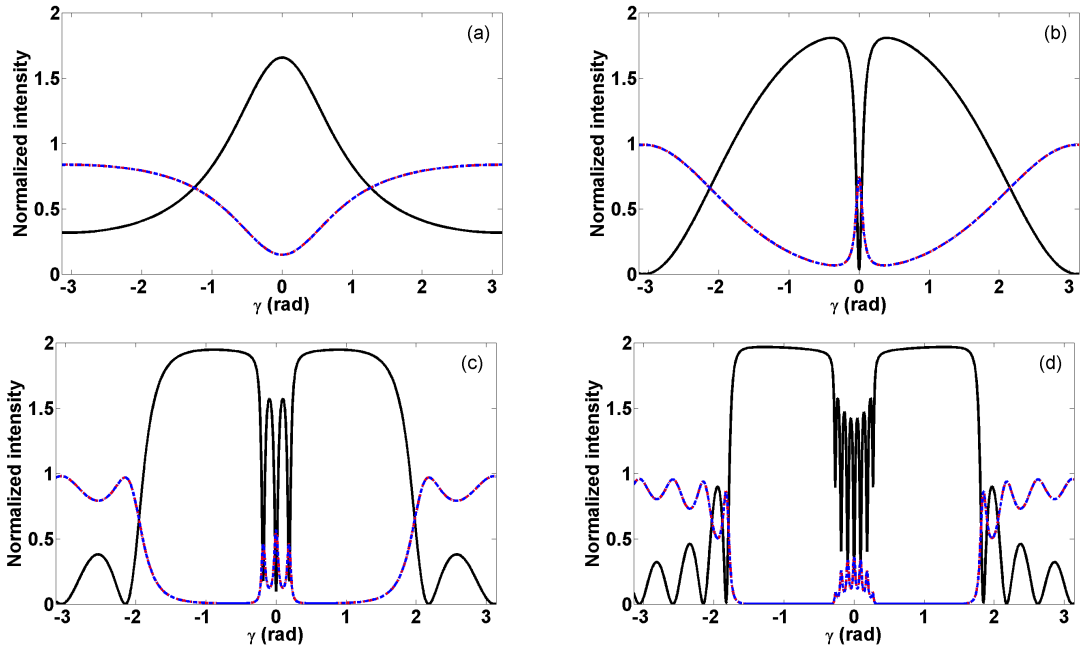

Figure 67: *Spectral response of the 2x8 SCISSOR switch of fig. 65 with 1, 2, 4, 8 pairs of resonators (((a), (b), (c), (d) respectively)), and inputs $A_{In_1} = 1$, $A_{Ad} = 0$, $A_{In_2} = 1$, with same phase. (Lines as in fig. 61)*

Fig. 67 illustrates the previous case but with both input signals switched on having both the same phase. From this one can observe that, in the SCISSOR's resonance band, the flat-box shape and the efficiency with which the two Through port signals are extinguished increases with the increasing number of resonator pairs (flattening of the overlapped blue and red lines in fig. 67 (a)-(d)).
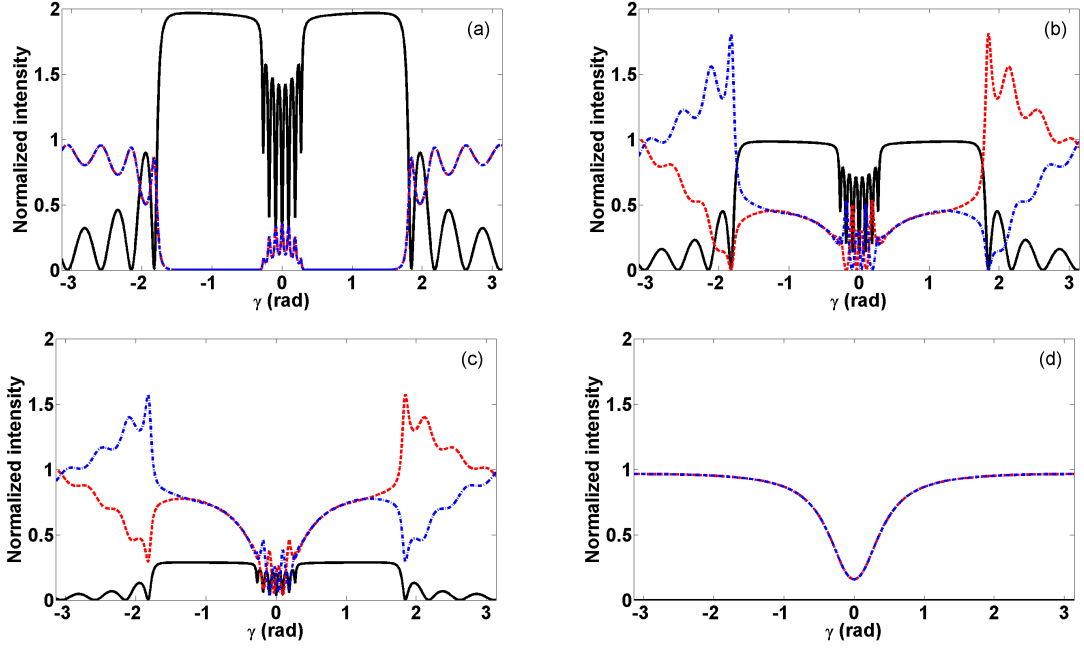
Figure 68: *Spectral response of the 2x8 SCISSOR switch of fig. 65 with inputs $A_{In_1} = (1, e^{i\frac{\pi}{2}}, e^{i\frac{3}{4}\pi}, e^{i\pi})$ ((a), (b), (c), (d) respectively), $A_{Ad} = 0$, $A_{In_2} = 1$. (Lines as in fig. 61)*

How the relative phase change between the two input ports in a 2x8 SCISSOR affects the spectrum is shown in fig. 68. Phase differences of 0, $\frac{\pi}{2}$, $\frac{3}{4}\pi$ and π were applied (fig. 68 (a), (b), (c), (d)) respectively). One observes that, also by applying a phase modulation, the power in the two Through ports tends to be distributed equally along most of the spectral range of the two sidebands of the resonant flat-boxed mode (at about ± 0.4 to ± 1.7 round-trip phase shift), confirming the SCISSOR's effectiveness in balancing the outputs. The 'disengagement' between the two Through ports occurs only, and almost suddenly, when the limits of the band are reached and the system goes out of resonance. The abrupt behavior of the Through signals around $\gamma = \pm 2$ in fig. 68 (b) and (c) is caused by the sidelobe ripplings which are not in phase at the two Through ports. As expected, strong attenuation occurs in the central CRIT-like region (evidenced by the dip in fig. 68 (d)).

The analogue of the input intensity imbalance of the device of fig. 60 and the phase responses of fig. 63 or fig. 64 for the 2x8 SCISSOR switch is shown in fig. 69 and fig. 70.

Figure 69: *Spectral response of the 2x8 SCISSOR switch of fig. 65 with inputs imbalance $I_{In_1} = (1, 0.25, 0.1, 0)$ ((a), (b), (c), (d) respectively), $A_{Ad} = 0$, $A_{In_2} = 1$. (Lines as in fig. 61)*
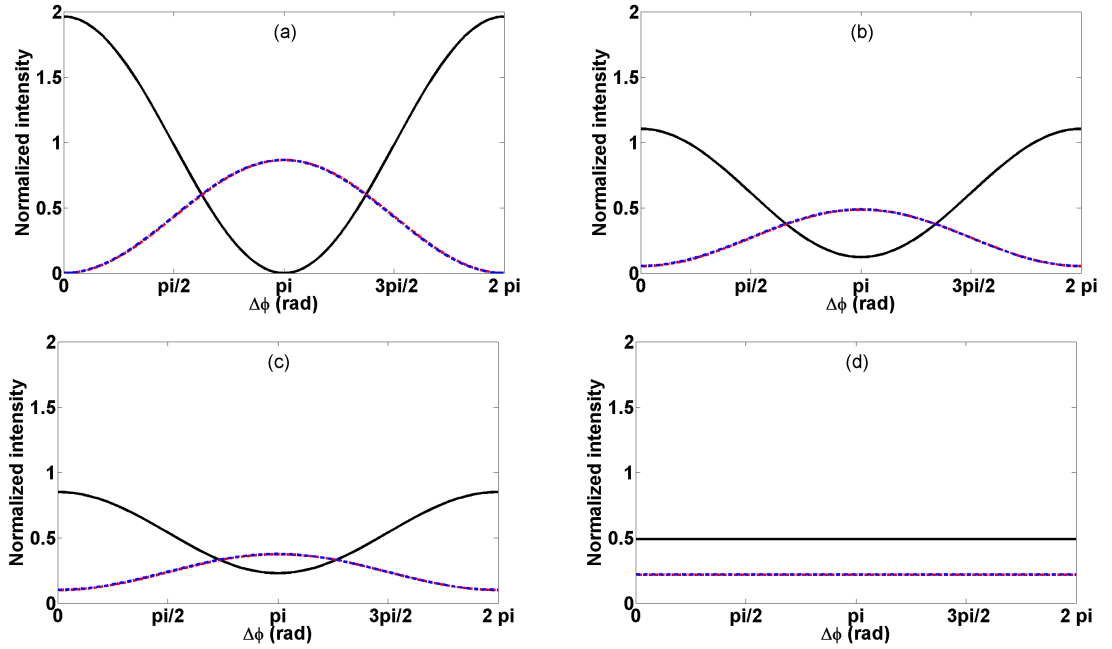
Figure 70: *Phase response of the 2x8 SCISSOR switch of fig. 65 with input imbalances $I_{In_1} = (1, 0.25, 0.1, 0)$ ((a), (b), (c), (d) respectively), $A_{Add} = 0$, $A_{In_2} = 1$, at phase round-trip shift $\gamma = 1$ of fig. 69. (Lines as in fig. 61)*

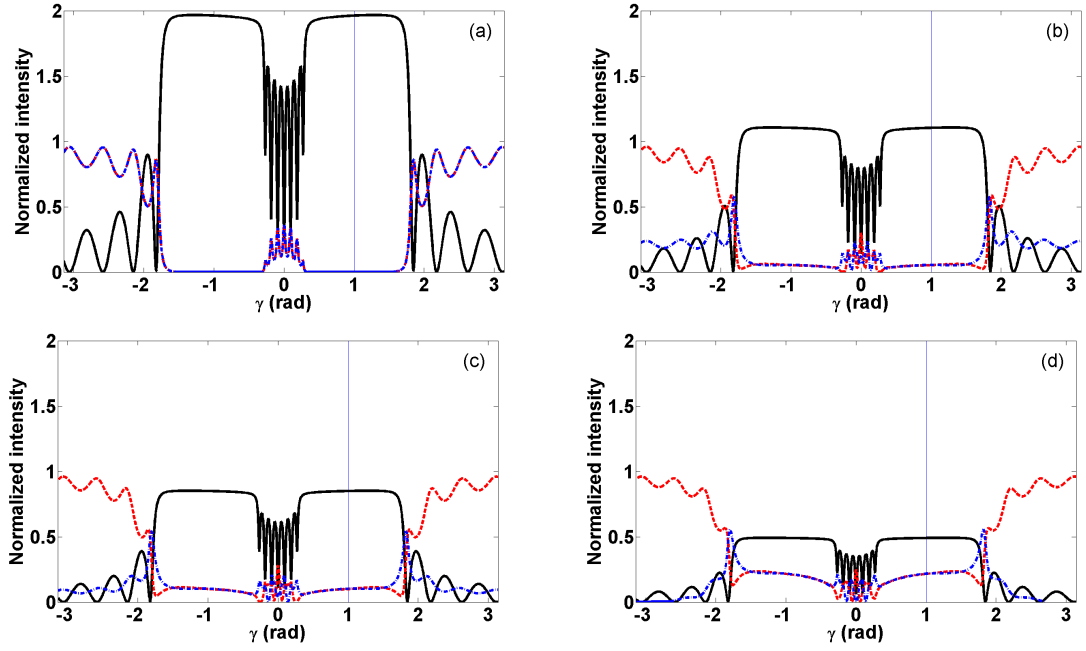Fig. 69 reproduces the response of the 2x8 SCISSOR switch of fig. 65 with inputs imbalance $I_{In_1} = (1, 0.25, 0.1, 0)$ ((a), (b), (c), (d) respectively), and $A_{Ad} = 0$, $A_{In_2} = 1$. The thin vertical line, about $\gamma = 1$, shows the wavelength at which the phase sweep for the four different intensities of fig. 70 has been done. Contrary to the single pair phase switch affected by Fano resonance asymmetries and unequal Through port signal intensities along the phase sweep, the 2x8 SCISSOR phase switch flattens out the differences on the Through ports and again shows its robustness against imbalance.

Another potentially interesting application is the 2x1 phase switch where the add port is used as a third input port. Fig. 71 shows the spectral response of the 2x1 SCISSOR switch of fig. 60 with inputs $A_{In_1} = 1$, $A_{Ad} = e^{i\phi_{Ad}}$, $A_{In_2} = e^{i\phi_2}$ and with some examples of different phase combinations for which one obtains a different light output combination. Fig.71 (a) ((ϕ_1, ϕ_{Ad}, ϕ_2)=(0,0,0)) shows the case of all three equal input
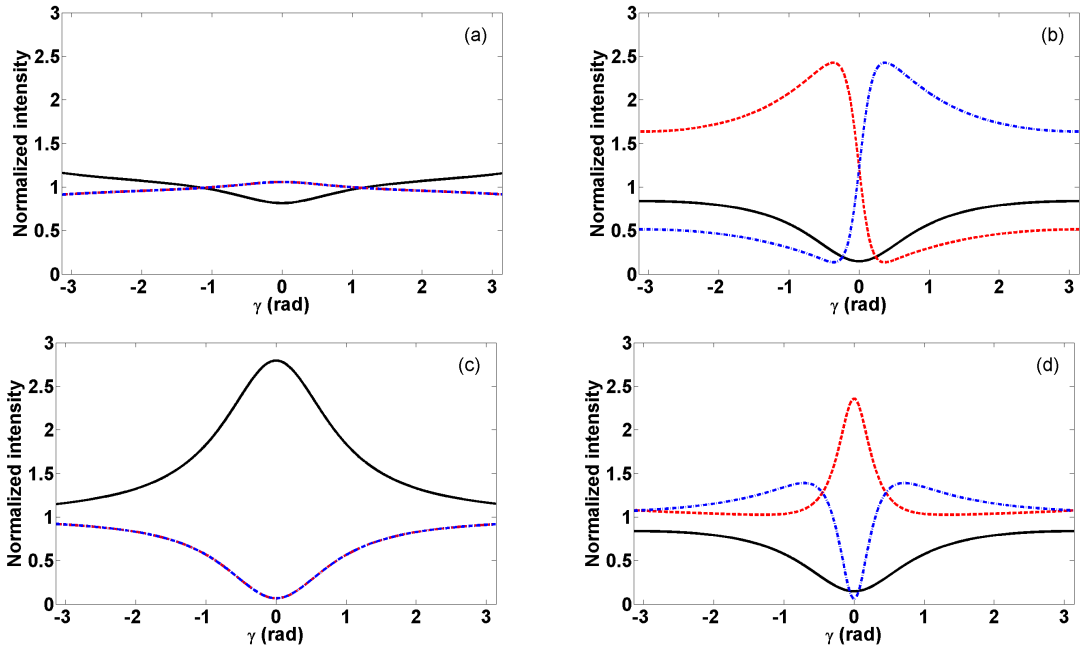
Figure 71: *Spectral response of the 2x1 SCISSOR switch of fig. 65 with inputs $A_{In_1} = 1$, $A_{Ad} = e^{i\phi_{Ad}}$, $A_{In_2} = e^{i\phi_2}$ and (ϕ_1, ϕ_{Ad}, ϕ_2)=(0,0,0); (ϕ_1, ϕ_{Ad}, ϕ_2)=(0, $\frac{\pi}{4}$, $\frac{\pi}{2}$); (ϕ_1, ϕ_{Ad}, ϕ_2)=(0, π, 0); (ϕ_1, ϕ_{Ad}, ϕ_2)=(0, π, π) for fig. (a), (b), (c), (d) respectively. (Lines as in fig. 61.)*

phases: this leads naturally to the direction of light towards all three output ports (with slight differences caused by the bend losses). Fig. 71 (b) reproduces the case ((ϕ_1, ϕ_{Ad}, ϕ_2)=$(0, \frac{\pi}{4}, \frac{\pi}{2})$): at the central resonance wavelength the power is distributed among the two Through ports and almost none into the Drop. Fig. 71 (c) represents the alternative case where only a de-phasing at the Add port is applied ((ϕ_1, ϕ_{Ad}, ϕ_2)=$(0, \pi, 0)$): the power goes into the Drop and almost none into the Through ports. Whereas fig. 71 (d) the Add and one Input port is addressed by de-phasing ((ϕ_1, ϕ_{Ad}, ϕ_2)=$(0, \pi, \pi)$): almost all the light is directed towards the Through$_1$ port. The symmetric case which directs the light towards the Through$_2$ port is obtained by applying the same de-phasing but on the opposite Input port (not shown in the figures).

Many other sorts of combinations in phase and intensity at the Input ports, resonator numbers, and overall resonant device geometry for phase switching applications could be imagined in the most diverse configurations. There is virtually no limit and these wanted to be only some examples which should illustrate the potentialities of light combining and phase switching.

8 First Practical Realizations of Phase Switching SCISSOR devices

The last section was theoretical. To summarize, a three bus waveguide SCISSOR phase switching system device was presented which is able to route light over a broad range of wavelengths by phase modulation. To obtain its behavior it was necessary to analyze first the performance of the two bus waveguide single resonator and SCISSOR and CROW systems. We showed that extending side coupling and Mach-Zhender phase switching techniques to multiple waveguides and to chains of resonators could potentially be useful to enhance their switching capabilities. Many other possible configurations, each of it with several parameters combinations to obtain phase switching, could be imagined. Of course, the potentialities and richness of photonic phase switching is by far not exhausted with the devices presented in this work. However, we believe that herewith we outlined some proposals which display how this is still a field with vast possibilities, hopefully inspiring further investigations of possible applications of novel phase switching devices. An example of design and fabrication of a real device which admits for WDM and switching functions at once, is discussed in this section.

8.1 The SCISSOR phase and λ-router: switching light by phase modulation

We propose to use the coherent overlap of light resonant with two identical SCISSOR for routing. The proposed structure is depicted in fig. 72 and 73. It is composed by two input waveguides (In$_1$ and In$_2$) which are coupled to two SCISSOR devices. The two SCISSOR are in turn coupled by a common central waveguide which identifies the Drop
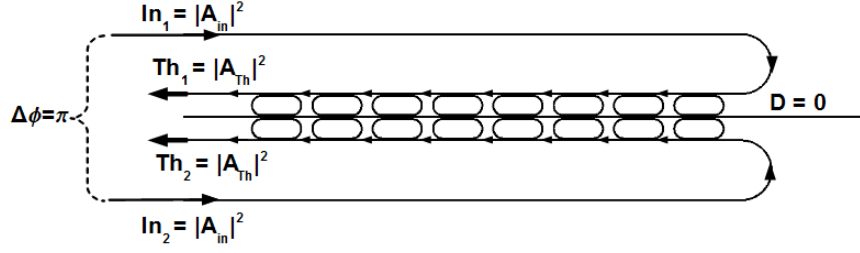
Figure 72: *The SCISSOR router formed by two parallel and coupled eight racetracks SCISSOR. Two input signals (In$_1$ and In$_2$) are inserted in the router from the left. They have a wavelength resonant with the racetrack resonances and a phase difference $\Delta\phi = \pi$. Light interferes destructively at the central common waveguide and the signal (D) on the Drop exit is zero. Instead, the signals are transmitted to the Through ports where the signal intensities are Th$_1$ and Th$_2$. A_{in} and A_{Th} are the field strength in the input and Through ports, respectively.*
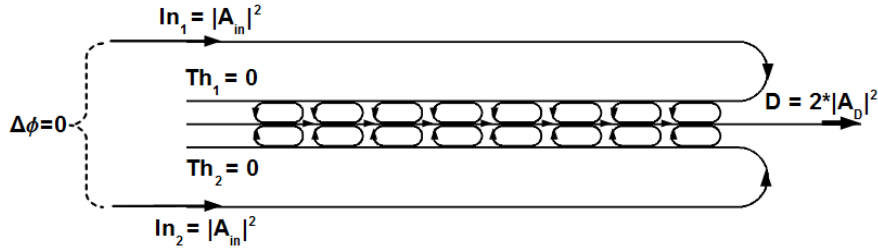
Figure 73: *The SCISSOR router formed by two parallel and coupled eight racetracks SCISSOR. Two input signals (In$_1$ and In$_2$) are inserted in the router from the left. They have a wavelength resonant with the racetrack resonances and a phase difference $\Delta\phi = 0$. Light interferes constructively at the central common waveguide and the signal exits on the Drop port with intensity D. Consequently, the signals (Th$_1$ and Th$_2$) in the Through ports vanish. A_{in} and A_D are the field strength in the input and Drop ports, respectively.*

output port of the router. Depending on the wavelengths of the input signals and their relative phase difference, two ideally equal intensity input signals (In$_1$=In$_2$) are either transmitted to the Through output ports (Th$_1$ and Th$_2$) or to the Drop port (D). When the two input signals are out of phase ($\Delta\phi = \pi$), as shown in fig. 72, they interfere destructively in the common waveguide, no signal is transmitted to the Drop port and
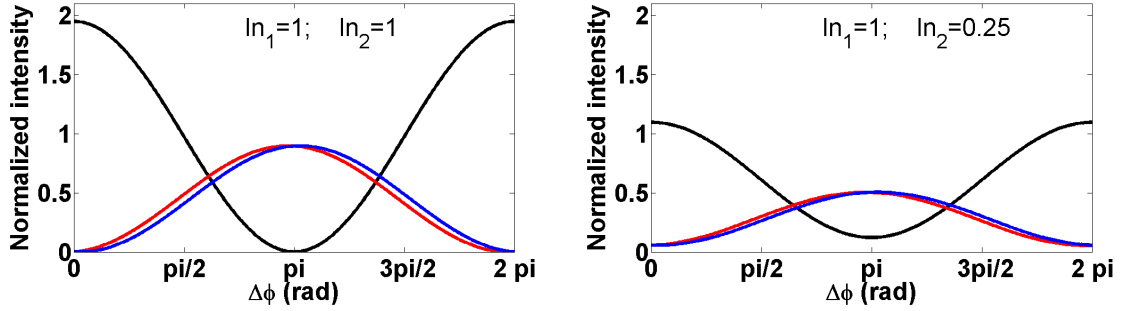
Figure 74: *The SCISSOR router phase response with no inputs imbalance (left) and 75% inputs imbalance (right). The input signal intensities are label In_1 and In_2, the output signals are the two Through signals Th_1 (red line), Th_2 (blue line) and the Drop signal D (black line).*

the signals are transmitted to the Through output ports. If their phase relation is such that constructive interference occurs in the central waveguide ($\Delta\phi = 0$, fig. 73), the two signals add coherently and a signal is transmitted to the Drop output port. Due to power conservation, in an ideal lossless system, this constructive interference produces a signal whose intensity is given by the sum of the two input intensities.

In fig. 72 and 73, two parallel eight racetrack SCISSOR are shown. It is clear that the same phase routing can be achieved by using a lower number of resonators, e.g. a single resonator pair. However, there are several reasons why SCISSOR is advantageous over single resonator geometries. For example, let us consider a situation where strong imbalances between the inputs are present.

Figure 74 illustrates a transfer matrix simulation of the balanced and imbalanced cases. Propagation and bending losses are considered in the simulation. In the balanced case, it is observed that the Drop signal is almost 2 for $\Delta\phi$=0, while it decreases to zero increasing $\Delta\phi$ to π. Concurrently, the Through signals are zero for $\Delta\phi$=0 and increase to almost 1 for $\Delta\phi \to \pi$. Note that both D$\neq$2 or Th$_1$$\neq$1 and Th$_2$$\neq$1 due to the finite propagation losses assumed. The slight asymmetry between the Th$_1$ and Th$_2$ signals is caused by the small differences in their resonant band gap (e.g. see later in fig. 79 left,

112
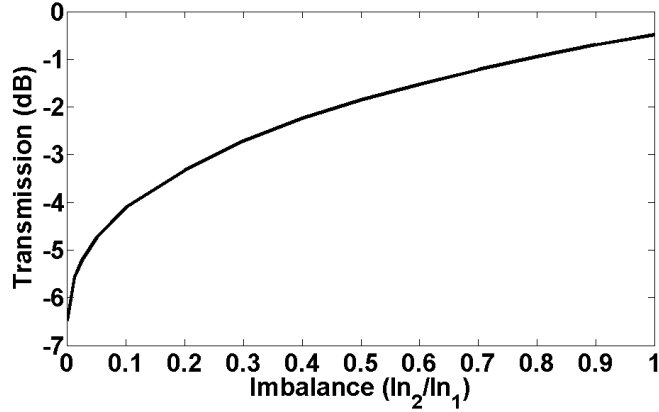
Figure 75: *The Through port intensity (at $\Delta\phi = \pi$) of the SCISSOR router as a function of the input imbalance. Only the intensity of one Through signal is reported since the SCISSOR router response is symmetric with respect to the Through exit ports.*

or the more dramatic case studied in fig. 64). If In_1 and In_2 are different in intensity while resonant with the SCISSOR, the D signal decreases significantly for $\Delta\phi=0$: the effect of the input imbalance starts to be sizeable for a 50% imbalance. Figure 74 right shows the D, Th_1 and Th_2 signals for an imbalance of 75%. It is noted that the D signal does not vanish when In_1 and In_2 signals are out-of balance, while the two Th_1 and Th_2 signals are still equal. This is because in an eight pair SCISSOR router, the signals that resonate with the first pair of resonators provide less imbalanced inputs into the following pair, and so on. At the end of the resonator chain, the balance between the two signals is restored and their intensities sum up to the sum of the two inputs.

Fig. 75 shows how the imbalance affects the maximum of the Th_1 or Th_2 signals by varying the imbalance of the inputs (transmission defined, at $\Delta\phi = \pi$, as $10 \log_{10} \left(\frac{I_{th_{1/2}}}{I_{Th_{ideal}}} \right)$ with $I_{Th_{ideal}} = 1$ the Through signal one expects in the ideal case of the lossless system in perfect balance, i.e. $\frac{In_2}{In_1} = 1$). This is particularly interesting because it demonstrates that this kind of router recovers possible intensity difference in its inputs. Such an effect is not achievable by using a router formed by only two resonators.

113

Another reason to use many side coupled resonators instead of few is to achieve a better coupling of the input signals with the central waveguide for $\Delta\phi = 0$. This leads to a sharper difference in the Drop signal as a function of the phase. Moreover, as we will demonstrate in the next sections, lithographic fabrication imperfections tend to be averaged out with a high number of resonators which yields a more robust design. Finally, the full width at half maximum (FWHM) of the SCISSOR resonances is larger for an increased number of resonators which is needed for band routing functionalities. When the resonator spacing (d_R, the distance between two nearby resonators) is chosen so that the resonator modes and the Bragg modes overlap ($d_R = \pi R$, where R is the radius of the curved part of the racetrack), then also a larger FSR is obtained ([21, 22, 23, 24, 25, 26, 74]). These facts are shown in fig. 36 (a) where 1, 2, 4, 8 resonator SCISSOR are compared (the geometrical parameters of the structure will be given in section 8.2).

Practically, the resolution in the lithography used to produce the router causes fabrication errors. These affect all SCISSOR devices [29] since they cause random statistical variations of the SCISSOR parameters (racetrack geometrical parameters, racetrack to waveguide gap, relative positions of racetracks with respect to the common waveguide, etc.) at the nanometer scale. These variations affect also the relative phase of the signals since their optical paths might differ. A comparison of the Drop signal spectrum of an ideal SCISSOR, fig. 36(a), and of a SCISSOR with 5 nm random variation in the geometrical parameters, fig. 36(b), shows the appearance of noisy dips within the resonance band. These dips are the evidence of disorder induced optical mode localization as discussed in [29]. Their presence limits the range of wavelengths that can be properly routed by SCISSOR.

114

8.2 Modelling, mask design and fabrication

The modelling and simulation of the router were performed via three steps: waveguide parameter estimation, circuit response modelling and silicon device component simulation. Parameter estimation was carried out with a full vectorial finite difference mode solver [69]. For instance, we had to determine the wavelength dependent racetrack coupling section lengths and the coupling constants, as explained in section 3, and obtain from these parameters the proper gap spacings. Results are published in [74]. With these parameters, we perform the simulations of the spectral response of the single SCISSOR and their combination as in the proposed geometry to analyze the Drop and Through port signals as a function of the phase difference of the input signals, as explained in section 7. This was done by using a transfer matrix method applied to each block of the coupled SCISSOR structure. Finally, we simulate the other photonic components in the router, like waveguide crossings, multimode interference (MMI) splitters and tapers. These were designed with a commercial Finite Difference Time Domain (FDTD) package (see section 5.1). All simulations assumed TE-polarization and SOI waveguides.
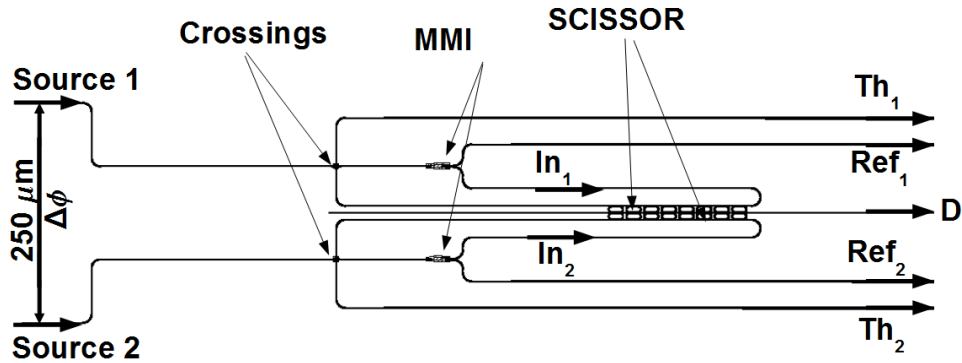

Figure 76: *Layout of the SCISSOR phase router of fig. 72 and 73. Co-directionality between input and output is achieved by bending the Th_1 and Th_2 signals on the right device side.*

Figure 76 reports the layout of the router. The input ports have been separated by a

distance which allows the simultaneous use of two tapered fibers to input the signals. Reference waveguides are used to monitor the input signals which reach the SCISSOR. To this end, an MMI splits the input signal in two waveguides: the Reference waveguide and the real SCISSOR input waveguide (it is the signal in these waveguides which we have used in the previous calculation and called In_1 and In_2). It is also desirable to have all the inputs on one side and the outputs on the other side. For this reason, the waveguide after the SCISSOR is bent to take the Through signals on the right device side. This forced us to insert two waveguide crosses.

This design was then transferred to a mask and processed on SOI wafers by using the processing facilities of CEA, LETI. The wafers were 200mm SOI wafers with a 220nm thick Silicon and $2\mu m$ thick buried oxide. The pattern definition was achieved by using state of the art DUV 193nm lithography. Different exposure doses were used to change few critical feature sizes, such as the gaps. The silicon waveguide and the other photonic components were then covered by a $0.75\mu m$ thick SiO_2 layer which acts as waveguide cladding layer as well as a protective layer. The waveguides were designed with a width of $0.5\mu m$, the waveguide-racetrack gaps were 200 nm, the racetracks have a radius of $R = 3.25\mu m$ and a straight section of $L = 10\mu m$. For this radius, the process yields a measured bending losses of about $0.025dB/90°$ (measurements done on a series of 100 bends).[76] It is customary to define the distance d_R as the distance between the centers of the half circumference of two facing racetracks. In our case d_R=10.21 μm. To decrease the coupling losses, tapering of each input and output waveguides was used. A $500\mu m$ long adiabatic taper reduced the waveguide width from $2\mu m$ down to $0.5\mu m$. The crossings and MMI splitters were processed by using a double etch processes in which a 70 nm shallow etch is followed by a 150 nm deep etch. This double etch scheme was based on the low insertion losses cross design of Ref. [77]. Measurements on a chain of cascaded crosses show 0.35 dB loss per crossing with a crosstalk of about $-27dB$ and

116

a back-reflection of 0.17% while the major contribution to losses (3.6%) comes from scattering. The MMI design was the same as in [8] and had about 0.4dB insertion losses with, however, a strong impairment between the two output channels possibly due to layer misalignment during the fabrication process. This impairment made very difficult the use of the Reference signals for intensity normalization.

8.3   Experimental characterization and results
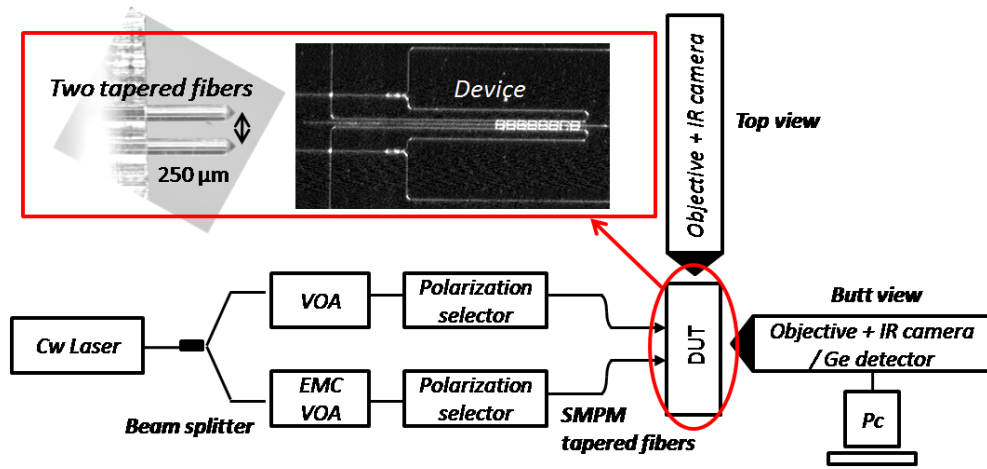
Figure 77: *Experimental setup used to test the router (VOA: variable optical attenuator, EMC: electro-mechanical, SMPM: single mode polarization maintaining, DUT: device under test).*

.

The set up used to test the router is shown in fig. 77. It is a standard set-up for waveguide measurements apart the input section. In fact, we need two input signals which are coherently controlled in phase. To achieve this, the output of a single CW tunable laser is connected via a fiber splitter to two polarization maintaining fibers. Each fiber is then connected to a polarization selector and a variable optical attenuator (VOA) in order to independently tune the polarization and intensity of the signal in each fiber. One of the VOA (named EMC-VOA) can be controlled electro-mechanically in order to have an attenuation sweep linear in time. Due to the fact that attenuation in

the VOA is achieved by misaligning the input and output VOA fibers, an attenuation change leads also to a different optical path in the VOA which, in turn, translates into a phase change of the optical signal. Therefore, during the attenuation sweep we achieve both a different ratio of the intensities of the signals in the two fibers and a phase shift of the signal in one fiber with respect to the signal in the other fiber. The two fibers are then connected to two polarization maintaining tapered fibers which are mounted on a special holder with two V-groove separated by $250\,\mu m$. The signals are then coupled into the device under test (DUT) by butt coupling where the fiber to waveguide alignment is controlled by a nanometer piezoelectric positioning system. This experimental set-up allows to get the DUT response either to a wavelength scan of one of the two input signals or to a relative phase scan of the two input signals with a fixed wavelength.

The five output signals (Ref$_1$, Ref$_2$, Th$_1$, Th$_2$ and D) are then measured either independently and in sequence with an optical zoom coupled to a Ge detector or simultaneously by imaging the whole output facet of the DUT into an IR CCD camera. Then, by an image processing software, the intensity of each spots corresponding to each output is obtained as a function of the input signals. The set-up allows also imaging the scattered light on the DUT surface into another IR camera and by image processing select specific router area to measure the intensity of the scattered light as a function of the input signals.

The first measurement performed is the spectral response of the router. We used a wavelength interval corresponding to a resonator resonance and not to a Bragg resonance. In fact for a Brag resonance neither the Drop nor the Through signals go to zero in resonance.[29] Our experimental set-up does not allow to perform a wavelength scan for a controlled and fixed phase difference between the two inputs. For this reason we could only make a wavelength scan for a single input. For a single input, the Drop and two Through spectra are reported in fig. 78. We observe a wide pass-band which

118
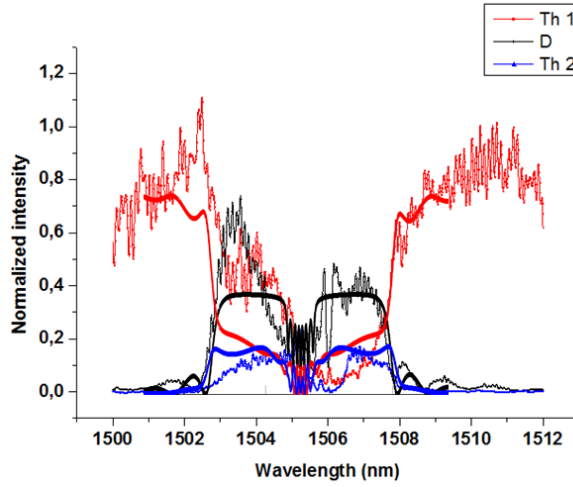
Figure 78: *Through and Drop port spectra (black, blue and red lines respectively) measured for the eight SCISSOR router when a single signal In_1 is input. The intensity at the Through port 2 (Th_2, blue line) gives the cross-talk. The thick continuous line represents the theoretical expected response.*

extends for almost 6 nm. Here the signal instead of being transmitted to the Through ports is resonantly coupled with the central waveguide (Drop signal, black line). Due to the above mentioned limit in the processing, few dips appear in the center of the pass-band. The dips in the pass-bands limit the available spectral range to the two lateral sidebands. Because of the power splitting imbalance in the MMI, the measured spectrum is asymmetric with respect to the resonance as would be expected in the ideal structure. Despite these experimental limitations, the agreement between the measured and simulated spectra is satisfactorily. It is interesting to note the large cross-talk from channel 1 to channel 2 as measured by the signal at the output Through port 2 (blue line). When the signal wavelength is within the pass band, the signal leaks to the other output Through port.

The simulated spectrum with a signal only in the In_1 (the continuous lines in fig. 78) is shown also in fig.79 left to compare it with the case where both inputs are injected with an equal intensity and are in phase (fig.79 right). In this way, we can evaluate the

119
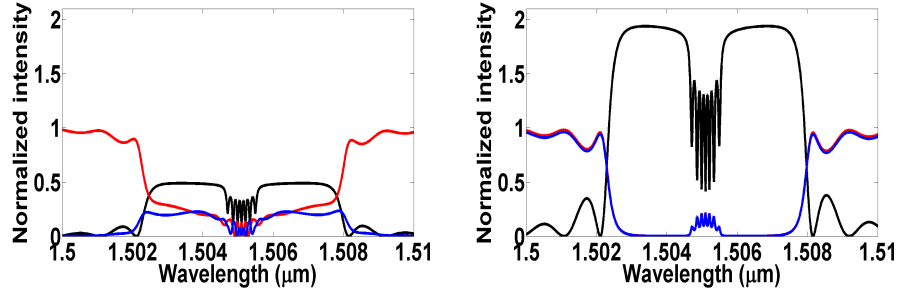
Figure 79: *Spectra of the Th_1 (red line), Th_2 (blue line) and D (black line) outputs for the eight SCISSOR router with only one input signal (left) and both input signals with the same phase (right).*

cross-talk and the response under strongly imbalanced inputs. We note that for the former case (fig.79 left) the Drop signal shows an intensity which is only half the one of the input. The Th_1 signal is complementary to the D signal with two remarkable features: out of the pass-band its intensity reaches almost 1, in the pass-band it does not go to zero. This is due to the cross-talk between the two SCISSOR which causes a non-zero signal intensity also at the Th_2 output in the wavelength range of the pass-band. To decrease the cross-talk one has to balance the intensity of the input signals and to increase the number of resonators in the SCISSOR. This is shown in the right of fig. 79, where the simulations are performed for the same structure but with two input signals of same intensity and phase. Now the spectral response is the one expected with two equal output Through signals and zero Through signal in the pass-band.

The phase dependence of the outputs from the router when the signal wavelength is within the Drop pass-band is shown in fig. 80. A signal wavelength of 1534.95 nm was used. The phase change was obtained by sweeping in time the attenuation of the EMC-VOA (In_2 intensity sweep). We then correlate the time with the phase shift by using the 2π periodicity of the oscillations of the output signals. The response of the router when the two input signals have equal intensity can be found when the D signal vanishes (red box in the figure, blow up in the insert).

120
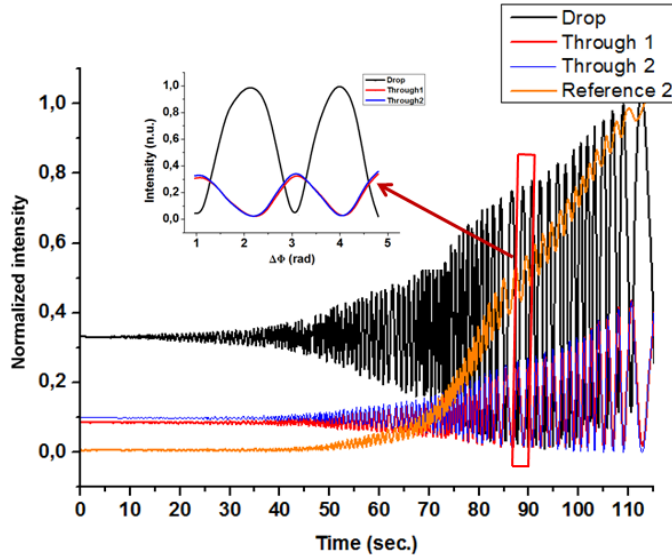
Figure 80: *Drop (black line), Through 1 (red line), Through 2 (blue line) and Reference 2 (orange line) signals as a function of the amplitude sweep of one of the two input (In₂) of the eight SCISSOR router of fig. 76. (Inset) Phase response of the device when the two input signals have the same intensity (red box region in the main graph).*

The black, red and blue lines represent the D, Th_1 and Th_2 signals, respectively. The orange line represents the Ref_2 signal (Reference for In_2). It is observed that the phase difference between the inputs affects significantly the Drop signal only when the two input channels are increasingly balanced. In fact, the oscillations on the D signal are large only when Ref_2 increases. In addition, the same behavior in the Th_1 and Th_2 signals is observed. A detail of the phase response of the router when the inputs are balanced is shown in the inset of fig. 80. Clear oscillations due to constructive and destructive interference on the central waveguide are observed both in the Drop and Through signals. This proves that the proposed router can be used both as a phase and a wavelength router. Where the input signal is routed depends both on the signal wavelength and on the signal phase. The observed profiles are not perfectly sinusoidal for an experimental limitation which is related to the noisy mechanical sweep of the EMC-VOA. Due to losses, mainly scattering losses, the sum of the two out-of-phase

121

Through signals does not equal the in-phase Drop signal. This is also observed in the simulations of fig. 74. Note also how, in the balanced case, the two Through signals are almost equal, as expected from the simulations. This correspondence is not always observed due to the slight asymmetries of the Through response.
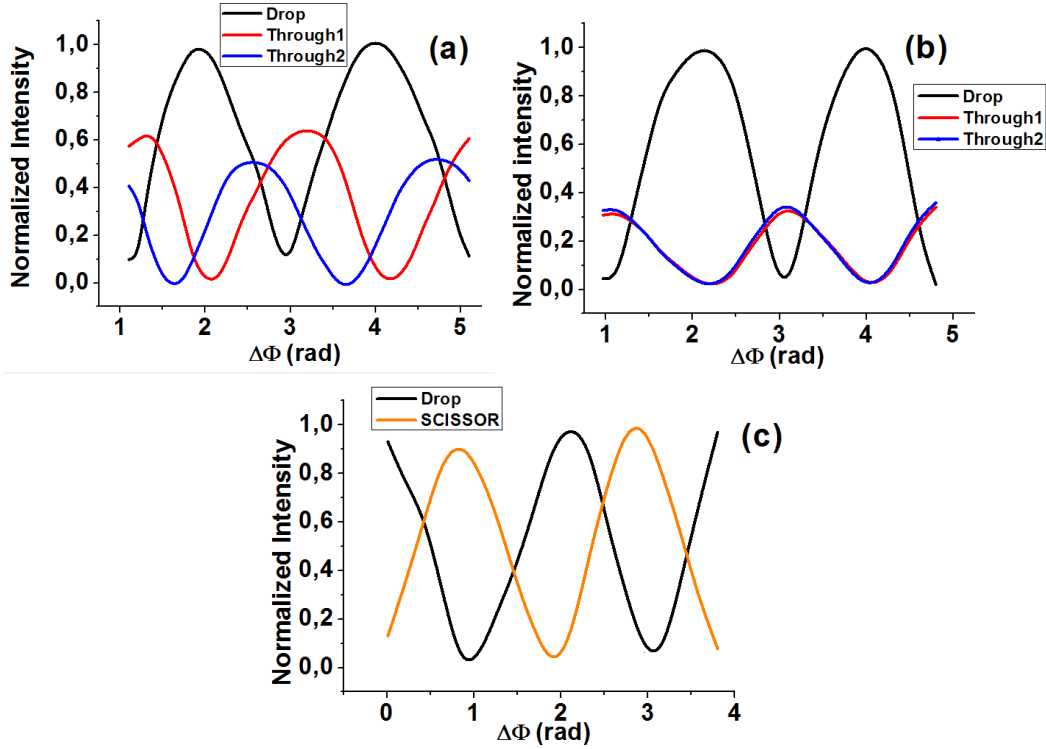
Figure 81: *(a) Phase response of a one pair SCISSOR router ($\lambda = 1542.25$ nm) and (b) of an eight SCISSOR router ($\lambda = 1534.95$ nm). (c) Top scattering of the eight SCISSOR router from the common waveguide area (D channel, black line) and from the resonators area (orange line)($\lambda = 1528.6$ nm). All graphs are normalized to the maximum amplitude of the D channel.*

Figure 81 shows the comparison between the phase response for two routers: one based on one racetrack pair (fig. 81(a), $\lambda = 1542.25$ nm), and the second based on eight racetrack pairs (fig. 81(b), $\lambda = 1534.95$ nm). In addition, we show in fig. 81(c) the top scattering curves of the eight racetrack pair router ($\lambda = 1528.6$ nm). These are taken by numerically integrating a given portion of the top IR image of the DUT: the area of the

central common waveguide for the black curve (the resulting intensity is proportional to the Drop signal) and that of the eight pairs of racetracks for the orange curve (the resulting intensity is proportional to the light intensity propagating in the resonators). From these data it emerges that both one and eight pair routers follow the predicted behavior. In particular, the one pair design shows an extinction in the Drop channel of 9 dB and the amplitudes of the Through signals in destructive interference state sum up to the value of the Drop signal in constructive interference state. This means that this design has a good capacity of redirecting the signals in the Through ports without introducing significant losses. It is, however, observed a shift between the extreme of the Drop and the two Through signal maxima. This is probably due to a non perfect alignment of the center of the racetracks which introduces a further uncontrolled phase shift for the signal propagating in one or the other Through waveguides. On the other hand, the eight pair design shows a Drop extinction of 15 dB, thanks to the higher number of racetracks. However, extra losses are observed and the Through signals have lower intensities than for the one pair resonator router. Figure 81(c) explains the origin of these extra losses. When the Drop signal shows a minimum in the scattered intensity, the interference is destructive. In this case we observe that the scattered intensity in the SCISSOR is maximum. These observations show that, when destructive interference occurs in the common waveguide, the light signal couples back into the racetracks where it is partially radiated by the scattering. This behavior is detrimental for routing and needs to be improved for practical purposes.

Another effect that can be noted in fig. 81 (a) and (b) is the phase offset between the Drop and the two Through signals. This is a consequence of the random variations in the racetrack parameters, which randomize in turn the relative phase of the Drop and the two Through signals. If the input signals In_1 and In_2 are in phase, they have nevertheless to go through two different optical paths if the resonators differ. This leads

to an offset of the Drop signal from the ideal expected extinction at phase difference $\Delta\Phi = 0$. To quantify this, we measured seven different but nominally equal one and eight SCISSOR routers. We statistically quantify the influences of fabrication variations by measuring the phase difference between the two Through signals ($\Delta\Phi_1$ and $\Delta\Phi_1$ for the one and eight SCISSOR router respectively), and their maximum amplitude difference

$$\Delta A = \frac{|Th_1 - Th_2|}{(Th_1 + Th_2)/2} \, .$$

$\Delta\Phi_1 \pm \sigma_{\Phi_1}$	$\Delta A_1 \pm \sigma_{A_1}$		$\Delta\Phi_8 \pm \sigma_{\Phi_8}$	$\Delta A_8 \pm \sigma_{A_8}$
0.34 ± 0.12	0.4 ± 0.17		0.02 ± 0.03	0.24 ± 0.15

Table 6: *Comparison of the phase ($\Delta\Phi_{1,8}$) and amplitude ($\Delta A_{1,8}$) differences between the one pair (left) and eight SCISSOR (right) router.*

Table 6 reports the average values for the one and eight SCISSOR router (left and right respectively). It is observed that the eight SCISSOR router is much more robust with respect to fabrication variations (smaller averages) than the one pair router. This is a consequence of the collective behavior of the SCISSOR which smoothes out statistical imperfections with an increasing number of resonators. Therefore, there is a trade-off between the robustness and the losses when designing the number of racetracks in the SCISSOR router.

8.4 A reconfigurable SCISSOR phase and λ-router

The possibility to reconfigure the router can be further exploited by combining coarse and dense WDM as shown in fig. 82.

For clarity the figure has been divided in three modules. The first module is responsible for the phase control. An input signal is split into two parts by an MMI splitter. Both
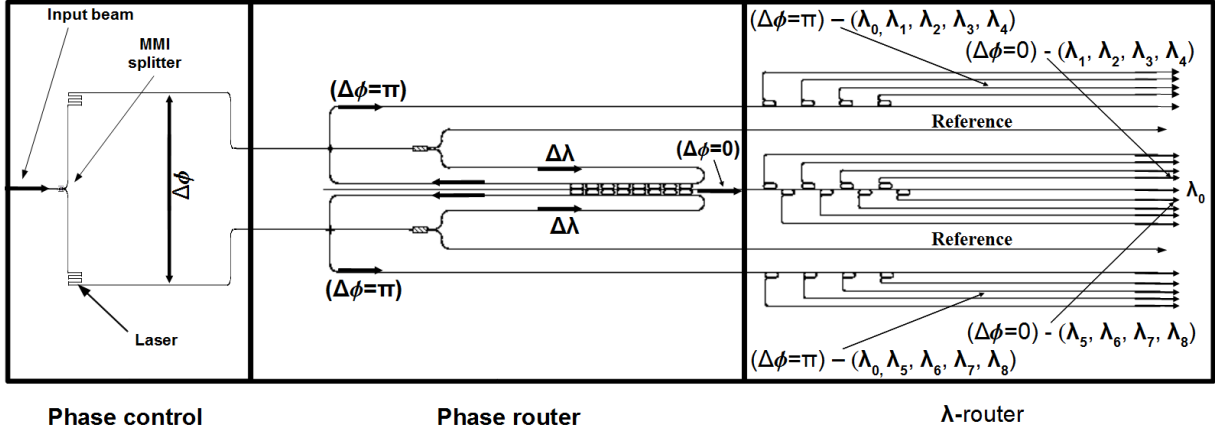
Figure 82: *Phase switching and λ-routing.*

are then directed towards a waveguide serpentine, one of which has the function to capture the light from a laser beam. This laser light spot, by inducing free carriers in the serpentine waveguide section, modulates slightly the effective index introducing a corresponding phase shift, according to the laser intensity. After appropriately tuning the phase with this phase modulation technique, the two phase shifted signals go into the phase router module where a spectral band, $\Delta\lambda$, is directed towards the parallel SCISSOR and therefore towards the middle waveguide (if $\Delta\phi = 0$) or the two Through ports (if $\Delta\phi = \pi$). Subsequently, in the third and final λ-router module, the signal is split into denser channels (λ_{1-4} or λ_{5-8} respectively) by another channel routing system (here as an example a 1×8 router), that can be designed with high quality factor resonators.

This combination of a phase and a λ-router shows the principle with which phase modulation can be employed for reconfigurable networks where the channels obtained by a standard WDM routing system can be doubled, i.e. we obtain a $2 \times (1 \times N)$-SCISSOR-λ router, where N is the number of channels that can be addressed towards the two different outputs. Fig. 82 is similar to the mask design which was fabricated in one of our wafers, but for graphical clarity we depict it with $N = 8$

125

output channels instead of the $N = 10$ channels of the real device. In fact, we employed the same small racetracks of the previous sections to maintain a small footprint but in order to obtain a higher quality factor the gap separation was increased ($R = 3.25\mu m$, gap=$300\mu m$, and $L = 9.92 - 10.10\mu m$ in steps of 20nm). However, the choice of 10 channels was deliberately over numbered in order to be sure that all the FSR would have been covered and that the appropriate channels could be chosen selectively also after the fabrication at a later stage of experimental characterization.
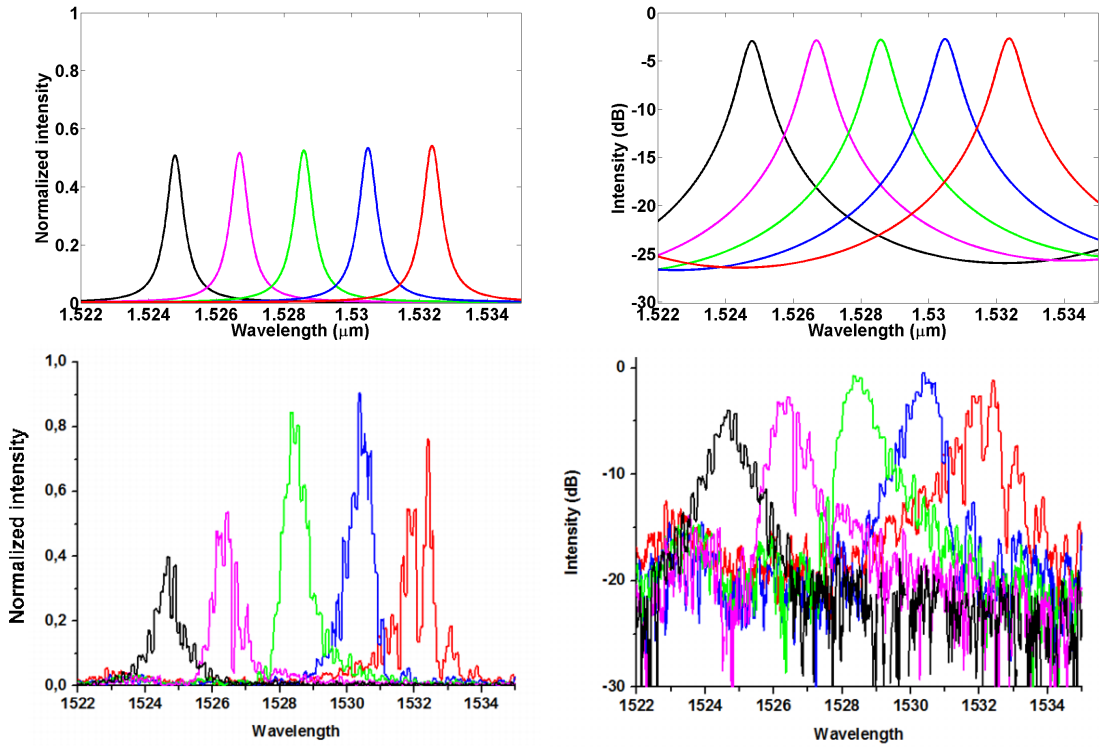
Figure 83: *Spectral response of the phase and λ-routing device of fig. 82 for five channels.* **Top:** *Expected spectrum.* **Bottom:** *Measured spectrum; (left: normalized intensity, right: logarithmic scale).*

This is what has been done in fig. 83 which shows the simulated and measured spectra in the top and bottom graph respectively (in normalized intensity on the left, and in logarithmic scale (dB) on the right) for the Drop port of the device in fig. 82 at five

channels when no phase difference was applied. These channels are routed towards the Drop and were clearly separated by the resonators afterwards as expected. The match between the predicted and measured signals is good. Only a discrepancy in the intensities has to be observed. The peaks were expected to have the same intensity while the measurements show to be somewhat resonator dependent. This is possibly caused by the gap randomization at each resonator induced by fabrication errors (here a gap of 300nm, larger than in other applications considered in this thesis, and which, because of the exponential decrease of the power coupled with increasing spacing, becomes more sensitive to these fabrication errors for larger gaps). By applying a phase difference at the input it was possible to see how the intensity of these peaks decreased and how they appeared on the two Through ports proving experimentally that indeed phase switching with λ-routing is possible. The measured spectrum was normalized to the largest measured output peak at the Drop port (in the simulation to the power in the input bus, here the Drop port), and therefore does not directly account for the total loss of the device. A direct measurement of this wasn't possible because the effectively coupled input power in the waveguide (input beam in fig. 82) was unknown and therefore it wasn't possible to normalize the measured signal over the real input power. However, from our discussion on the MMI, crossing, coupling, and bend losses in section 5.1 one can nevertheless estimate the total loss as follows. Following the light path in fig. 82 it undergoes 9 times a 90° bend of −0.025 db/90° loss, i.e. a 0.225 dB loss, it encounters two MMIs (−2 × 0.4 dB=-0.8 db), one crossing (-0.35 dB). The loss across the SCISSOR switch is low compared to single resonator losses, as also fig. 67(a), 68(a) or 69(a) show. This again is because of the efficiency of a chain of resonators to couple efficiently almost all the light towards the Drop port, only the coupling and bend losses are left, and which can be estimated from the simulations of fig. 36 to be less than -1 dB. From simulation of fig. 83 (top, right) about -3 dB loss are to expect at the

λ-router resonators. Finally, the material losses declared by the processing facility of CEA, LETI is about -1 dB/cm. Even tough our devices were much smaller than 1cm, (for comparison, the largest structures, the eight SCISSOR switch, is about 150 μm long), due to multiple round trips light travels in the resonators and the fact that the dies fabricated are about 6mm long, to remain conservative we add -1 dB for the material loss. Therefore, the overall loss is about -6.4 dB, which is still acceptable, especially considering that future improvements and optimizations can lower this value further. From fig. 83 one sees that the crosstalk between the channels is about, or for some channels even less, than $-10dB$, which is a good achievement for a first proof of concept device and can be optimized further too (e.g. by gap engineering vs. power losses). The same could be said about the channel density. In order to be sure to get a strong and easy to detect signal low quality factor resonators for this final λ-routing stage were chosen (about $Q = 1500$) and, on a FSR of about 8 nm, each channel has only about 1nm FWMH which does not lead to high channel densities. However, considering that higher quality factors of an order of magnitude or even more are possible with current technology, it is foreseeable that an arrangement of about hundred channels in future optimized devices could be realized.

.

9 Conclusion

We modeled and designed some novel photonic λ-routing and phase switching devices based on SCISSOR. Simulations were compared with experimental measurements of the designed PIC. The experimental test furnished a first proof of concept of some proposed micro-optical CWDM devices and how light switching is achieved according to the phase difference of two input signals.

The overall conclusion is that different structures with similar routing and/or switching functions are possible. They differ essentially in the geometry and their performance is highly dependent from the fabrication parameters, as for example the correct choice of the waveguide structure, the proper choice of the resonant devices arrangement and the parameters characterizing it (gap spacings, coupling sections, etc.). The degrees of freedom are so many that resorting to numerical simulation is no option but an indispensable step without which any practical realization in wafer fabrication, which offers a costly trial only each several months, would not be possible.

Current technologies however still limit their full performance because of the randomization of the parameters induced by fabrication errors. Therefore to compare and evaluate the pros and cons of each device it will be necessary to fabricate and test directly further some of these structures on chip. Nevertheless, it was shown that the proposed devices work as expected and that the physics which govern them is well understood.

These were only some examples of potential applications of cascaded resonator structures (and also others have been proposed elsewhere [88] [89]). But next generation electron beam- or extreme ultraviolet lithography promise to lower fabrication errors of an order of magnitude, making the proposed SCISSOR-routing and phase-switching systems we discussed a valuable approach which can complement other existing routing

and switching technologies.

From a theoretical perspective also more sophisticated phase switching schemes were investigated. We believe that further design optimizations and especially the upcoming new lithographic technologies will dramatically improve photonic device performances making these structures feasible and paving the way to new still unexplored routing and switching functions. In my opinion the phase switching functions of SCISSOR and CROWS via multiple bus ports, as investigated in section 7, is still an unexplored domain with possibly several unexpected potential applications waiting to be discovered and which should be pursued further. But only history will tell for sure which technology will win. A history I'm glad to participate in.

10 Acknowledgments

This PhD thesis would not have been possible without the contribution from many people.

I am grateful to Prof. Lorenzo Pavesi, my supervisor and head of the Silicon Photonics group of the University of Trento, for his continuous support, several useful and important advices, suggestions and ideas which undoubtedly gave momentum and extra strength to my work.

I thank Régis Orobtchouk for sharing with me his powerful mode solver code, and because he left me full freedom to explore my own ideas and creative potentialities during my four month stage at INL from which the TMM code was born and with which later the phase switching ideas could be explored further.

I express my gratitude to Manga Rao Vanacharla who was very helpful in designing especially the first wafer and whose expertise in FDTD simulation I will certainly miss.

I can't forget the contribution of Mattia Mancinelli and Alberto Battarelli for their large amount of measurements which became the base of the experimental validation.

I and the silicon photonics group of the physics department of the university of Trento acknowledge the support of the EU through the FP7 ICT-(216405) project Wavelength Division Multiplexed Photonic Layer on CMOS.

11 Appendix

In fig. 60 we can relate $(A^2_3, A^2_4, A^2_5) \rightarrow (A^1_3, A^1_4, A^1_5)$ through eqs. 2.65, 2.66 and 2.67 as:

$$\begin{pmatrix} A^1_3 \\ A^1_4 \\ A^1_5 \end{pmatrix} = \mathcal{M} \begin{pmatrix} A^2_3 \\ A^2_4 \\ A^2_5 \end{pmatrix} = \begin{pmatrix} t' & i\kappa_D & -\kappa' \\ i\kappa_D & t_D & i\kappa_D \\ -\kappa' & i\kappa_D & t' \end{pmatrix} \begin{pmatrix} A^2_3 \\ A^2_4 \\ A^2_5 \end{pmatrix} . \tag{11.1}$$

Proceeding in the same way as we have done with matrix $\mathbf{M}$ of eq. 4.9, we look for the coupling matrix that relates in the interference section the upper to the lower waveguide through the middle one, i.e. $(A^2_3, A^2_4, A^1_3) \rightarrow (A^2_5, A^1_4, A^1_5)$, and obtain the second transfer matrix $\mathbf{T^b}$:

$$\begin{pmatrix} A^2_5 \\ A^1_4 \\ A^1_5 \end{pmatrix} = \mathbf{T^b} \begin{pmatrix} A^2_3 \\ A^2_4 \\ A^1_3 \end{pmatrix} = \frac{1}{\kappa'} \begin{pmatrix} t' & i\kappa_D & -1 \\ i\kappa_D(\kappa' + t') & t_D\,\kappa' - \kappa_D^2 & -i\kappa_D \\ t'^2 - \kappa'^2 & i\kappa_D(\kappa' + t') & -t' \end{pmatrix} \begin{pmatrix} A^2_3 \\ A^2_4 \\ A^1_3 \end{pmatrix} . \tag{11.2}$$

Due to symmetric coupling, $\mathbf{K}$ of eq. 4.11 can be applied also at $(A^1_6, A^2_6) \rightarrow (A^1_7, A^2_7)$. For the same reason the same internal propagation matrix of eq. 4.12 can be applied also at $(A^2_5, A^1_5) \rightarrow (A^1_6, A^2_6)$. Therefore the third transfer matrix connects $(A^2_5, A^1_5) \rightarrow (A^1_7, A^2_7)$ in the same way as eq. 7.1 (but with the order of the propagation and coupling matrixes inverted):

$$\begin{pmatrix} A^1_7 \\ A^2_7 \end{pmatrix} = \mathbf{T^{KP}} \begin{pmatrix} A^2_5 \\ A^1_5 \end{pmatrix} = \mathbf{KP} \begin{pmatrix} A^2_5 \\ A^1_5 \end{pmatrix} . \tag{11.3}$$

To proceed in the inverse direction, i.e. from $(In_2, Through_2)$ to $(In_1, Through_1)$, note that, again because of coupling symmetry, $\mathbf{T^{PK}}$ relates also $(A^1_7, A^2_7) \rightarrow (A^2_5, A^1_5)$, $\mathbf{T^{KP}}$ does the same with $(A^2_3, A^1_3) \rightarrow (A^1_1, A^2_1)$), and that $\mathbf{T^b}$ connects also $(A^2_5, A^2_4, A^1_5) \rightarrow (A^2_3, A^1_4, A^1_3)$.

Now we can obtain the overall device response of fig. 60 by separating the contributions to the two Through and the Drop port as the sum of three different terms corresponding to the three following device states.

State (I): Input signal In_1 only is injected and propagated from the top to the bottom of the device.

$$\begin{pmatrix} A_{In_1} = |A_{In_1}| e^{i\phi_1} \\ A_{Ad} = 0 \\ A_{In_2} = 0 \end{pmatrix} \longmapsto \begin{pmatrix} A_{Th_1^{(I)}} \\ A_{D\,(I)} \\ A_{Th_2^{(I)}} \end{pmatrix}. \tag{11.4}$$

Schematically this goes as follows (from the right to the left):

$$\longleftarrow \begin{pmatrix} A_3^2 \\ A_3^1 \end{pmatrix} = \mathbf{T^{PK}} \begin{pmatrix} A_{In_1} \\ A_{Th_1^{(I)}} \end{pmatrix} \tag{11.5}$$

$$\longleftarrow \begin{pmatrix} A_5^2 \\ A_{D\,(I)} \\ A_5^1 \end{pmatrix} = \mathbf{T^b} \begin{pmatrix} A_3^2 \\ 0 \\ A_3^1 \end{pmatrix} \longleftarrow \tag{11.6}$$

$$\begin{pmatrix} 0 \\ A_{Th_2^{(I)}} \end{pmatrix} = \mathbf{T^{KP}} \begin{pmatrix} A_5^2 \\ A_5^1 \end{pmatrix} \longleftarrow \tag{11.7}$$

This means that the first set of equations from the first transferral of eq. 11.5

$$A_3^2 = T_{11}^{PK} A_{In_1} + T_{12}^{PK} A_{Th_1^{(I)}} \tag{11.8}$$
$$A_3^1 = T_{21}^{PK} A_{In_1} + T_{22}^{PK} A_{Th_1^{(I)}},$$

have to be inserted into eq. 11.6 to obtain:

$$A_5^2 = (T_{11}^b T_{11}^{PK} + T_{13}^b T_{21}^{PK}) A_{In_1} + \tag{11.9}$$

$$+(T_{11}^b T_{12}^{PK} + T_{13}^b T_{22}^{PK}) A_{Th_1^{(I)}},$$

$$A_{D\,(I)} = (T_{21}^b T_{11}^{PK} + T_{23}^b T_{21}^{PK})\, A_{In_1} +$$

$$+ (T_{21}^b T_{12}^{PK} + T_{23}^b T_{22}^{PK})\, A_{Th_1^{(I)}}\,, \qquad (11.10)$$

$$A_5^1 = (T_{31}^b T_{11}^{PK} + T_{33}^b T_{21}^{PK})\, A_{In_1} +$$

$$+ (T_{31}^b T_{12}^{PK} + T_{33}^b T_{22}^{PK})\, A_{Th_1^{(I)}}\,. \qquad (11.11)$$

Proceeding further with the next transfer we have from eq. 11.7 that:

$$0 = T_{11}^{KP}\, A_5^2 + T_{12}^{KP}\, A_5^1\,, \qquad (11.12)$$

$$A_{Th_2^{(I)}} = T_{21}^{KP}\, A_5^2 + T_{22}^{KP}\, A_5^1\,, \qquad (11.13)$$

which, through eqs. 11.9, 11.10 and 11.11, leads to:

$$A_{Th_1^{(I)}} = T_{11}\, A_{In_1}\,, \qquad (11.14)$$

$$A_{D\,(I)} = T_{21}\, A_{In_1}\,, \qquad (11.15)$$

$$A_{Th_2^{(I)}} = T_{31}\, A_{In_1}\,, \qquad (11.16)$$

with

$$T_{11} = -\frac{T_{11}^{KP} A + T_{12}^{KP} B}{T_{11}^{KP} C + T_{12}^{KP} D}\,, \qquad (11.17)$$

$$T_{21} = E + F\, T_{11}\,, \qquad (11.18)$$

$$T_{31} = G + H\, T_{11}\,, \qquad (11.19)$$

and

$$A = T_{11}^b T_{11}^{PK} + T_{13}^b T_{21}^{PK}\,, \qquad (11.20)$$

$$B = T_{31}^b T_{11}^{PK} + T_{33}^b T_{21}^{PK}\,, \qquad (11.21)$$

$$C = T_{11}^b T_{12}^{PK} + T_{13}^b T_{22}^{PK}\,, \qquad (11.22)$$

$$D = T_{31}^b T_{12}^{PK} + T_{33}^b T_{22}^{PK} \,, \tag{11.23}$$

$$E = T_{21}^b T_{11}^{PK} + T_{23}^b T_{21}^{PK} \,, \tag{11.24}$$

$$F = T_{21}^b T_{12}^{PK} + T_{23}^b T_{22}^{PK} \,, \tag{11.25}$$

$$G = T_{21}^{KP} A + T_{22}^{KP} B \,, \tag{11.26}$$

$$H = T_{21}^{KP} C + T_{22}^{KP} D \,. \tag{11.27}$$

State (II): Input signal In_2 only is injected and propagated from the bottom to the top of the device.

$$\begin{pmatrix} A_{In_1} = 0 \\ A_{Ad} = 0 \\ A_{In_2} = |A_{In_2}| e^{i\phi_2} \end{pmatrix} \longmapsto \begin{pmatrix} A_{Th_1^{(III)}} \\ A_{D\,(III)} \\ A_{Th_2^{(III)}} \end{pmatrix} . \tag{11.28}$$

One proceeds exactly as for state (I), but in the opposite direction. The only difference in the final result is that in eqs. 11.14, 11.15, 11.16 the ports $(In_1, Through_1^{(I)}, Through_2^{(I)})$ have to be exchanged with $(In_2, Through_2^{(III)}, Through_1^{(III)})$:

$$A_{Th_1^{(III)}} = T_{13}\, A_{In_2} \,. \tag{11.29}$$

$$A_{Drop^{(III)}} = T_{23}\, A_{In_2} \,, \tag{11.30}$$

$$A_{Th_2^{(III)}} = T_{33}\, A_{In_2} \,, \tag{11.31}$$

with $T_{13} = T_{31}$, $T_{23} = T_{21}$ and $T_{33} = T_{11}$.

State (III): Add port signal only is injected and propagated from the central Add waveguide towards the Drop and upper and lower Through ports.

In the transfer matrix of eq. 7.10 only one coefficient is missing, namely T_{22}. This is fixed by the other matrix elements and power conservation criteria. Expressing

explicitly with the matrix elements of **T** the power balance between the input and output intensities of the waves it must hold:

$$|A_{In_1}|^2 + |A_{In_2}|^2 + |A_{Ad}|^2 = \tag{11.32}$$

$$|A_{Th_1}|^2 + |A_D|^2 + |A_{Th_2}|^2 + Loss = \tag{11.33}$$

$$= \left(|T_{11}|^2 + |T_{21}|^2 + |T_{31}|^2\right)\left(|A_{In_1}|^2 + |A_{In_2}|^2\right) + \tag{11.34}$$

$$+ \left(2|T_{21}|^2 + |T_{22}|^2\right)|A_{Ad}|^2 + , \tag{11.35}$$

$$+ \left(T_{11}T_{31}^* + |T_{21}|^2 + T_{31}T_{11}^*\right)\left(A_{In_1}A_{In_2}^* + A_{In_1}^*A_{In_2}\right) + , \tag{11.36}$$

$$+ \left(T_{11}T_{21}^* + T_{21}T_{22}^* + T_{31}T_{21}^*\right)\left(A_{In_1} + A_{In_1}\right)A_{Ad}^* + , \tag{11.37}$$

$$+ \left(T_{11}^*T_{21} + T_{21}^*T_{22} + T_{31}^*T_{21}\right)\left(A_{In_1}^* + A_{In_2}\right)A_{Ad} + Loss . \tag{11.38}$$

with the last term indicating the losses of the structure. This implies the conditions:

$$|T_{11}|^2 + |T_{21}|^2 + |T_{31}|^2 = 1; \tag{11.39}$$

$$2|T_{21}|^2 + |T_{22}|^2 = 1; \tag{11.40}$$

$$T_{11}T_{31}^* + |T_{21}|^2 + T_{31}T_{11}^* = 0; \tag{11.41}$$

$$T_{11}^*T_{21} + T_{21}^*T_{22} + T_{31}^*T_{21} = 0 . \tag{11.42}$$

Conditions 11.39 and 11.41 are already satisfied by the coefficients found in the two previous cases (very cumbersome and long calculations, we don't prove this analytically, but numeric implementation has verified this). From 11.42 we finally obtain the last coefficient for matrix 7.10:

$$T_{22} = -\frac{T_{21}}{T_{21}^*}\left(T_{11}^* + T_{31}^*\right), \tag{11.43}$$

which automatically satisfies also 11.40 through 11.41.

12   Acronyms

CMOS = Complementary Metal-Oxide-Semiconductor

CMT = Coupled Mode Theory

CRIT = Coupled Resonator Induced Transparency

CROW = Coupled Resonator Optical Waveguides

CWDM = Coarse Wavelength Division Multiplexing

ds- = double sided

dc- = double channel

DWDM = Coarse Wavelength Division Multiplexing

EM = Electromagnetic

FDTD = Finite Difference Time Domain

FSR = Free Spectral Range

FVFD= Full Vectorial Finite Difference

FWHM = Full Width at Half Maximum

GDS = Graphic Database System

GVD = Group Velocity Dispersion

IC = Integrated Circuit

INL = Institut des Nanotechnologies de Lyon

MMI = Multi Mode Interference

MZ = Mach-Zhender

MZI = Mach-Zhender Interferometer

ONoC = Optical networks on chip

PIC = Photonic Integrated Circuit

PM = Polarization Maintaining

PSE = Photonic Switching Element

SEM = Scanning Electron Microscope

SCISSOR = Side-Coupled Integrated Spaced-Sequences of Resonators

SOI = Silicon-on-Insulator

TBC = Transparent Boundaries Conditions

UPML = Uniaxial Perfectly Matched Layers

VOA = Variable Optical Attenuator

WDM = Wavelength Division Multiplexing

WGW = Waveguide Width

WADIMOS = Wavelength Division Multiplexed Photonic Layer on CMOS

13   Nomenclature and conventions

Normalized intensity: if not mentioned otherwise the powers of the input signals are set to unity ($I_{In_j} = 1$, (j=1,..,N)) and the output signal powers I_{Out_j} on the abscissa of the graphs are rescaled to the sum of the input intensities, i.e. $\frac{I_{Out_j}}{\sum I_{In_j}}$.

Radius R: the physical curvature radius of a bend is taken to be that from the center to the *middle* of the waveguide.

Amplitude and intensity port labels: In, Through, Drop and Add signal amplitudes and intensities are labeled as A_{In}, A_{Th}, A_D, A_{Ad} and I_{In}, I_{Th}, I_D, I_{Ad} respectively.

Loss parameters: on bends radiative losses are expressed as loss per arc length, i.e. in dB/90°. Material losses are given in loss per unit length, i.e. dB/cm.

14 On the author

Marco Masi was born the 4th of April 1965 in Milan, Italy. He received his Masters degree in astrophysics at the university of Padua, Italy. After authoring several articles in astronomy, statistical mechanics and mathematical physics he is now completing his Ph.D. studies at the Nanoscience Laboratory of the university of Trento (Italy). His present interests focus on silicon photonics, in particular on the design, modeling and fabrication of photonic integrated circuits of micro-resonant structures, its applications to WDM and interconnect technologies, and possible other areas of physics.

Articles published and submitted as result of doctoral activity:

First name

"*Towards a realistic modelling of ultra-compact racetrack resonators*", M. Masi, R. Orobtchouk, G. Fan, J-M. Fedeli, and L.Pavesi, Journal of LightWave Technology, 22, 3233, (2010).

"*A silicon photonic phase router device based on SCISSOR concept*", M. Masi, M. Mancinelli, A. Battarelli, R. Guider, M. R. Vanacharla, P. Bettotti, J-M. Fedeli, and L. Pavesi, submitted (2010).

"*Light combining for phase switching*", M. Masi, and L. Pavesi, in preparation (2010).

Co-authored

"*Coupled-resonator-induced-transparency concept for wavelength router applications*", M. Mancinelli, R. Guider, P. Bettotti, M. Masi, M. R. Vanacharla, and L. Pavesi, submitted (2010).

"*Robust design of an optical router based on asymmetric side coupled integrated spaced sequence of optical resonators*", P. Bettotti, M. Mancinelli, R. Guider, M. Masi, and L. Pavesi, submitted (2010).

"*Optical characterization of a SCISSOR device*", M. Mancinelli, R. Guider, M. Masi, P.

Bettotti, M. R. Vanacharla, J-M. Fedeli, and L. Pavesi, submitted (2010).

"*Optical characterization of SOI based single and coupled racetrack resonators*", M. Mancinelli, R. Guider, P. Bettotti, M. Masi, M. R. Vanacharla, J-M. Fedeli, D. Van Thourhout, and L. Pavesi, submitted (2010).

Pre-doctoral published articles:

Single authored

"*On the extended Kolmogorov-Nagumo information-entropy theory, the q-¿1/q duality and its possible implications for a non-extensive two dimensional Ising model*", Physica A, 377, 1, 67-78 (2007).

"*On compressive radial tidal forces*", American Journal of Physics, 75 (2), February 2007.

"*On the q-parameter spectrum of generalized information-entropy measures with no cut-off prescriptions*", Physics Letters A 357, 288-294 (2006).

"*A step beyond Tsallis and Renyi entropies*", Physics Letters A, 338, 217-224 (2005).

First name

"*Effects of the Planar Galactic Tides and Stellar Mass on Comet Cloud Dynamics*" M. Masi, L. Secco and G. Gonzalez, in The Open Astronomy Journal, Vol. 2, 74-89, 2009.

"*Dynamical effects of the Galaxy on the Oort's Cloud*", M. Masi, L. Secco and V. Vanzani, in Memorie della Societ Astronomica Italiana, Vol. 73, 23 (2002).

"*Cenni storici sul decentramento del sito della Vita*" - ("Historical outline of the decentralization of location of Life"), together with L. Secco and V. Vanzani, in Giornale di Fisica, Vol. XLIII, N.4 - 2002.

Pre-print

"*Generalized information-entropy measures and Fisher information*", arXiv: cond-mat/0611300.

15 References

References

[1] K. Asanovic', R. Bodik, J. Demmel, T. Keaveny, K. Keutzer, J. Kubiatowicz, N. Morgan, D. Patterson, K. Sen, J. Wawrzynek, D. Wessel, and K. Yelick, "A View of the Parallel Computing Landscape," in *Communications of the ACM*, 2009.

[2] D. A. B. Miller, "Device requirements for Optical Interconnects to Silicon Chips", Vol. 97, No. 7, Proc. IEEE, Jul. 2009.

[3] A. Shacham, K. Bergman, and L. P. Carloni, "Photonic Networks-on-Chip for Future Generations of Chip Multiprocessors", IEEE Trans. on Computers, Vol. 57, No. 9, Sept. 2008.

[4] L. Pavesi and D. Lockwood, "Silicon Photonics", Topics in Applied Physics, vol. 94, Springer-Verlag, 2004; D. Lockwood and L. Pavesi, "Silicon Photonics II: components and integration" Topics in Applied Physics, Vol. 119, Springer-Verlag 2011

[5] S.J.B. Yoo, "Future prospects of silicon photonics in next generation communication and computing systems", Electronics Lett., Vol. 45 No. 12, June 2009.

[6] A. Joshi, C. Batten, Y-J. Kwon, S. Beamer, I. Shamim, K. Asanovic, V. Stojanovic, "Silicon-Photonic Clos Networks for Global On-Chip Communication", 3rd ACM/IEEE International Symposium on Networks-on-Chip (NoCS), 2009.

[7] L. Liu, T. Spuesens, D. Van Thourhout, G. Morthier, L. Grenouillet, N. Olivier, J-M. Fedeli, P. Rojo-Romeo, P. Rgreny, F. Mandorlo, R. Oroubtchouck, "200mm Wafer Scale III-V/SOI Technology for All-Optical Network-on-Chip and Signal

Processing", conference paper, 7th International Conference on Group IV Photonics Beijing, Sept. 2010.

[8] W. Bogaerts, S. K. Selvaraja, P. Dumon, J. Brouckaert, K. De Vos, D. Van Thourhout, and R. Baets, "Silicon-on-Insulator Spectral Filters Fabricated With CMOS Technology", Jour. Sel. Top. Quantum Electron., vol. 16, pp. 33-44, 2010.

[9] L. Liu, G. Roelkens, J. Van Campenhout, J. Brouckaert, D. Van Thourhout, and R. Baets, "III-V/silicon-on-insulator nanophotonic cavities for optical networks-on-chip, Jour. Nanosci. Nanotechnol., vol. 10, pp. 1461-1472, 2010.

[10] N. Daldosso, L. Pavesi, "Nanosilicon photonics," in *Laser & Photon. Rev.*, **3**, 6, pp. 508-534, 2009.

[11] "Technology focus on Lithography," in *Nature Photonics*, January issue, **4**, 1, 2010.

[12] R. Soref, "The Past, Present, and Future of Silicon Photonics," in *IEEE Journal of Selected Topics in Quantum Electronics*, Vol. 12, **6**, part 2, pp. 1678–1687, 2006.

[13] D. Miller, "Device Requirements for Optical Interconnects to Silicon Chips," in *Proceedings of the IEEE*, **97**, 7, pp. 1166–1185, 2009.

[14] M. Petracca, B. G. Lee, K. Bergman, L. P. Carloni, "Photonic NoCs: System-Level Design Exploration," in *IEEE Micro*, **29**, 4, pp. 74–85, 2009.

[15] L. Chen, K. Preston, S. Manipatruni, and M. Lipson, "Integrated GHz silicon photonic interconnect with micrometer-scale modulators and detectors," in *Opt. Exp.* **17**, 15248–15256, 2009.

[16] J. V. Campenhout, L. Liu, P. R. Romeo, D. V. Thourhout, C. Seassal, P. Regreny, L. Di Cioccio, J. M. Fedeli, and R. Baets, "A Compact SOI-Integrated

Multiwavelength Laser Source Based on Cascaded InP Microdisks," in *IEEE Photnic Technology Lett.*, **20**, 16, 2008.

[17] J. E. Heebner, V. Wong, A. Schweinsberg, R. W. Boyd, and D. J. Jackson, "Optical Transmission Characteristics of Fiber Ring Resonators", Jour. Quant. Eelec., Vol. 40, No. 6, June 2004.

[18] B. G. Lee, A. Biberman, N. Sherwood-Droz, C. B. Poitras, M. Lipson and K. Bergman, "High-Speed 2x2 Switch for Multiwavelength Silicon-Photonic NetworksOn-Chip", Jour. Light. Tech., Vol. 27, No. 14, Jul. 15, 2009.

[19] T. Barwicz, H. Byun, F. Gan, C. W. Holzwarth, M. A. Popovic, P. T. Rakich, M. R. Watts, E. P. Ippen, F. X. Krtner, and H. I. Smith, "Silicon photonics for compact, energy-efficient interconnects", Jour. Opt. Netw., Vol. 6, No. 1, Jan. 2007.

[20] F.Y. Gardes, A. Brimont, P. Sanchis, G. Rasigade, D. Marris-Morini, L. O'Faolain, F. Dong, J.M. Fedeli, P. Dumon, L. Vivien, T.F. Krauss, G.T. Reed, J. Mart, "High-speed modulation of a compact silicon ring resonator based on a reverse-biased pn diode", Opt. Express, Vol. 17, No. 24, Nov. 2009.

[21] A. Yariv, Y. Xu, R. K. Lee, and A. Scherer, "Coupled-resonator optical waveguide: A proposal and analysis, Opt. Lett., Vol. 24, pp. 711713, (1999).

[22] J. E. Heebner, Q. Park, "SCISSOR solitons and other propagation effects in microresonator modified waveguides," J. Opt. Soc. Amer. B, vol. 19, pp. 722731, (2002).

[23] J. E. Heebner, P. Chak, S. Pereira, J. E. Sipe, and R. W. Boyd, "Distributed and localized feedback in microresonator sequences for linear and nonlinear optics," J. Opt. Soc. Am. B 21, 1818-1832 (2004).

[24] F. Xia, L. Sekaric, M. O'Boyle, and Y. Vlasov, "Coupled resonator optical waveguides based on silicon-on-insulator photonic wires", Appl. Phys. Lett. 89, 041122 (2006)

[25] J. Capmany, P. Munoz, J. D. Doemenech, M. A. Muriel, "Apodized coupled resonator waveguides", Optics Express, vol.15, no. 16 (2007).

[26] S. Y. Cho, R. Soref, "Apodized SCISSORs for filtering and switching," Opt. Express 16, 19078-19090 (2008).

[27] Y. Vlasov, W. M. J. Green and F. Xia, "High-throughput silicon nanophotonic wavelength-insensitive switch for on-chip optical networks", Nature Phot., Vol. 2, Apr. 2008.

[28] M. A. Popovic', T. Barwicz, M. S. Dahlem, F. Gan, C. W. Holzwarth, P. T. Rakich, H. I. Smith, E. P. Ippen and F. X. Krtner, "Tunable, Fourth-Order Silicon Microring-Resonator Add-Drop Filters", Opt. Express, Vol. 17, Issue 16, pp. 14063-14068, 2009.

[29] M. Mancinelli, R. Guider, M. Masi, P. Bettotti, M. R. Vanacharla, Jean-Marc Fedeli, and L. Pavesi, "Optical characterization of a SCISSOR device", submitted.

[30] M. L. Cooper, G. Gupta, J. S. Park, M. A. Schneider, I. B. Divliansky, and S. Mookherjea, "Quantitative infrared imaging of silicon-oninsulator microring resonators", Opt. Lett. Vol. 35, No. 5, March 2010.

[31] M. Baldi, G. Marchetto, Y. Ofek, "A scalable solution for engineering streaming traffic in the future Internet", Computer Networks Vol. 51, **14**, 10 Oct. 2007.

[32] "Optical Microcavities", ed. K. Vahala, World Scientific Publishing (2004).

[33] O. Schwelb, "Transmission, Group Delay, and Dispersion in Single-Ring Optical Resonators and Add/Drop Filters - A Tutorial Overview," J. Lightwave Technol. 22, 1380 (2004).

[34] F. Xia, L. Sekaric, and Y. Vlasov, "Mode conversion losses in silicon-on-insulator photonic wire based racetrack resonators", Opt. Exp. 3872, vol. 14, No. 9 (2006)

[35] Q. Xu, B. Schmidt, S. Pradhan, and M. Lipson, "Micrometre-scale silicon electro-optic modulator", Nature, **435**, 325-327 (2005).

[36] Q. Xu, S. Manipatruni, B. Schmidt, J. Shakya, and M. Lipson, "12.5 Gbit/s carrier-injection based silicon micro-ring silicon modulators", Opt. Express, **15** 430-436 (2007).

[37] Q. Xu, D. Fattal, and R.G. Beausolei, "Silicon microring resonators with $1.5 - \mu m$ radius", Opt. Express **16**, 6, (2008).

[38] Q. Xu, B. Schmidt, J. Shakya, and M. Lipson, "Cascaded silicon micro-ring modulators for WDM optical interconnection", Opt. Express **14**, 20, (2006).

[39] J.E. Heebner and R.W. Boyd, "Slow light, induced dispersion, enhanced nonlinearity, and optical solitons in a resonator-array waveguide", Phys. Rev. E, **65**, 036619, (2002).

[40] J. K. S. Poon, J. Scheuer, S. Mookherjea, G. Paloczi, Y. Huang, and A. Yariv, "Matrix analysis of microring coupled-resonator optical waveguides," Opt. Express 12, 90-103 (2004).

[41] O. Weiss and J. Scheuer, "Side coupled adjacent resonators CROW - formation of mid-band zero group velocity," Opt. Express **17**, 14817 (2009).

[42] F. Xia, L. Sekaric, and Y. Vlasov, "Ultracompact optical buffers on a silicon chip", Nature Photonics, **1**, 65-71 (2007).

[43] A. Canciamilla, C. Ferrari, A. Melloni, M. Torregiani, F. Morichetti, A. Samarelli, M. Sorel, and R. De La Rue, "Reconfigurable CROW delay lines on a silicon platform", Platform, CLEO 2009, Munich, Germany, 14-19 June, 2009.

[44] T. S. El-Bawab, "Optical Switching", Springer (2006).

[45] S. Cho and R. Soref, "Interferometric microring-resonant 2 x 2 optical switches," Opt. Express 16, 13304-13314 (2008)

[46] P. Dong, S. Liao, H. Liang, R. Shafiiha, D. Feng, G. Li, X. Zheng, A.V. Krishnamoorthy, and M. Asghari, "Submilliwatt, ultrafast and broadband electro-optic silicon switches," Opt. Express 18, 25225-25231 (2010).

[47] D. D. Smith, H. Chang, K.A. Fuller, A. T. Rosenberger and R. W. Boyd, "Coupled-resonator-induced transparency", Phys. Rev., A 69, 063804 (2004).

[48] Q. Xu, S. Sandhu, M. L. Povinelli, J. Shakya, S. Fan, and M. Lipson, "Experimental Realization of an On-Chip All-Optical Analogue to Electromagnetically Induced Transparency", Phys. Rev. Lett. PRL 96, 123901 (2006).

[49] Y.F. Xiao, X.B. Zou, W. Jiang, Y.L. Chen, and G.C. Guo, "Analog to multiple electromagnetically induced transparency in all-optical drop filter systems", Phys. Rev. A, 75, 063833 (2007).

[50] X. Yang, M. Yu, D. L. Kwong, and C. W. Wong, "All-optical analog to electromagnetically induced transparency in multiple coupled photonic crystals cavities", Phys. Rev. Lett. 102, 173902-4 (2009).

[51] M. Masi, M. Mancinelli, M.R. Vanacharla, A. Battarelli, R. Guider, P. Bettotti, J-M. Fedeli and L. Pavesi, "A silicon photonic phase router device based on SCISSOR concept", submitted.

[52] G. T. Reed, G. Mashanovich, F. Y. Gardes, D. J. Thomson1, "Silicon optical modulators", Nature Photonics vol. 4, (2010).

[53] A.W. Poon, X. Luo, F. Xu, and H. Chen, "Cascaded Microresonator-Based Matrix Switch for Silicon On-Chip Optical Interconnection", Proc. IEEE, **97**, 7, 1216 - 1238 ,(2009).

[54] A. Kazmercziak, E. Drouard, M. Briere, P. Rojo Romeo, X. Letartre, I. O Connor, F. Gaffiot, Z. Lisik, "Optimization of an integrated optical crossbar in SOI technology for optical networks on chip", Jour. of Telecom. Inf. Tech. **3** 109-114 (2007).

[55] N. Sherwood-Droz, H. Wang, L. Chen, B. G. Lee, A. Biberman, K. Bergman, and M. Lipson, "Optical 4x4 hitless slicon router for optical networks-on-chip (NoC)," Opt. Express **16**, 15915-15922 (2008).

[56] B.G. Lee, A. Biberman, J. Chan, and K. Bergman, "High-Performance Modulators and Switches for Silicon Photonic Networks-on-Chip", IEEE Jour. Sel. Topics in Quant. Electr. **16**, 1, (2010)

[57] A. W. Topol, D. C. L. Tulipe, Jr., L. Shi, D. J. Frank, K. Bernstein, S. E. Steen, A. Kumar, G. U. Singco, A. M. Young, K. W. Guarini, and M. Ieong, Three-dimensional integrated circuits, IBM J. Res. Dev., **50**, 4/5, pp. 491506, (2006).

[58] V. F. Pavlidis, I. Savidis, and E. G. Friedman, Clock distribution networks for 3-D integrated circuits, in Proc. IEEE Custom Integr. Circuits Conf. (CICC), San Jose, CA, pp. 651654, (2008).

[59] Y.M. Darmawan, S. Chin, M. K. Landobasa, "Matrix analysis of 2-D microresonator lattice optical filters", Quantum Electronics, IEEE Journal of Vol. 41, Issue 11 (2005).

[60] C. S. Ma, ; X. Yan, X.Y Wang, "Matrix analysis of 2D microring resonator arrays", Jour. of Mod. Opt., vol. 55, issue 1, pp. 143-154, (2008).

[61] J. K. S. Poon, P. Chak, J. M. Choi, and A. Yariv, "Slowing light with Fabry-Perot resonator arrays," J. Opt. Soc. Am. B 24, 2763-2769 (2007).

[62] D. Marcuse, "Theory of Dielectric Optical Waveguides", Academic Press, 1974.

[63] K. Okamoto, "Fundamentals of Optical Waveguides", Second Edition, Academic Press, 2006.

[64] H. Kogelnik, "Guided-Wave Optoelectronics: Device Characterization, Analysis, and Design", T. Tamir (ed.), Springer, Berlin, 2nd edition (1990).

[65] G. Lifante, "Integrated Photonics: Fundamentals", Wiley (2003).

[66] K. Lizuka, "Elements of Photonics" Wiley-Interscience ed. 2002.

[67] A. Milos, C. Manolatou and M.R. Watts, "Coupling-induced resonance frequency shifts in coupled dielectric multi-cavity filters", Opt. Exp. 1208, vol. 14, No. 3, 2006.

[68] E.D. Palik, "Handbook of Optical Constants of Solids", Academic Press, San Diego, CA, 1985.

[69] Mode solver based on a full vectorial finite difference scheme and developed for internal use by Regis Orobtchouk at the Institut des Nanotechnologies de Lyon, Université de Lyon.

[70] From a private comunication of one of the authors (R. Orobtchouk).

[71] K. R. Hiremath, "Coupled Mode Theory Based Modeling and Analysis of Circular Optical Microresonators", Ph.D. thesis.

[72] P. Bienstman, S. Selleri, L. Rosa, H. P. Uranus, W.C.L. Hopman, R. Costa, A. Melloni, L.C. Andreani, J. P. Hugonin, P. Lalanne, D. Pinto, S.S.A. Obayya, M. Dems, and K. Panajotov, "Modelling leaky photonic wires: A mode solver comparison", Opt. and Quantum Electr. 38:731759, (2006).

[73] A. Vorckel, A. Monster, M. Henschel, P. H. Bolivar, H. Kurz, "Asymmetrically coupled silicon-on-insulator microring resonators for compact add-drop multiplexers", IEEE Phot. Tech. Lett., vol. 15, no.7 (2003).

[74] M. Masi, R. Orobtchouk, G. F. Fan and L. Pavesi, "Towards realistic modeling of ultra-compact racetrack resonators", Jour. Lightw. Tech. **28** (22), 3233 (2010).

[75] IMEC and CEA-LETI are CMOS development labs partnering in ePIXfab, the a Silicon Photonics Platform within the framework of ePIXnet, the FP6 European Network of Excellence on photonic integrated components and circuits.

[76] From a private communication with Régis Orobtchouk, Institut des Nanotechnologies de Lyon, Université de Lyon, INL-UMR5270, CNRS, INSA de Lyon, 69621 Villeurbanne, France.

[77] W. Bogaerts, P. Dumon, D. Van Thourhout, R. Baets, "Low-loss, low-cross-talk crossings for silicon-on-insulator nanophotonic waveguides," Opt. Lett. 32, 2801-2803, 2007.

[78] KLayout is a GDS layout, viewer and editor for chip design engineering of CMOS and photonic circuits. www.klayout.de

[79] C. Madsen and J. Zhao, "Optical filter and analysis: a signal processing approach", vol. 16 (1999).

[80] F. Wang, X. Wang, H. Zhou, Q. Zhou, Y. Hao, X. Jiang, M. Wang, and J. Yang, "Fano-resonance-based Mach-Zehnder optical switch employing dual-bus coupled ring resonator as two-beam interferometer," Opt. Express 17, 7708-7716 (2009).

[81] U. Fano, Sullo spettro di assorbimento dei gas nobili presso il limite dello spettro d'arco, Nuovo Cimento 12, 154161, (1935).

[82] U. Fano, Effects of Configuration Interaction on Intensities and Phase Shifts, Phys. Rev. 124, 18661878, (1961).

[83] A. E. Miroshnichenko, S. Flach, and Y. S. Kivshar, "Fano resonances in nanoscale structures", Rev. Mod. Phys., in print; arXiv:0902.3014 (2009).

[84] S. Fan, W. Suh, and J. D. Joannopoulos, "Temporal coupled-mode theory for the Fano resonance in optical resonators," J. Opt. Soc. Am. A 20, 569-572 (2003).

[85] L. Y. Mario, S. Darmawan, and Mee K. Chin, "Asymmetric Fano resonance and bistability for high extinction ratio, large modulation depth, and low power switching", Opt. Express 14, 12770-12781 (2006).

[86] L. J. Zhou and A. W. Poon, "Fano resonance-based electrically reconfigurable add-drop filters in silicon microring resonator-coupled Mach-Zehnder interferometers," Opt. Lett. 32, 781-783 (2007).

[87] Y. Lu, J. Q. Yao, X. F. Li, and P. Wang, "Tunable asymmetrical Fano resonance and bistability in a microcavity-resonator-coupled Mach-Zehnder interferometer," Opt. Lett. 30, 3069-3071 (2005).

[88] M. Mancinelli, R. Guider, P. Bettotti, M. Masi, M.R. Vanacharla and L. Pavesi "Coupled-resonator-induced-transparency concepte for wavelength router applications. In preparation.

[89] P. Bettotti, M. Mancinelli, R. Guider, M. Masi, M.R. Vanacharla and L. Pavesi "Optical router for dense wavelength multiplexing based on asymmetric side coupled integrated sequence of optical resonators". In preparation.